PERSISTENT SCATTERER INTERFEROMETRY IN NATURAL TERRAIN

A DISSERTATION

SUBMITTED TO THE DEPARTMENT OF ELECTRICAL ENGINEERING

AND THE COMMITTEE ON GRADUATE STUDIES

OF STANFORD UNIVERSITY

IN PARTIAL FULFILLMENT OF THE REQUIREMENTS

FOR THE DEGREE OF

DOCTOR OF PHILOSOPHY

Piyush Shanker Agram

August 2010

This dissertation is online at: http://purl.stanford.edu/fm943vt7275

I certify that I have read this dissertation and that, in my opinion, it is fully adequate in scope and quality as a dissertation for the degree of Doctor of Philosophy.

Howard Zebker, Primary Adviser

I certify that I have read this dissertation and that, in my opinion, it is fully adequate in scope and quality as a dissertation for the degree of Doctor of Philosophy.

George Hilley

I certify that I have read this dissertation and that, in my opinion, it is fully adequate in scope and quality as a dissertation for the degree of Doctor of Philosophy.

Paul Segall

Approved for the Stanford University Committee on Graduate Studies.

Patricia J. Gumport, Vice Provost Graduate Education

This signature page was generated electronically upon submission of this dissertation in electronic format. An original signed hard copy of the signature page is on file in University Archives.

Abstract

Time-series InSAR techniques are designed to estimate the temporal characteristics of surface deformation by combining information from multiple SAR images acquired over time. In many cases, these techniques also enable us to measure deformation signals in locations where conventional InSAR fails and also to reduce the error associated with deformation measurements. Among these techniques, Persistent Scatterer (PS) methods work by identifying the ground resolution elements that are dominated by a single scatterer. A persistent scatterer exhibits reduced baseline and temporal decorrelation due to its stable, point-like scattering mechanism. In PS analysis, a set of interferograms formed with a single master scene are processed at single look resolution in order to maximize the signal-to-clutter ratio (SCR) of the resolution elements containing a single dominant scatterer. In urban terrain, buildings and other man-made structures often act as PS due to their corner reflector-like scattering behavior and high radar reflectivity. Hence, traditional SAR amplitude-based PS-InSAR techniques have proved to be very effective in urban terrain. In natural terrain, the absence of bright manmade structures makes reliable estimation of deformation using PS-InSAR techniques a challenging task. The main obstacle is in the phase unwrapping stage, where the solutions are directly dependent on the PS network density.

We have developed a two pronged approach to improve the applicability of PS-InSAR techniques to natural terrain - increasing PS network density and improving the reliability of phase unwrapping algorithms. We first present an information theoretic approach to PS pixel selection and demonstrate the ability of these new

algorithms in identifying a denser network of PS in natural terrain. We then address the spatio-temporal (three dimensional) phase unwrapping problem applicable to sparse and non-uniformly sampled time-series InSAR data sets, and present two novel phase unwrapping algorithms. We demonstrate the efficacy of our new PS selection technique with experimental results from the San Francisco Bay Area, Lyngen region of Norway and the creeping section of the Central San Andreas Fault. We explain the salient features of our new "edgelist" phase unwrapping algorithm with results from the Central San Andreas Fault region north of Parkfield, CA. We provide detailed comparisons of the estimated line of sight velocity and deformation time-series with results from other time-series InSAR algorithms developed by research groups based in NORUT, Norway and IREA-CNR, Italy.

Acknowledgments

Piyush Shanker Agram

Stanford, California
August 12, 2010

I owe my deepest gratitude to my advisor, Prof. Howard Zebker, for his untiring guidance, advice and mentorship, and for being a great teacher and a source of inspiration. I'm also grateful to Prof. Paul Segall for his encouragement, guidance and insightful research advice. I'm indebted to George Hilley for kindly agreeing to be the third thesis reader and providing valuable comments that helped improve this thesis.

I am indebted to Andrew Hooper for being available to answer all my questions patiently during the early stage of my Ph.D and for constructive suggestions later on. I also owe the completion of this thesis to ideas and projects executed in collaboration with Tom Rune Lauknes, Francesco Casu, Isabelle Ryder and Mariana Eneva. Other colleagues who have been instrumental in my education are Leif Harcke, Noa Bechor, Fayaz Onn, Ana Bertrán Ortiz, Shadi Oveisgharan, Lauren Wye, Cody Wortham, Albert Chen, Jessica Reeves and Jingyi Chen.

My work was supported generously by the NASA Earth and Space Science Fellowship (NESSF) and other grants from the USGS, NSF and NASA. I would also like to thank Prof. Leonard Tyler and Prof. Jerry Harris for supporting my education by extending research and teaching assistantships.

I'm forever indebted to my parents, my sister, my uncle Ravi Nanjundiah and family for their constant support, encouragement and guidance. A number of friends have been instrumental in making my stay at Stanford a joyful and

memorable experience, including Sachin Premasuthan, Ankit Bhagatwala, Stephanie Hurder, Mamta Parakh, Tanmay Chaturvedi, Debarun Bhattacharjya, Sameer Parakh, Shankar Swaminathan and Hari Kannan. My interaction with the Bechtel International Center, EV Community Associate Program and the Stanford Cricket Club also provided a refreshingly relaxing break from research and many memorable experiences that I will fondly cherish.

Contents

List of Tables

List of Figures

List of Abbreviations

1-D ..... one dimensional

2-D ..... two dimensional

3-D ..... three dimensional

N-D ..... N dimensional

APS ..... Atmospheric Phase Screen

DEM ..... Digital Elevation Model

DLR ..... German Aerospace Center

ESA ..... European Space Agency

Envisat ..... European Space Agency's environmental satellite

ERS-1 ..... European Space Agency's Earth Remote Sensing satellite 1

ERS-2 ..... European Space Agency's Earth Remote Sensing satellite 2

ER ..... Error Rate

FFT ..... Fast Fourier Transform

GNSS ..... Global Navigation Satellite System

GPS ..... Global Positioning System

GSAR ..... Generic SAR processor from Norut

IFG ..... Interferogram

JPL ..... NASA's Jet Propulsion Laboratory

LOS ..... Line-of-sight

LP ..... Linear Program

MCF ..... Minimum Cost Flow

ML . . . . . Maximum Likelihood

MST . . . . . Minimum Spanning Tree

NASA . . . . . National Aeronautics and Space Administration

NGU . . . . . Geological Survey of Norway

Norut . . . . . Northern Research Institute, Norway

Radar . . . . . RAdio Detection and Ranging

SAR . . . . . Synthetic Aperture Radar

InSAR . . . . . Interferometric Synthetic Aperture Radar

IREA-CNR . . . . . Institute for Electromagnetic Sensing of Environment, Napoli

D-InSAR . . . . . Differential Interferometric Synthetic Aperture Radar

PDF . . . . . Probability Distribution Function

PS . . . . . Persistent Scatterers or Permanent Scatterers

PS-InSAR . . . . . Persistent Scatterer Interferometric Synthetic Aperture Radar

PSI . . . . . Persistent Scatterer Interferometry

RMSE . . . . . Root Mean Squared Error

RPAR . . . . . Random Pixels Acceptance Rate

SB . . . . . Short Baseline

SBAS . . . . . Small Baseline Subset Algorithm

SEASAT . . . . . NASA's remote sensing satellite

SCR . . . . . Signal-to-clutter ratio

SNR . . . . . Signal-to-noise ratio

SLC . . . . . Single look complex SAR image

SRTM . . . . . Shuttle Radar Topography Mission

StaMPS . . . . . Stanford Method for PS

SFSU . . . . . San Francisco State University

TUM . . . . . Total Unimodularity

USGS . . . . . United States Geological Survey

WGS-84 . . . . . World Geodetic System 1984

ZWD . . . . . Zenith Wet Delay

List of Symbols

$\Delta\phi$ ..... Interferometric phase

$\Delta\rho$ ..... Difference in LOS range

λ ..... Wavelength

ϕ_{base} ..... Interferometric phase due to perfectly ellipsoidal Earth

ϕ_{topo} ..... Interferometric phase due to topography

ϕ_{defo} ..... Interferometric phase due to deformation

ϕ_{atm} ..... Interferometric phase due to atmospheric phase screen

ϕ_{noise}, ϕ_n ..... Interferometric phase noise

B ..... Interferometric baseline

$B_\perp$ ..... Component of Interferometric baseline perpendicular to LOS

α ..... Baseline angle with the horizontal

θ ..... Look angle

$\Delta\phi_\epsilon$ ..... Phase error due to sub-pixel position of PS

$\Delta\phi_{orb}$ ..... Phase error due to orbit errors

Δh ..... Error in DEM

ϵ ..... Sub-pixel position in range of dominant scatterer

Δr ..... Range resolution

η ..... Sub-pixel position in azimuth of dominant scatterer

v ..... Relative velocity of the SAR imaging platform

F_{DC} ..... Doppler centroid of a SAR scene

z_i ..... Complex return from pixel i

f_θ ..... PDF of SAR pixel phase

f_ϕ ..... PDF of InSAR pixel phase

f_r ..... PDF of SAR pixel amplitude

μ_n ..... Mean of random variable n

σ_n ..... Standard deviation of random variable n

γ ..... Signal-to-Clutter Ratio

ρ ..... Correlation

ρ_{temp} ..... Temporal coherence

ρ_{thr} ..... Correlation threshold

P_{obs} ..... Probability as computed using observed data

P_{sim} ..... Probability as computed using simulations

γ_{ML} ..... Maximum likelihood estimate of γ

C_{ij} ..... Cost of unit flow on edge (i, j)

K_{ij} ..... Integer flow on edge (i, j)

P_{ij} ..... Integer flow from i to j on edge (i, j)

Q_{ij} ..... Integer flow from j to i on edge (i, j)

$\tilde{S}$ ..... Delaunay triangulation of set of sparse points S

$\hat{S}$ ..... Discrete Voronoi diagram of set of sparse points S

n_i ..... Integer cycle multiplier for pixel i

ψ_i ..... Wrapped phase observation for pixel i

ϕ_i ..... Unwrapped phase observation for pixel i

$\bar{v}$ ..... Mean velocity

$\bar{a}$ ..... Mean acceleration

$\Delta\bar{a}$ ..... Mean acceleration variation

Chapter 1

Introduction

Surface deformation measurements are critical for the study and detailed understanding of of tectonics, earthquakes, volcanism and landslides. Geodetic measurements provide invaluable information on the accumulation or release of strain in seismically active faults or stretching of the crust as a result of magma migration from the mantle through the crust in volcanoes. Geodetic measurements also play an important role in monitoring active landslides and provide important insight into their kinematics. Global positioning system (GPS) networks and interferometric synthetic aperture radar (InSAR) are the two most popular techniques used for measuring surface deformation. InSAR has an unique advantage in its ability to measure deformation with centimeter scale accuracy over large contiguous areas (few hundred kilometers). However, almost any interferogram includes large areas where the signals decorrelate due to the imaging geometry, vegetation or change in surface scattering properties and no reliable measurement is possible. Moreover the deformation measurements due to a single interferogram are affected by the variation in atmospheric properties. Persistent scatterer (PS) InSAR refers to a family of time-series InSAR techniques that addresses both the decorrelation and atmospheric problems of conventional InSAR.

Early PS-InSAR techniques were designed to identify very bright scatterers, whose scattering properties vary little with imaging geometry and time. Such techniques work well in urban areas where man-made structures behave like strongly reflecting corner reflectors but fail to perform satisfactorily in vegetated terrain. The StaMPS

(Stanford Method for Persistent Scatterers) technique, developed by Andy Hooper, was the first PS-InSAR method designed to estimate a deformation signal even in the absence of very bright scatterers using a self-consistent network of PS. In this work, we build upon StaMPS PS selection framework and develop an information theoretic approach to improve PS selection in non-urban and vegetated terrain. We apply our new Maximum Likelihood (ML) PS selection technique to identify a denser network of PS in non-urban regions of the San Francisco Bay Area. We then present a new edge-based phase unwrapping algorithm that is more flexible than the conventional network programming phase unwrapping techniques. We apply this algorithm to unwrap a sparse PS dataset and estimate the time-dependent creep across the Central San Andreas Fault. This constitutes the first such analysis of this heavily decorrelated section of the San Andreas Fault using time-series InSAR techniques. We then compare the results of our new PS selection techniques against those obtained with two different short baseline time-series InSAR implementations. We compare PS-InSAR results and small baseline subset algorithm (SBAS) results from Northern Research Institute, Tromso (Norway) over the rockslides in Lyngen region of Norway. We also compare PS-InSAR and SBAS results from IREA-CNR, Naples (Italy) on a pixel-by-pixel basis in the radar coordinates to characerize the noise properties of time-series InSAR deformation estimates. Significantly, we observe that that these results agree to within 1 mm/yr and 5 mm line of sight (LOS) velocity and absolute displacement respectively.

1.1 Contributions

There are three aspects to this dissertation. First, we describe a new Bayesian PS selection technique based on statistical models that extends the applicability of PS-InSAR techniques in natural terrain. Second, we describe new phase unwrapping algorithms for sparse PS networks that significantly improves the accuracy of deformation estimates. We then apply these improved PS-InSAR techniques to study

numerous geophysical phenomenon. Finally, we compare the performance of our newly developed PS-InSAR techniques against short baseline (SB) techniques from independent research groups in Europe and characterize the noise properties of our time-series results. Below we summarize the main contributions of this work:

1. We design an information theoretic approach to identify persistent scattering pixels in a series of interferograms that outperforms other published algorithms in natural terrain.

2. We develop a new framework that reduces a sparse two-dimensional phase unwrapping problem to a regular two-dimensional phase unwrapping problem.

3. We develop a new generic phase unwrapping formulation capable of handling multidimensional datasets and incorporating external geodetic measurements such as leveling surverys and GPS as constraints.

4. We apply our new methods to estimate the time-series for creep across the central Hayward fault and deformation of areas along the Bay in San Mateo county and Alameda county of California.

5. We apply our new PS selection method and phase unwrapping techniques to studying time-dependent creep across the central section of the San Andreas Fault.

6. We provide a detailed one-to-one comparison of deformation time-series estimated using PS-InSAR and SBAS algorithms for slow moving landslides in Lyngen region, Norway.

7. We conduct a pixel-by-pixel comparison of PS-InSAR and SBAS results in the San Francisco Bay Area and estimate the noise levels in our PS-InSAR estimates to be 1 mm/yr in LOS velocity and 5 mm in absolute LOS displacement compared to the SB estimates.

8. We compare our PS-InSAR deformation time-series with creep measurements from the SFSU-USGS alignment arrays along the Hayward Fault and show that the creep estimates agree to within 1.5 mm LOS displacement and 0.5 mm/yr LOS velocity.

1.2 Thesis Roadmap

In Chapter 2 we provide a brief overview of InSAR and in Chapter 3 present a detailed overview of mathematical models used to describe the statistical behavior of persistent scatterers in interferograms. This chapter includes statistical distributions for amplitude and interferometric phase for signal models commonly used for describing PS.

In Chapter 4 we review PS selection techniques in literature so far and introduces the bayesian Maximum Likelihood (ML) PS selection algorithm. We apply the ML PS technique to two regions in the San Francisco Area and show that the algorithm identifies a denser network of PS in non-urban vegetated terrain than other published algorithms. This PS selection technique has been published in *Geophysical Research Letters* (Shanker and Zebker, 2007).

In Chapter 5 we describe two new phase unwrapping algorithms for unwrapping sparse data. The first technique involves a simple reduction of a sparse two-dimensional phase unwrapping problem into a regularly sample two-dimensional phase unwrapping problem that can be solved with any generic phase unwrapping algorithm. This method has been published in *IEEE Geoscience and Remote Sensing Letters* (Shanker and Zebker, 2008). Next, we describe a new linear programming formulation that relies on the edges of an unwrapping grid as a basic construct. This unwrapping formulation is more flexible than conventional network programming approaches and can incorporate additional geodetic information as constraints in the unwrapping process. We apply this unwrapping technique to estimate the time-dependent creep

across the Central San Andreas Fault. This technique has been published in the *Journal of Optical Society of America A* (Shanker and Zebker, 2010).

In Chapters 6 and 7 we compare the performance of our PS-InSAR algorithms with the SBAS algorithm. In Chapter 6, we apply our techniques to study rockslides in Lyngen region of Norway and present a one-to-one comparison with SBAS results processed at Northern Research Institute (NORUT), Norway. This detailed comparison has been published in *Remote Sensing of the Environment* (Lauknes *et al.*, 2010). In Chapter 7 we present a pixel-by-pixel comparison of our PS-InSAR results and SBAS results from IREA-CNR, Italy. We also compare our PS-InSAR estimates against creep measurements from alignment arrays along the Hayward Fault. A paper describing this comparison in detail has been submitted to *IEEE Geoscience and Remote Sensing Letters*.

Finally, in Chapter 8 we provide a dissertation summary and suggestions for future work.

Chapter 2

InSAR : Background

Persistent Scatterer Synthetic Aperture Radar Interferometry (PS-InSAR) is a family of extensions to the Interferometric Synthetic Aperture Radar (InSAR) technique, that allow us to estimate a deformation time-series for regions that are traditionally considered decorrelated under conventional InSAR techniques. In this chapter, we review the traditional InSAR technique for studying ground deformation and its associated shortcomings. We also review multi-temporal InSAR methods that have been developed to address the shortcomings of standard InSAR and discuss their strengths and weaknesses.

2.1 History

The word "radar" itself is an acronym for radio detection and ranging. Radar systems were initially developed in the first half of the 20^{th} century to determine the position or course of a moving object like an ocean-going vessel or an airplane. Pulse compression signal processing techniques have been traditionally used to improve the signal to noise ration and then locate targets with an error of few meters (Cumming and Wong, 2005; Soumekh, 1999). Synthetic Aperture Radar (SAR) is an extension of the mapping radar that creates a highly directional beam using sophisticated signal processing to combine information from multiple echoes to accurately estimate the azimuth position of the target as well. The synthetic aperture concepts enable us to

image with a resolution on the order of meters with relatively small physical antennas. As a result, SAR is an excellent tool for high resolution remote sensing of the Earth's surface from space. After experimenting with airborne SAR instruments in the 60s and 70s, NASA launched the first space-borne SAR satellite SEASAT in 1978 for ocean studies (Fu and Holt, 1982).

2.2 Synthetic Aperture Radar

Airborne and spaceborne SAR systems typically have a fixed side-looking antenna that illuminates a strip or swath parallel to the sensor's ground track with a series of monochromatic microwave pulses (Figure 2.1). The platform's flight direction is called the azimuth direction and the direction of the main lobe of the transmitting antenna is called the range direction. The antenna, when inactive between transmission of pulses, is designed to receive the scattered echoes from the illuminated surface of earlier transmitted pulses. From antenna theory, the area illuminated on the ground is inversely proportional to the physical shape and dimensions of the antenna (Skolnik, 2001). Therefore, to obtain fine azimuth resolution in real-aperture radar systems we would need a very long antenna.

SAR is an alternative solution to using a long physical antenna. The SAR concept separates two targets at the same range but different azimuth positions by their different relative velocities with respect to the moving platform. The reflected monochromatic waves from two different scatterers in the same illuminated beam have different Doppler shifts or phases associated with them. Using the knowledge of the path of the imaging platform, we can compute the exact phase history for every point target on the ground. We combine information from multiple echoes, effectively creating a synthetic longer aperture (Figure 2.2) to separate targets within the same illuminated beam. Resolution is dependent on the total amount of phase information available for each target. The longer a target is illuminated, the better is our ability to resolve it. Thus, SAR enables us to create high resolution images using small

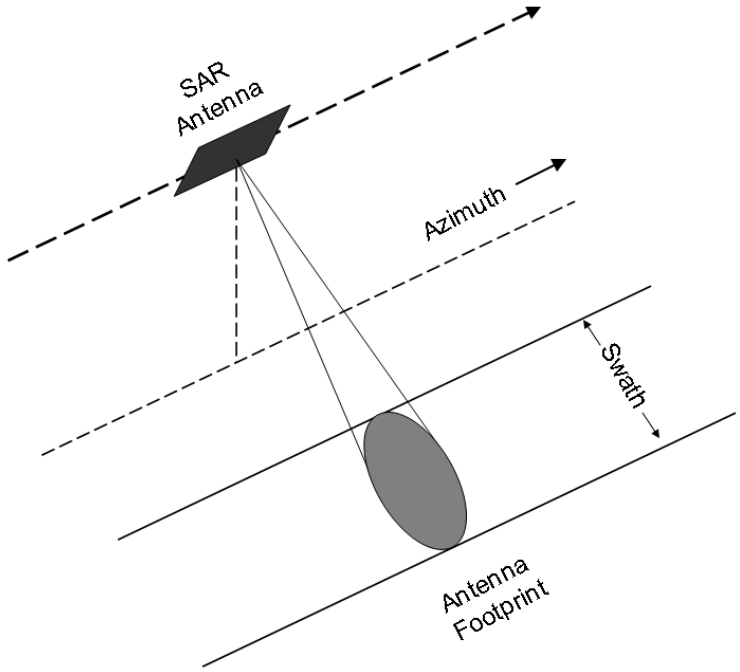

Figure 2.1: SAR imaging geometry

physical antennas. There are numerous published algorithms (Cumming and Wong, 2005; Soumekh, 1999) that can be used to process the recorded echoes to create high resolution images using the SAR concept.

The imaging geometry shown in Figure 2.1 is called the stripmap mode and is the most common. Modern phased-array antennas implement complicated data acquisition strategies, e.g, ScanSAR and spotlight SAR, to increase the area imaged by the radar platform. The output from SAR processing algorithm is a single look complex (SLC) image, a two dimensional array of complex numbers, representing the brightness and phase of the scatterers on the ground. The indices of pixels in the matrix are directly related to the azimuth and range position of the scatterers with respect to a reference point on the platform's path.

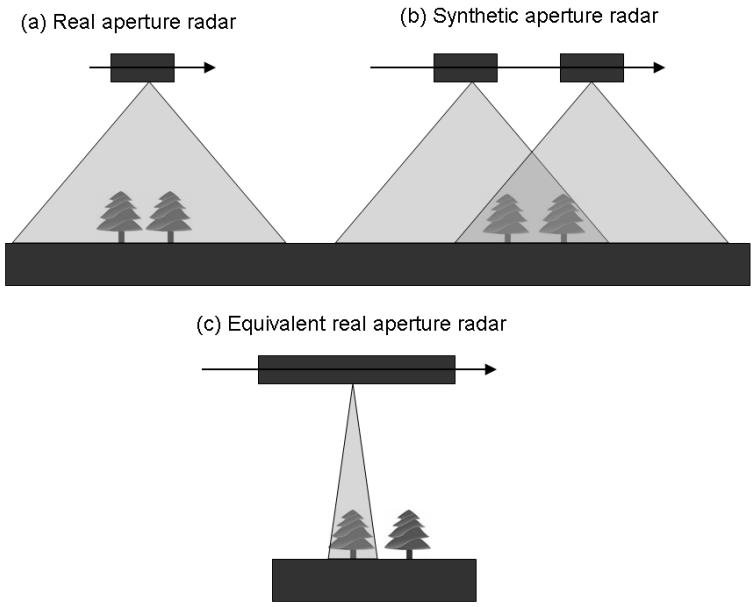

Figure 2.2: (a) Real aperture antenna, (b) Synthetic aperture antenna created by combining information from many pulses and (c) a real aperture antenna that is equivalent to the synthetic aperture antenna.

2.3 SAR Interferometry

Synthetic aperture radar interferometry (InSAR) exemplifies multiplicative interference. The almost monochromatic nature of the scattered echoes enables us to combine the phase information from two or more SAR images acquired over the same area either simultaneously or at different times. The two SAR images are generally acquired from slightly different imaging geometries. The second SLC must be precisely coregistered and resampled to the geometry of the first SLC (Zebker and Goldstein, 1986; Sansosti *et al.*, 2006). The interferometric phase is then computed by multiplying the first SLC with the complex conjugate of the coregistered second SLC. The resulting complex valued image is called an interferogram (IFG). Ignoring any time delays in the imaging hardware, the estimated interferometric phase can be directly related to the difference in path length to a target from the imaging platform in the line of sight (LOS) direction (Figure 2.3).

$$\Delta\phi = -\frac{4\pi}{\lambda}\Delta\rho \tag{2.1}$$

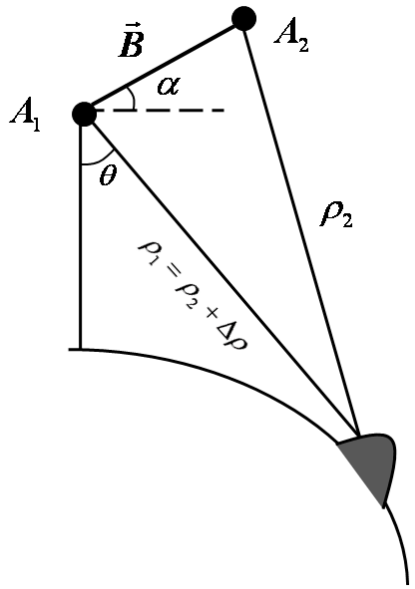

Figure 2.3: SAR interferogram imaging geometry in the plane normal to the flight direction.

Figure 2.4 shows an example interferogram computed over the Cotton Bowl basin in Death Valley (California) using two SAR images acquired using the SEASAT satellite. The interferometric phase map shown in Figure 2.4 can be decomposed into following components:

$$\Delta\phi = \phi_{base} + \phi_{topo} + \phi_{defo} + \phi_{atm} + \phi_{noise} \tag{2.2}$$

where ϕ_{base} is the phase difference due to the baseline between the positions of the satellite corresponding to the two acquisitions, ϕ_{topo} is due to topography, ϕ_{defo} is due to ground deformation, ϕ_{atm} is due to atmospheric delay, and ϕ_{noise} is due to other terms including the ionosphere and system noise.

For mapping topography, all terms besides ϕ_{base} and ϕ_{topo} are treated as noise (Zebker and Goldstein, 1986).

$$\phi_{base} + \phi_{topo} = -\frac{4\pi}{\lambda} B \sin(\theta - \alpha) \tag{2.3}$$

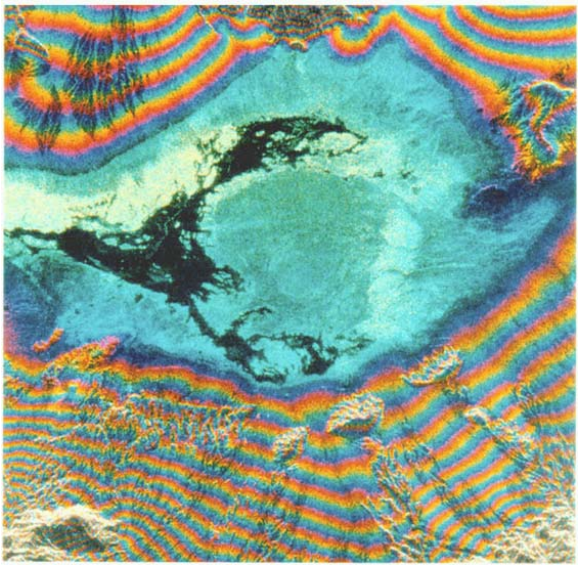

Figure 2.4: Example interferogram of the Cotton Bowl basin in Death Valley, CA (Goldstein *et al.*, 1988). The salt flats in the center of the image show no fringes whereas topographic fringes are clearly visible on the hills surrounding the basin.

where θ is the look angle and α is the angle that the baseline subtends with the reference horizontal plane as shown in Figure 2.3 (Rosen *et al.*, 2000). In fact, InSAR was first developed to map the Earth's topography (Zebker and Goldstein, 1986) and was the technology behind the Shuttle Radar Topography Mission (SRTM) (Farr *et al.*, 2007). As can be seen in Figure 2.4, interferometric phase can only be determined modulo 2π. To obtain a continuous interferometric phase map, the differential phase between all neighboring pixels is integrated. This process is called "phase unwrapping" and is discussed in detail in Chapter 5. The unwrapped phase can then be converted to topography by inverting Equation 2.3.

For crustal deformation studies, ϕ_{defo} is the only term of interest and other terms are either corrected for or treated as noise. ϕ_{base} can be estimated using precise orbit information and an elliptical or spherical model for the Earth's surface. The slightly different imaging geometries also produce a slight parallax, if the area has topography. A digital elevation model (DEM) such as from the Shuttle Radar Topography Mission (SRTM) (Farr *et al.*, 2007) or another interferogram (Gabriel *et al.*, 1989) of the same area can be used to estimate the ϕ_{topo} term. This technique is called "Differential

Interferometry" or D-InSAR. This was first successfully applied to study the Landers earthquake (Massonnet *et al.*, 1993; Zebker *et al.*, 1994).

2.4 Limitations of conventional InSAR

D-InSAR has been successfully applied for measuring ground deformation due to active volcanism (Amelung *et al.*, 2000; Pritchard and Simons, 2002), co-seismic motions (Zebker *et al.*, 1994; Simons *et al.*, 2002), post-seismic motions (Pollitz *et al.*, 2001; Jacobs *et al.*, 2002), mining and groundwater induced deformation (Amelung *et al.*, 1999), and creeping faults (Ryder and Bürgmann, 2008; Bürgmann *et al.*, 2000). The quality of our deformation estimates, measured by a quantity called "correlation" (Zebker and Villasenor, 1992), also depends on the nature of the surface being imaged itself. Change in the surface reflectivity with time or "temporal decorrelation", due to vegetation or melting of snow or other natural phenomena, decorrelates the measurements significantly rendering the phase measurements unreliable. As a result, most conventional InSAR studies tend to focus on dry and sparsely vegetated regions, for example the southwest of the U.S., the Middle East and Tibet.

Degradation of the quality of interferometric phase or decorrelation also occurs due to the variation in imaging geometry. Difference in incidence angles results in the wavelets from the scatterers from a resolution element on the ground adding up slightly differently and the measurements are not reproduced exactly. This is called "spatial decorrelation" (Zebker and Villasenor, 1992) and increases with increasing perpendicular component of baseline. A similar effect is also observed when the imaging tracks for the two acquisitions are not completely parallel, producing "rotational decorrelation". A corresponding geometrical effect also occurs due to a change in the squint angle, the angle with which the spacecraft points forward or backward. The change in squint angle is characterized by a change in the SAR Doppler frequencies leading to decorrelation. Although many of these decorrelation effects can be minimized by filtering, there are critical limits on the baseline and Doppler

frequency differences beyond which no interferometric phase information can be retrieved (Zebker and Villasenor, 1992). In short, the number of usable interferogram pairs are limited by temporal and geometric decorrelation effects, effectively reducing the temporal resolution of regularly acquired SAR data sets.

We denote the atmospheric phase "screen" (ϕ_{atm}) as the variation in the delay of the signal as the signal propagates through the atmosphere, which introduces a variable phase over the image (Hanssen, 2001). Most of the variation in the the atmospheric phase term is due to the variation in the water vapor distribution over the scene, and is often correlated with the topography of the area (Onn and Zebker, 2006). As the SAR acquisitions are separated by about 30 days, the atmospheric phase screen at the two SAR acquisitions is essentially uncorrelated in time. A common method of reducing the effects of the atmosphere is to combine information from various interferograms using multi-temporal InSAR techniques, as described in the next section. Errors in the known position of the imaging platform affect the baseline estimates and typically manifest themselves as phase ramps in the final interferograms. These phase ramps are a result of the wrong ϕ_{base} used in phase correction stage. Such ramps can be easily corrected by computing the fringe rate over flat areas with no expected deformation and applying the correction over the entire image. Residual errors from the phase ramp correction stage cannot be distinguished from the atmospheric phase screen and multi-temporal InSAR techniques need to be used to mitigate their effects.

2.5 Multi-temporal InSAR

Multi-temporal InSAR techniques are extensions of conventional InSAR aimed at addressing the problems caused by decorrelation and atmospheric delay. These techniques involve the simultanoues processing of multiple SAR acquisitions over the same area to allow for the correction of uncorrelated phase noise terms and hence, reduce errors associated with the deformation estimates. Currently, multi-temporal

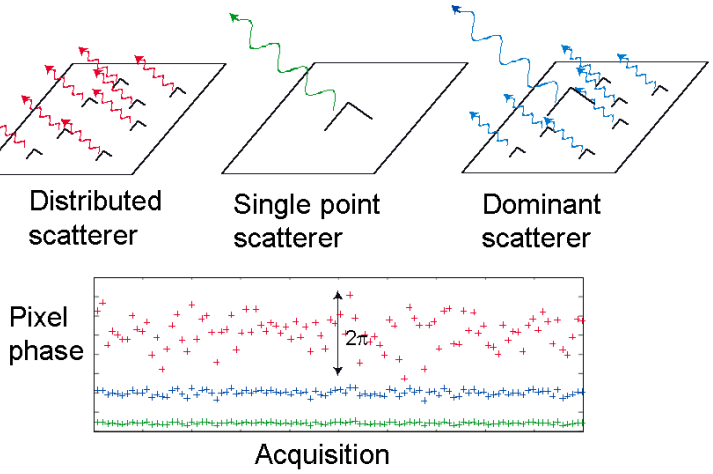

Figure 2.5: Scattering mechanism models for a SAR resolution element - distributed scatterers (red), ideal single point scatterer (green) and persistent scatterer (blue). The persistently scattering pixel exhibits smaller phase variation than the distributed scattering pixel.

InSAR algorithms can be broadly classified into two categories - *persistent scatterer (PS)* and *small baseline (SBAS)* methods. Each of these set of methods is designed for a specific type of scattering mechanism.

The signal return from each resolution element on the ground depends on the distribution and reflectivity of scattering centers within the element. Since we use a monochromatic source, the reflected signal from each resolution element is the coherent sum of individual wavelets scattered by numerous discrete scattering centers within the element (Figure 2.5). Consider the effect of decorrelation by letting scatterers in a resolution element move randomly with respect to the imaging platform due to geometric and temporal decorrelation effects. If the resolution element were composed of a single point scatterer (Figure 2.5), the received signal shows very little variation with time. If this is the case, all interferograms can be used for estimating deformation and we are able to estimate ground motion without error. But in reality, such point scatterers rarely exist.

If all the scatterers are of comparable strength (Figure 2.5), then the interferometric phase realizations are randomly distributed in the interval $[-\pi, \pi)$. In such cases, we can improve the signal-to-noise ratio (SNR) by averaging the interferometric

signal from adjacent resolution elements. Under this assumption random phase contributions due to movement of scattering elements cancel out, leaving behind the phase due to the average motion of the averaged resolution elements. This forms the basis of short baseline (SBAS) methods. Stacking (Sandwell and Price, 1998) is one of the simplest forms of SBAS methods. It determines an average velocity model by averaging numerous interferograms with short orbital baselines to mitigate atmospheric effects. Newer algorithms based on singular value decomposition and temporal models (Berardino *et al.*, 2002) have since been developed to estimate non-linear deformation from a stack of interferograms.

On the other hand, if one of the scatterers in the resolution element is brighter than the others (Figure 2.5), the interference from other scatterers is minimal, the received signal is stable, and the motion of the dominant scatterer can be determined from the interferometric phase. Such pixels form the model for Persistent Scatterer (PS) InSAR (Ferretti *et al.*, 2001). PS methods apply statistical techniques to identify pixels with a single dominant scatterer that are relatively less affected by decorrelation, and use the associated interferometric phase to infer a deformation time-series. For maximizing our ability to identify such resolution elements, all interferograms are analyzed at the highest possible resolution.

A detailed overview of the mathematical models used for PS-InSAR is provided in Chapter 3. We also briefly describe popular PS-InSAR algorithms, most importantly the Stanford Method for PS (Hooper, 2006) framework that forms the scaffold on which rests the research described in this thesis.

Chapter 3

Mathematical modeling of persistent scatterers

In this chapter, we describe in detail the mathematical models of scattering behavior of persistently scattering pixels and derive the associated PS pixel amplitude and interferometric phase statistics. We present models developed in earlier literature as well as new ones developed during the course of this work. We introduce a physical model for describing the nature of various components of observed interferometric phase of a PS pixel. In the last section, we describe the salient features of the Stanford Method for PS (StaMPS) framework (Hooper, 2006), which is used to estimate the various phase components of the physical model. Our phase-stability based PS selection techniques described in Chapter 4 builds on the StaMPS framework.

3.1 Introduction

Conventional InSAR (Section 2.3) is an effective method for measuring deformation in areas of good coherence (Massonnet *et al.*, 1993; Zebker *et al.*, 1994). A closer examination of any interferogram covering vegetated areas or areas prone to changes in surface properties reveals the degradation of the quality of interferometric phase due to changing surface properties with time, resulting in a loss of coherence (Zebker and Villasenor, 1992). Variation in signal properties results from changes in the

relative reflectivity of the scatterers and their relative positions within a resolution element. If the scattered signal from a resolution element is dominated by a single scatterer, the backscattered signal from the element is fairly consistent as described in Section 2.5, and is less affected by spatial and temporal decorrelation. Hence, a network of such single scatterer-dominated pixels may be used to extract deformation signatures from interferograms that have been severley compromised by decorrelation.

The backscattered signal from each resolution element is represented by two physical measures - the amplitude and the phase. We denote pixels that exhibit statistical invariance in the observed SAR amplitude or interferometric phase over a stack of SAR images as *Persistent Scatterers* (PS). A single point scatterer over a perfectly dark background exhibits absolute invariance in the observed signal characteristics due to differences in imaging geometry and with time. As the background or the non-dominant scatterers in a resolution element get brighter, the variance of the observed signal characteristics increases. We use mathematical models described in this section to quantify this variation in signal properties and infer the strength of the single dominant scatterer relative to the cumulative strength of the other scatterers in the resolution element.

Observed interferometric phase measurements are affected by the imaging geometry, topography, atmospheric propagation and scatterer displacement or deformation. In time-series InSAR, we deal with the problem of estimating a time-series of surface deformation from a series of interferograms. A digital elevation model (DEM) and precise orbit information are used to model and remove phase contributions due to geometry and topography. Errors in the DEM and precise position of the imaging platform also contribute to the observed interferometric phase. Hence, the interferometric phase of a pixel (ϕ_{int}) in a differential interferogram can be represented by (Hooper *et al.*, 2004)

$$\phi_{int} = \phi_{def} + \Delta\phi_{\epsilon} + \phi_{atm} + \Delta\phi_{orb} + \phi_{n} \tag{3.1}$$

where ϕ_{def} represents the phase due to deformation, $\Delta\phi_{\epsilon}$ refers to the error introduced by using imprecise topographic information, $\Delta\phi_{orb}$ refers to the error introduced due to the use of imprecise orbits in mapping the contributions of Earth's ellipsoidal surface, ϕ_{atm} corresponds to the difference in atmospheric propagation times between the two acquisition used to form the interferogram and ϕ_n represents the phase noise due to the scattering background and other uncorrelated noise terms. The SAR amplitudes are not affected significantly by the variations in imaging geometry, for baseline values smaller than the critical baseline. Hence, their affects are neglected when modeling SAR signals.

In persistent scatterer interferometry, our primary signal of interest is the return from the dominant scatterer in the resolution element. The echoes from the dimmer distributed scatterers in a pixel is also commonly referred to as "clutter" and contributes to ϕ_n. Signal-to-clutter ratio (SCR) defined as the ratio between the reflected energy from the dominant scatterer to that of the reflected energy from the rest of the resolution element is a measure often used to indicate the strength of the dominant scatterer in SAR pixels. High SCR (¿8) pixels exhibit low interferometric phase variation (¡ 0.25 radians) and vice versa.

In Section 3.2 we describe the models used to describe the interferometric phase components. In Section 3.3, we describe the scattering signal models that are useful in analyzing both amplitude and interferometric phase of SAR pixels. The scattering models in this section only addresses the clutter component (ϕ_n in Equation 3.1) of the interferometric phase.

3.2 Interferometric phase components

In this section, we present phase models used to describe the first four phase components of the estimated phase in differential interferograms (Equation 3.1) (Hooper, 2006; Kampes, 2006). The first four phase components (Equation 3.1)

are systematic and can be estimated accurately for a reasonably dense network of medium signal-to-clutter ratio (SCR) pixels (SCR$\geq$ 2).

3.2.1 Deformation

Deformation (ϕ_{defo}) is the primary phase component or signal of interest in this work. Persistent scatterer InSAR permits estimates of deformation time-series for a region of interest by combining information from multiple SAR acquistions (Ferretti *et al.*, 2001). PS InSAR is an ideal tool for studying the spatial-temporal characteristics of crustal deformation a region of interest, a few square km in size.

Temporal models for deformation like a constant velocity model with or without a sinusoidal component for seasonal ground water fluctuations are often used to simplify the estimation of the relevant deformation signals (Ferretti *et al.*, 2001; Kampes, 2006; Colesanti *et al.*, 2003; Werner *et al.*, 2003). *A priori* information related to the region of interest can also be used to develop structural models for deformation signal estimation (Shanker and Zebker, 2010).

In this work, we use the StaMPS framework (Hooper, 2006) which provides a means of estimating the deformation of a region of interest by assuming that deformation has a long wavelength spatial and low frequency temporal structure (Section 3.4). Phase contributions due to the scatterer geometry errors (Section 3.2.2), atmospheric propagation (Section 3.2.3) and errors in the precise orbits (Section 3.2.4) affect the deformation phase estimates from a single interferogram (Hanssen, 2001). PS-InSAR uses information from multiple interferograms to separate out the deformation phase signal from these other phase contributions.

3.2.2 Geometric phase component ($\Delta\phi_\epsilon$)

The phase contributions due to the imaging geometry and topography are removed for interferograms used in time-series analysis by a process called flattening (Section 2.3). This correction is applied in two stages. In the first stage, the phase component due to the Earth's curvature (ϕ_{base} in Equation 2.2) is removed by assuming that all the

scatterers lie on the WGS-84 ellipsoid. In the next stage, a digital elevation model (DEM) of the area in the radar coordinates is used to compute the corresponding phase component (ϕ_{topo} in Equation 2.2). This second processing stage contains two types of topography-related errors in the processed differential interferograms: DEM error and sub-pixel position error.

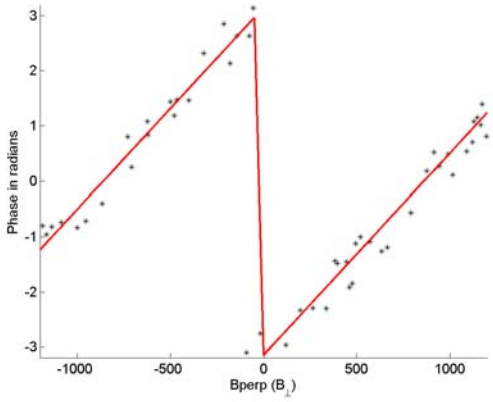

Figure 3.1: Example inversion of observed interferometric phase (black dots) for geometric phase components (solid line) as a function of the perpendicular baseline.

DEM error

Using an approximate DEM can introduce systematic phase artifacts. In many active regions of the planet, the topography has significantly changed by a few meters from the time when the digital models were created, for example using SRTM data (Farr *et al.*, 2007). If Δh is the error in the DEM used, the corresponding phase error (Kampes, 2006) is

$$\Delta\phi_\epsilon = \frac{4\pi}{\lambda} B_\perp(\theta) \frac{\Delta h \sin(\theta)}{r} \tag{3.2}$$

where $B_\perp$ represents the perpendicular baseline, r represents the absolute one way range from the satellite to the pixel under consideration and θ represents the look angle.

All the data sets discussed in this thesis were acquired using the ERS and EnviSAT satellites. The baselines of both the European Space Agency (ESA) satellites are well controlled and do not exhibit a systematic drift in baselines. This is not the case for

most SAR systems, including the ALOS PALSAR system, which has a characteristic baseline drift. If the perpendicular baselines are correlated with time and the area being analyzed is characterized by steady deformation, the effects of the deformation phase component and the geometric error components are indistinguishable.

Sub-pixel range position error

Range resolution (Δr) is one of the important performance characteristics of a SAR system and limits the accurate positioning of a dominant scatterer in a SAR image. The location of the dominant scatterer in a radar pixel may not always correspond to the center of the mapped pixel location on the ground. Hence, if the dominant scatterer within a SAR pixel is located at a distance ε from the center of the pixel, the corresponding systematic phase offset (Kampes, 2006) is given by

$$\Delta\phi_{\epsilon} = \frac{4\pi}{\lambda} B_{\perp}(\theta) \frac{\varepsilon \cos(\theta)}{r} \tag{3.3}$$

Since both the phase terms 3.2 and 3.3 have the same functional relationship with the perpendicular baseline and the look angle, they are indistinguishable. For most deformation monitoring applications, the additional processing step of distinguishing between the height and the sub-pixel position components is not necessary. The combined phase contributions can be estimated using a non-linear estimator as shown in Figure 3.1 (Hooper, 2009). It is not possible to use a simple linear estimator due to the possible wrap around of phase as a result of large perpendicular baseline values or DEM errors.

Sub-pixel azimuth position error

An error term similar to the DEM error and sub pixel range position arises if the acquisition squint angles are different for the scenes combined to form an interferogram and the dominant scatterer is not located at the center of the SAR pixel. The sub-pixel azimuth position error only produces a systematic phase offset

if the SAR scenes are processed to a geometry that is different from the acquisition geometry. For time-series InSAR, the SAR scenes are often processed to the zero-Doppler geometry for reducing data volume and hence, only the range difference to the center of the SAR pixels are used for phase compensation. If the dominant scatterer is offset from the pixel center by a distance of η in the azimuth direction, the corresponding systematic phase shift is given by

$$\Delta\phi_\nu = \frac{2\pi}{v} \cdot \Delta F_{DC} \cdot \eta \tag{3.4}$$

where ΔF_{DC} corresponds to the difference in the Doppler centroid frequencies of the slave and the master scenes, and v corresponds to the velocity of the SAR platform (Kampes, 2006). The data sets discussed in this thesis were acquired using the ERS and Envisat satellites, which are characterized by slow drift in the Doppler centroid. Hence, the phase component is correlated with the time-difference between acquisitions and can be mistaken for time-dependent deformation. These phase errors are much smaller in magnitude (order of 0.2 radians) than deformation and hence, we treat it as noise. We do not attempt to correct for these systematic offsets. An oversampling and local maxima detection approach (Ketelaar, 2009) can be used to determine the sub-pixel position of the dominant scatterer and the corresponding phase corrections can be applied if needed.

3.2.3 Atmospheric phase screen

The dominant error source in many interferograms results from the spatial heterogeneity of the wet component of atmospheric refractivity, resulting in excess path length of the radar signal propagating through the neutral atmosphere (Goldstein, 1995; Onn and Zebker, 2006). The atmospheric phase signal varies gradually over space and is often modelled as a long wavelength component in unwrapped phase (Hooper, 2006; Onn and Zebker, 2006). Emardson et al. (2003) estimated the correlation function of the atmospheric phase screen using InSAR and GPS data, and for data

over Southern California estimated a phase difference of approximately one radian at 1 GHz for points separated by a distance of two km.

It has been shown that the atmospheric propagation delay between two points increases exponentially with the distance separating them, almost linearly with their altitude difference and is independent of the wavelength (Emardson *et al.*, 2003; Onn and Zebker, 2006). We ignore the systematic variation of the tropospheric phase delay due to topography in most cases and treat it as spatially correlated noise (Hooper, 2006) unless specifically mentioned otherwise. This is a reasonable assumption as the topgraphy in most areas that we analyze in this work do not vary by more than 500 m over the area of interest. In regions, where the topography varies significantly over the scene of interest, we use a model in which the tropospheric phase delay is linearly proportional to the altitude of the SAR pixel. More details of this correction technique will be presented below as a part of the discussion of results corresponding to landslides in Norway (Chapter 6).

3.2.4 Orbital errors

The positions of the SAR platform must be known with sub-meter accuracy for precise determination of baselines and accurate topographic phase correction (Rosen *et al.*, 2000). Geographically correlated orbit errors, like those due to gravity models cancel each other out in baseline computations (Hanssen, 2001). However, non-conservative forces like time-variable drag and time-variable solar radiation pressure cannot be modelled accurately in the current precise orbit determining systems (Scharroo and Visser, 1998). This error in the precise positions of satellites also propagates into the baseline calculations, and hence affects the topographic phase correction and the Earth ellipsoid correction.

Along-track position error

Along-track positioning errors can be corrected in the coregistration process, where the absolute shift between the two SAR scenes in the azimuth direction are also

estimated. The across-track error of the master scene affects the DEM (in radar coordinates) that is used to generate the differential interferogram. However, these errors are in the order 1-2 m, which is significantly smaller than the SRTM DEM spacing of 30 m (Farr *et al.*, 2007). Hence, the phase error due to the approximate DEM is expected to be small. This DEM error (Equation 3.1) can be estimated as they are correlated with the perpendicular baseline values. The across-track orbit errors produce systematic errors and can be estimated from the data itself.

Across-track position error

The interferometric phase is much more sensitive to across-track errors than along-track errors and particularly, those in the vertical direction. These errors manifest as a phase ramp superimposed over the actual interferometric phase, as the incorrect baseline is used for correcting the contribution of the spherical or ellipsoidal earth ($\Delta\phi_{base}$ in Equation 2.2). These errors introduce a fairly gentle phase ramp when precise orbits are used with ERS or Envisat data (Scharroo and Visser, 1998). This signal is indistinguishable from phase gradients introduced by the atmospheric phase delays or long wavelength deformation (Hanssen, 2001). When analyzing areas of 40 km $\times$ 40 km in size, as is typical in this work, we do not encounter any large phase ramps and treat this phase component as noise that is indistinguishable from the atmospheric component. Occasionally, large phase ramps are encountered which can be corrected by fitting a plane or a parabolic surface to the unwrapped interferogram (Hanssen, 2001) or by explicitly counting fringes in the wrapped inteferogram (Kohlhase *et al.*, 2003). However this method can be severely limited by presence of large decorrelated areas (Kohlhase *et al.*, 2003) and in vegetated terrain.

3.2.5 Other phase terms

We have, so far, described all the systematic phase components that affect the observed differential interferometric phase (Equation 3.1). There are numerous other phase aberrations introduced by the SAR and InSAR processing implementations

(Bamler and Just, 1993). Various effects such as geometric misregistration, defocusing in azimuth and errors in range migration can introduce phase aberrations. With improved SAR processing algorithms and improved precise orbit determination, many of these artifacts are effectively reduced. Yet in combination with thermal noise, these factors contribute to an interferometric phase noise "floor". These effects are less apparent in conventional multi-looked interferograms where the signal-to-noise ratio (SNR) is boosted by averaging pixels. These effects are more visible when handling single-look interferograms (see Chapter 7). These small phase effects are treated similar to the scatterer noise (ϕ_n), as they are assumed to be uncorrelated with time.

3.3 Scattering Signal Models

The phase noise (ϕ_n) term in Equation 3.1 can be primarily attributed to non-dominant scatterers in the resolution element. Published PS-InSAR algorithms generally represent this phase component using one of two PS signal models - the constant signal model and the Gaussian signal model. In this section, we discuss the probability distribution functions (PDFs) for the distribution of the SAR pixel amplitude and scatterer phase noise for both of these signal models. PS pixels can be defined as those resolution elements in a series of SAR images that are less affected by scatterer noise and other noise factors.

These signal models represent the signal return from the resolution elements. These signals are also affected by atmospheric propagation and other physical noise sources before reaching the SAR antenna. For simplicity, we can group all temporally and spatially uncorrelated noise sources with the scatterer noise.

3.3.1 Constant Signal Model

This signal model for persistent scatterers was first suggested by Ferretti *et al.* (2000) and Ferretti *et al.* (2001). Let $z = 1 + n$ represent the return from a single resolution element in a single look complex SAR image. The radar return from the dominant

scatterer is assumed to be a constant, over a small range of imaging geometries and baseline, and is normalized to unity. "n" represents the noise from the other scatterers and uncorrelated noise sources. The noise term is assumed to be circular Gaussian (complex number with the real and imaginary parts represented by i.i.d zero mean Gaussian variables) with variance σ_n^2. The SCR of this signal model is given by $1/\sigma_n^2$.

SAR amplitude

The amplitude of the signal ($b = ||z||$) is given by the Rice distribution (Papoulis, 1991) and can be defined using the modified Bessel function (I_0) as follows:

$$f_b(b) = \frac{2b}{\sigma_n^2} \cdot I_0\left(\frac{2b}{\sigma_n^2}\right) \cdot e^{-\left(1+b^2\right)/\sigma_n^2} \tag{3.5}$$

SAR pixel phase

The corresponding SAR pixel phase ($\angle z = \theta$) distribution can be written in terms of error functions (Abramowitz and Stegun, 1972):

$$f_\theta(\theta) = \frac{1}{2\pi} \exp\left(-\frac{\sin^2\theta}{\sigma_n^2}\right) \cdot \left[\exp\left(\frac{-\cos^2\theta}{\sigma_n^2}\right) + \sqrt{\frac{\pi}{\sigma_n^2}} \cdot \cos\theta \cdot \operatorname{erfc}\left(-\sqrt{\frac{1}{\sigma_n^2}} \cdot \cos\theta\right)\right] \tag{3.6}$$

InSAR pixel phase

The intereferometric phase distribution corresponding to this signal model does not have a simple closed form expression. A derivation of a semi-analytical solution for this PDF is presented from first principles in this work. If $z_1 = r_1 \cdot e^{j\theta_1}$ and $z_2 = r_2 \cdot e^{j\theta_2}$ represent the signal return from two different SAR images for the same resolution element or pixel, then the distribution of the interferometric phase ($\phi_n = \angle(z_1 \cdot z_2^*)$) can be derived starting from the SAR pixel phase (Equation 3.6) as shown below. As the phase observations in the individual SAR images are independent, we write joint distribution of two independent SAR phase observations θ_1 and θ_2 as

$$f_{\theta_1,\theta_2}(\theta_1, \theta_2) = f_\theta(\theta_1) \cdot f_\theta(\theta_2) \tag{3.7}$$

ϕ_n and ϕ_{sum}, a new random variable, can be defined in terms of θ_1 and θ_2 as

$$\begin{aligned} \phi_n &= (\theta_1 - \theta_2)_{2\pi} \\ \phi_{sum} &= (\theta_1 + \theta_2)_{2\pi} \end{aligned} \tag{3.8}$$

We now apply this transformation to obtain the joint PDF of ϕ_n and ϕ_{sum}. The modulo 2π operation, represented by $(\cdot)_{2\pi}$, ensures that ϕ_n and ϕ_{sum} are restricted to $[-\pi, \pi)$. The tranformation uses the Jacobian of Equation 3.8 (Papoulis, 1991) and is given by

$$f_{\phi_n,\phi_{sum}}(\phi_n, \phi_{sum}) = \frac{1}{2}\left[\begin{array}{l} f_{\theta_1,\theta_2}\left(\frac{\phi_n+\phi_{sum}}{2}, \frac{\phi_{sum}-\phi_n}{2}\right) \\ +f_{\theta_1,\theta_2}\left(\frac{\phi_n+\phi_{sum}}{2}+\pi, \frac{\phi_{sum}-\phi_n}{2}+\pi\right) \end{array}\right] \tag{3.9}$$

Equation 3.9 can be numerically integrated over ϕ_{sum} to yield the PDF of the the phase difference ϕ_n as follows:

$$f_{\phi_n}(\phi_n) = \int_{-\pi}^{\pi} f_{\phi_n,\phi_{sum}}(\phi_n, \phi_{sum}) \cdot d\phi_{sum} \tag{3.10}$$

These probability distribution functions can be pre-computed for various noise levels (σ_n^2) and stored for later applications. PDFs of the SAR amplitude and interferometric phase for various values of SCR (γ) are shown in Figure 3.2.

3.3.2 Gaussian signal model

Let $z = s + n$ represent the return from a single resolution element in a single look complex SAR image. In this case, the return from the dominant scatterer is also modeled by a circular Gaussian random variable, with variance σ_s^2. This assumption was shown to be valid for SAR data by Sarabandi (1992).

SAR amplitude

The amplitude of the signal is characterized by the Rayleigh distribution (Abramowitz

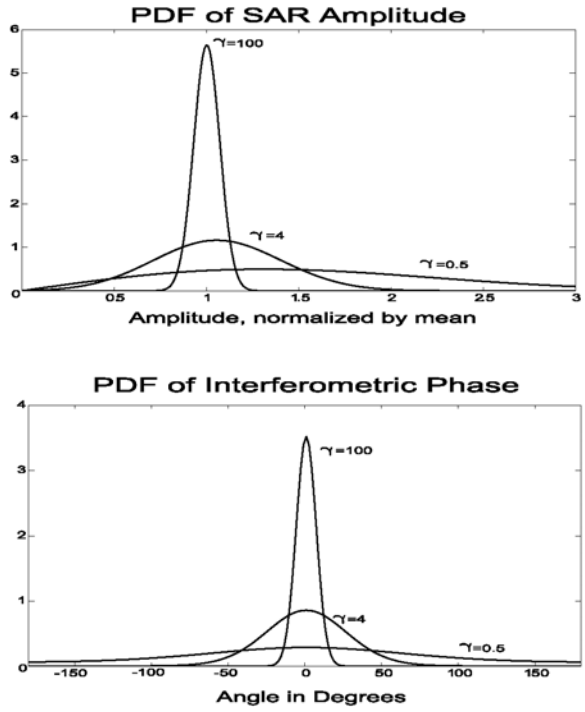

Figure 3.2: (Top) PDFs of the SAR amplitude function and (Bottom) PDFs of the interferometric phase residuals for the constant signal model evaluated for SCR values of 0.5, 4 and 100.

and Stegun, 1972) as follows:

$$f_b(b) = \frac{2b}{\sigma_s^2 + \sigma_n^2} \cdot \exp\left(\frac{-b^2}{\sigma_s^2 + \sigma_n^2}\right) \tag{3.11}$$

Since z is also distributed as a circularly Gaussian variable, the phase of the SAR pixel is distributed as a uniformly random variable over $[-\pi, \pi)$.

Interferometric phase

The PDF of the inteferometric phase of a single look pixel in this model is given by (Just and Bamler, 1994; Lee *et al.*, 1994)

$$f_\phi(\phi) = \frac{1 - |\rho|^2}{2\pi} \cdot \frac{1}{1 - \beta_\phi^2} \cdot \left[1 + \frac{\beta_\phi \cdot \arccos(-\beta_\phi)}{\sqrt{1 - \beta_\phi^2}}\right] \tag{3.12}$$

$$\text{where } \beta_\phi = |\rho| \cdot \cos\phi$$

The magnitude of the interferometric correlation ($|\rho|$) depends on the signal to clutter ratio (SCR or γ) following Just and Bamler (1994) and Lee et al. (1994):

$$\gamma = \frac{|\rho|}{1 - |\rho|} \tag{3.13}$$

PDFs of the SAR amplitude and interferometric phase for various values of SCR are shown in Figure 3.3. Equation 3.12 reduces to a Dirac delta function for perfectly correlated signals($|\rho| = 1$) and to a uniform distribution on $[-\pi, \pi)$ for perfectly decorrelated signals ($|\rho| = 0$).

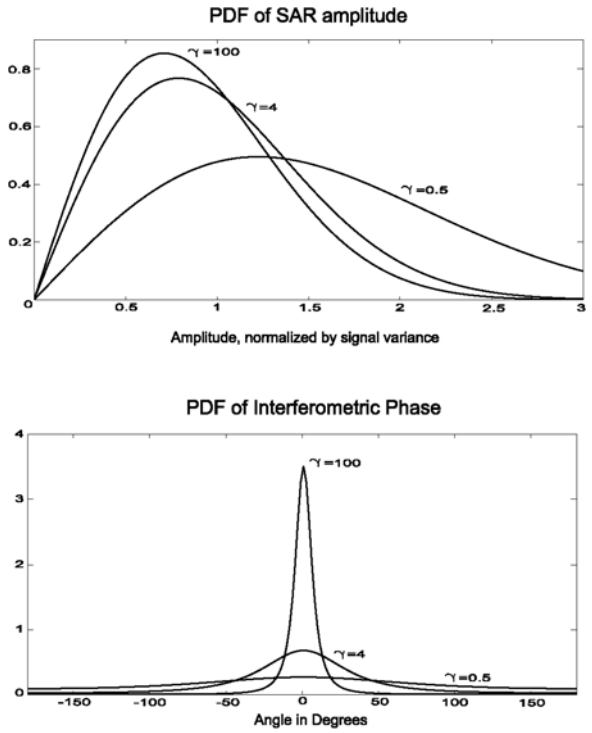

Figure 3.3: (Top) PDFs of the SAR amplitude function and (Bottom) PDFs of the interferometric phase residuals for the constant signal model evaluated for SCR values of 0.5, 4 and 100.

3.4 StaMPS framework

The Stanford Method for PS (StaMPS) framework was initially developed for PS applications in natural terrain (Hooper *et al.*, 2004; Hooper *et al.*, 2007) and since, has been expanded to include short baseline analysis (Hooper, 2008). For PS-InSAR analysis, a set of N common-master interferograms, where the master scene has been chosen to minimize the decorrelation effects (Hooper *et al.*, 2007), is analyzed at the highest possible resolution. We generalize Equation 3.1 to

$$\phi_{x,i} = \phi_{defo,x,i} + \Delta\phi_{\epsilon,x,i} + \phi_{atm,x,i} + \Delta\phi_{orb,x,i} + \phi_{n,x,i} \tag{3.14}$$

where x represents the spatial index of the pixel under consideration in interferogram i and all the other symbols are the same as given in Equation 3.1. PS pixels are again defined as pixels with very little variation in the scatterer noise term ($\phi_{n,x,i}$). The first four terms in Equation 3.14 dominate the scatterer term and need to be reliably estimated for identification of PS pixels. The StaMPS framework is a collection of spatial and temporal filtering routines that allow us to estimate each of these phase components by assuming a spectral structure. Table 3.1 describes the spectral characteristics assumed for each of the phase components. All the observed interferometric phases are wrapped values and hence, the low pass components from Table 3.1 are estimated using a combination of a low pass filter and an adaptive phase filter (Hooper *et al.*, 2007) that preserves the interferometric fringes.

Table 3.1: Spectral characteristics for various phase components of the observed interferometric phase for a PS pixel (Hooper, 2006).

	Component	Spatial Properties	Temporal Properties
$\phi_{defo,x,i}$	Deformation	Low freq	Low freq
$\phi_{atm,x,i}$	Atmosphere	Low freq	High freq
$\Delta\phi_{orb,x,i}$	Orbital errors	Low freq	High freq
$\phi_{n,x,i}$	Scatterer noise	High freq	High freq
$\phi_{\epsilon,x,i}$	DEM Error	High freq	Correlated with baseline

From Table 3.1, it is clear that the deformation signal, atmospheric phase screen and the orbital errors are all spatially correlated and can be estimated simultaneously as a combined term for each interferogram. The DEM error term can be estimated on a pixel-by-pixel basis. The various steps involved in the estimation of the spatially correlated phase terms are shown in Figure 3.4 and described in the following subsections.

3.4.1 Preliminary PS candidate selection

Amplitude dispersion, defined as the ratio between the standard deviation and the mean of the SAR amplitude (Ferretti *et al.*, 2001), is computed on a pixel-by-pixel basis and a preliminary set of candidates are identified with a threshold of typically 0.4 to 0.45. This is a very liberal threshold compared to that typically suggested for PS selection (Ferretti *et al.*, 2001) and primarily eliminates areas over water and heavily decorrelated pixels in vegetated areas. Accurate computation of amplitude dispersion requires precise amplitude calibration of the SAR images using the antenna gain pattern. Since we use a relaxed threshold for candidate selection,we can use a simplified constant calibration factor obtained by averaging the pixel brightness in the SAR images (Lyons and Sandwell, 2003). This candidate selection stage is purely optional, but often decreases the processing time and memory requirements by a factor of ten.

3.4.2 Weighted estimation of correlated phase terms and DEM error

The first three terms in Equation 3.14 are spatially correlated over short distances and can be estimated by spatial filtering of each interferogram. Lyons and Sandwell (2003) showed that the noise in interferometric phase observations can be significantly reduced by weighting the pixel amplitudes by a measure of their stability, before multilooking or adaptive filtering in the complex image domain. Building on this idea,

the amplitudes of the pixels are weighted by the inverse of the amplitude dispersion (Hooper, 2009). Once the spatially correlated terms are estimated and subtracted, the baseline diversity of the stack of interferograms is exploited to determine the phase terms associated with the DEM error ($\Delta\phi_\epsilon$) for each selected candidate pixel in the interferograms. The phase residuals are interpreted as scatterer noise terms ϕ_n for each pixel and used to compute a temporal coherence (ρ_{temp}) measure on a pixel-by-pixel basis as follows:

$$\rho_{temp,i} = \sum_{k=1}^{N} \left[\frac{e^{j\phi_{n,k,i}}}{N} \right] \tag{3.15}$$

We estimate the probability of estimating a similar coherence value for a purely random phase sequence by numerical simulation of a $100,000$ random phased sequences. Hooper *et al.* (2007) empirically observed that the spatially correlated phase estimation is significantly improved and converged faster if the amplitude weights are readjusted using this probability measure. This process is repeated iteratively until the estimated probability values converge (Figure 3.4). For more details of the iterative estimation of correlated phase terms, we refer the readers to Hooper (2006) and Hooper *et al.* (2007).

3.4.3 PS selection

The StaMPS framework is self-sufficient and provides a method for identifying the PS pixels after estimation of the spatially correlated phase terms. However, the most important contribution of the StaMPS method is the estimation of spatially-correlated phase terms as described in the previous section. Figure 3.4 summarizes the various steps involved in estimating the spatially correlated phase terms. In this work, we use our own PS selection algorithms but depend on the ability of the StaMPS framework to reliably estimate spatially correlated phase terms. A detailed discussion of the PS selection techniques is provided in Chapter 4.

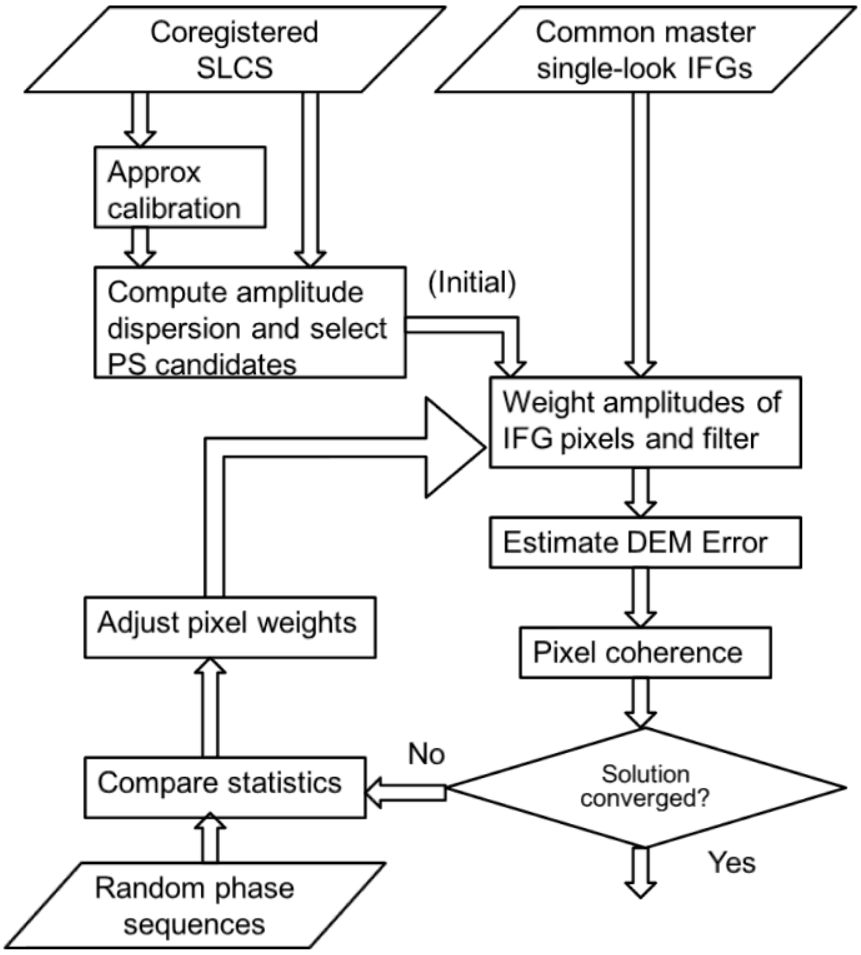

Figure 3.4: The StaMPS framework for estimating spatially correlated phase terms for every PS candiate in each interferogram. The outputs of this processing step include estimates of spatially correlated terms, geometric errors and pixel coherences.

3.4.4 Sidelobe effects

The impulse function of a single target is characterized by sinc functions in the range and azimuth directions. Hence, any SAR image can be represented as a convolution of the reflectivity of the scatterers on the ground and the two dimensional sinc function (Cumming and Wong, 2005). As a result, bright scatterers in the ground dominate the response from the surrounding darker scatterers. To avoid the selection of pixels affected by sidelobes and misinterpretation of systematic phase artifacts as deformation, whenever adjacent pixels are identified as PS, the StaMPS framework

discards the less coherent of these pixels as affected by sidelobes of the brighter and more coherent pixels.

The wrapped phase values corresponding to the final reliable network of PS are then unwrapped and smoothened using appropriate spatial and temporal filters to estimate the line of sight deformation from the stack of interferograms. Phase unwrapping is the subject of a later chapter in this work (Chapter 5).

3.4.5 Other PS frameworks

Many other PS-InSAR algorithms and frameworks have been developed and successfully applied to study temporal characteristics of deformation across the world. The more popular of these include the original Permanent Scatterers^{TM}from Tele-Rilevamento Europe (TRE), the Interferometric Point Target Analysis (IPTA) framework (Werner *et al.*, 2003) from GAMMA software, the GENESIS-PSI system (Adam *et al.*, 2003) from the German Aerospace Center (DLR) and the DePSI system from Delft University of Technology (Kampes, 2006). All these PS systems are designed to identify pixels with stable amplitude characteristics and use amplitude statistics to identify coherent scatterers. StaMPS (Hooper, 2006) was the first framework to consider phase stability as a criterion for coherent scatterer selection and incorporate information from neighboring pixels to determine phase stability of each pixel. The full resolution SBAS (Lanari *et al.*, 2004b) is another full resolution time-series InSAR technique but uses all small geometric baseline interferograms to reduce the effects of decorrelation. As this system does not operate on single-master interferograms, it is technically not a PS system. More details on the PS selection mechanisms of these frameworks will be discussed in Chapter 4.

3.5 Summary

We have presented here two mathematical models – constant signal model and Gaussian signal model, to describe the scattering properties of persistently scattering

pixels. The distribution functions for the SAR amplitudes and interferometric phases for both the signal models have been described. The PDF of the interferometric phase for the constant signal model has been presented for the first time in literature, in this work. These signal models can be used as a reference model for quantifying the relative strength of the dominant scatterer in pixels and for quantifying the variation in signal amplitude and phase. Each signal model represents a slightly different interpretation of the received radar echo, but the PS selection experiments described in Chapter 4 do not indicate that either of the signal models is superior to the other. The two models are almost equivalent with the Gaussian signal model exhibiting roughly twice the phase variation as the constant signal model for the same SCR.

We have also described the salient features of the StaMPS framework (Hooper, 2006) in this chapter. The StaMPS framework is used to model the effects of imaging geometry, atmospheric propagation and orbital errors on the observed interferometric phase in terms of their spectral structure without assuming a fixed functional form.

Chapter 4

Persistent Scatterer Selection

In this chapter we present a new information theoretic approach to PS selection. Building on the mathematical models presented in Chapter 3, we present the most common amplitude-based PS selection methods and then describe our new phase-based approach for identifying PS pixels in a stack of common master single-look inteferograms by comparing the observed interferometric phase against a known mathematical model. Our method identifies a denser PS network in natural terrain than other published algorithms (Shanker and Zebker, 2007).

4.1 Amplitude based PS Selection

In this section, we provide a brief overview of the PS selection methods suggested in literature so far. Most of these PS selection algorithms are amplitude-based and operate on coregistered SAR images.

4.1.1 Amplitude Dispersion

Amplitude dispersion was the first method developed to identify PS pixels in a series of SAR images (Ferretti *et al.*, 2000). The constant signal model (Section 3.3.1) is used to characterize the statistical behavior of PS pixels. For low SCR pixels, the amplitude distribution (Equation 3.5) tends to a Rayleigh distribution (Papoulis, 1991) that depends only on the noise variance (σ_n^2). For high SCR pixels, as is

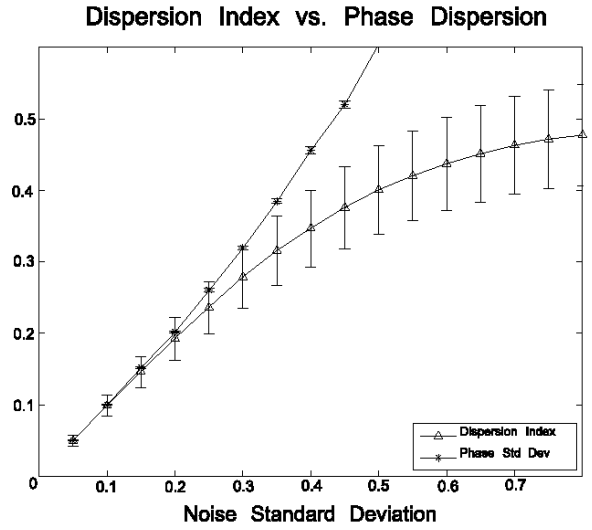

Figure 4.1: Amplitude dispersion ($D_{\mathcal{A}}$) and phase dispersion (σ_ϕ) as a function of increasing noise for the constant signal model (Section 3.3.1) for a simulated stack of 25 interferograms. For low noise values, the two curves track each other well.

often the case in urban regions, the amplitude distribution approaches a Gaussian distribution (Ferretti *et al.*, 2001) and the phase deviation (σ_ϕ) can be approximated by

$$\sigma_\phi \approx \sigma_n = \frac{\sigma_b}{\mu_b} = D_{\mathcal{A}} \tag{4.1}$$

where μ_b and σ_b represent the mean and standard deviation of the SAR pixel amplitude and $D_{\mathcal{A}}$ represents the amplitude dispersion. Figure 4.1 shows the relationship between phase deviation (σ_ϕ) and amplitude dispersion ($D_{\mathcal{A}}$). From this image, it is clear that the one-to-one correspondence between the phase statistics and the amplitude statistics breaks down beyond a dispersion value of 0.25 or a corresponding signal-to-clutter ratio (SCR) value of 8. This selection criterion works well in urban areas where man-made structures have higher reflectivity and hence, high SCR. In natural terrain, there could potentially exist low SCR PS pixels with stable phase characteristics which would not be identified by this method.

Precise radiometric calibration of the coregistered SAR images is essential for reliable estimation of pixel amplitude statistics and the identification of persitent scatterers in the area of interest. In areas with calibrated corner reflectors or

transponders, external calibration (Freeman, 1992) can be applied and the scaling constants for each SAR scene can be obtained by the analysis of uncalibrated SAR scenes themselves (Freeman, 1992). This scaling constant can be derived using the peak power or the integral output of the reference targets (Ulander, 1991). But often, this method cannot be applied for calibrating SAR images due to the absence of calibrated targets in the area of interest.

To overcome this calibration issue, the PS selection is implemented iteratively. If the truly bright targets (PS) correspond to the constant signal model 3.3.1, then their amplitude distribution is given by the Rice distribution. Hence, for each iteration a set of calibration scaling constants can be identified in the least squares sense, such that the observed amplitude characteristics are best fit by a Rice distribution (D'aria *et al.*, 2009). The availability of a large number of SAR scenes can thus be exploited to derive the SAR calibration constants as well. The amplitude dispersion method has also been adapted for other PS frameworks (Kampes, 2006; Crosetto *et al.*, 2003; Lyons and Sandwell, 2003).

4.1.2 Signal-to-Clutter Ratio

This set of PS selection techniques is also inspired by SAR calibration techniques. The SCR approach has been used by researchers at DLR in their GENESIS processing chain (Adam *et al.*, 2003) and at Delft University in the DePSI processing chain (Kampes, 2006). The SAR images are oversampled by a factor of 2 to reduce aliasing effects due to the complex multiplication of the SAR images (Nutricato *et al.*, 2002). The signal-to-clutter ratio (SCR) is estimated by computing the ratio of the power of a PS candidate with that of its immediate neighboring pixels (Adam *et al.*, 2003; Kampes and Adam, 2005). As a result of the oversampling, the sub-pixel position of the dominant scatterer (Ketelaar, 2009) is also estimated during the processing. A typical SCR threshold of 2.0 (Kampes, 2006; Ketelaar, 2009) is used to identify the PS pixels from amongst the candidates. The main advantage of this method is that

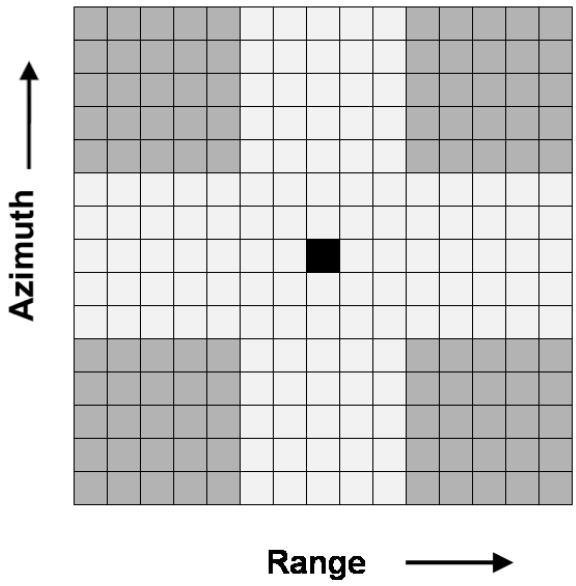

Figure 4.2: The Signal-to-Clutter Ratio for the pixel of interest (black) is computed by ratio of the energy in the sidelobes (white) and the background (gray) in oversampled SAR images.

the SCR determination is independent of the calibration constant as the brightness of each pixel is compared to those of its immediate neighbors.

Implementation of this method in heavily urbanized areas, however, is difficult due to the presence of bright scatterers in close proximity to each other. Sophosticated SCR estimators and filters are needed in such scenarios for effective estimation of PS pixels. Kampes (2006) provides a comparison of the SCR technique against the amplitude dispersion technique.

4.1.3 Scripps technique

The Scripps PS technique (Lyons and Sandwell, 2003) is a not a conventional PS-InSAR technique by definition. It is a filtering framework that uses the amplitude stability characteristics of each pixel to reduce noise in the multi-looked phase of differential interferograms. The cleaner differential interferograms are then used for unwrapping and stacking to determine the average line of sight (LOS) deformation velocity.

The amplitude of the coregistered SAR images are roughly calibrated by normalizing them with the sum of the brightness values of all pixels in the scene of interest. A scattering function (s), defined as the inverse of ampitude dispersion (Section 4.1.1), is computed for each pixel over this set of calibrated coregistered images. The single-look high resolution interferograms are multilooked after scaling the amplitude by s^2 for each of the pixels. These multi-looked interferograms are then unwrapped and averaged to estimate an average velocity. This averaging step can also be interpreted as a simple time-series InSAR technique where a linear temporal deformation model is used. The main difference with the conventional PS-InSAR techniques however, is that this framework allows for use of multi-master multi-looked interferograms. The weighted multi-looking scheme introduced by this technique was the predecessor on which the StaMPS filtering framework described in Section 3.4 was built.

4.2 Elimination using a temporal model

Very often, the criteria mentioned in the previous section are used with liberal thresholds to select a dense network of PS pixel candidates. If reliably unwrapped interferograms are available, all the pixels with unwrapped phase values that do not reasonably fit a pre-determined deformation temporal model can be rejected as non-PS. In the absence of unwrapped interferograms, the time-series of the differences in interferometric phase for pixels in geographical proximity (also called double-differences) are analyzed and a temporal deformation model (typically linear) is used to approximate the interferometric phase (Werner *et al.*, 2003; Kampes and Adam, 2005). Double-difference time-series typically do not involve multiple cycle phase jumps and allows us to work with wrapped data. Mathematically, the method involves the analysis of the spatial gradient of the differential interferometric phase (Equation 3.1)

$$\nabla\phi_{ifg} = \nabla\phi_{def} + \nabla\left(\Delta\phi_{\epsilon}\right) + \nabla\phi_{atm} + \nabla\left(\Delta\phi_{orb}\right) + n \tag{4.2}$$

The model assumes that the phase gradients of the atmospheric phase screen ($\nabla\phi_{atm}$) and the orbit errors ($\nabla(\Delta\phi_{orb})$) for nearby pixels are negligible compared to the other phase components. Hence, the phase gradient term can be approximated by a temporal deformation model and a linear DEM error term. It is to be noted that the temporal model regards the spatial gradient as a function of time and not the actual deformation itself. This model is applied to all the pixel pairs that are separated by a pre-determined finite distance. The reliability of the model for a corresponding phase can then be quantified by a numerical measure called *temporal coherence* defined as

$$\rho_{temp} = \| \sum_{k=1}^{N_{ifg}} e^{\left[\phi_{ifg,k} - \phi_{model,k}\right]} \| \tag{4.3}$$

where is $\phi_{ifg,k}$ represents the observed double-difference phase in interferogram k and $\phi_{model,k}$ represents the modeled phase for the same pair of pixels in interferogram k. The temporal coherence value ranges from zero to one and represents the quality of fit of the model to the observed data. Amongst the initial set of PS candidate pairs, many exhibit large residuals or a low temporal coherence. Pixels that figure in a large number of such low coherence pairs are flagged as noisy and not included in the final PS network. Thus, a deformation model incorporating any *a priori* information about the area being analyzed itself can also be used for identifying a PS network.

4.3 StaMPS PS selection

The StaMPS framework, as developed by Hooper (2006) is described in detail in Section 3.4. The StaMPS method is a complete package of PS-InSAR analysis tools and incorporates vital aspects of many other PS selection algorithms. StaMPS was the first method to adopt phase stability and spatial correlation as a criterion for PS selection.

Equation 3.15 defines the pixel-wise coherence, a phase stability measure ranging between zero and one corresponding to a purely random phased pixel and an ideal

point scatterer respectively. Similar coherence measures are also computed for a few hundered thousand randomly simulated phase sequences. Due to the finite number of phase observations, i.e, the number of interferograms, the observed estimates are biased (Touzi *et al.*, 1990). As a result, it is assumed that all the coherence estimates with values less than 0.3 corresponds to noisy non-PS pixels. This assumption is used to normalize the histograms of the observed coherence values and the simulated random phase coherence values. Thus the probability of each pixel belonging to the family of PS pixels, based solely on the coherence measure, can be determined as shown below (Hooper, 2006).

$$P\left(x \in \mathrm{PS} | \, \rho\right) = 1 - \left[\frac{\int_0^{0.3} P_{obs}\left(\rho\right) \cdot d\rho}{\int_0^{0.3} P_{sim}\left(\rho\right) \cdot d\rho}\right] \cdot \frac{P_{sim}\left(\rho\right)}{P_{obs}\left(\rho\right)} \tag{4.4}$$

P_{sim} and P_{obs} correspond to the simulated coherence histogram and the observed coherence histogram respectively. Based on these probability measures, we can define a random pixel acceptance rate (RPAR) corresponding to the coherence threshold (ρ_{thr}) as

$$\mathrm{RPAR}\left(\rho_{thr}\right) = \left[\frac{\int_0^{0.3} P_{obs}\left(\rho\right) \cdot d\rho}{\int_0^{0.3} P_{sim}\left(\rho\right) \cdot d\rho}\right] \cdot \left[\frac{\int_{\rho_{thr}}^{1} P_{obs}\left(\rho\right) \cdot d\rho}{\int_{\rho_{thr}}^{1} P_{sim}\left(\rho\right) \cdot d\rho}\right] \tag{4.5}$$

The RPAR values can be numerically calculated using the observed coherence values and an appropriate threshold for PS selection can be chosen depending on a suitable choice of RPAR. Hooper (2006) also observed that the selection process can be improved by incorporating the amplitude information. All pixels with coherence values greater than the estimated threshold (ρ_{thr}) are labelled as PS pixels.

The StaMPS PS selection technique outperforms the other PS algorithms described in the previous sections and successfully identifies more PS pixels in non-urban vegetated terrain. We build on the StaMPS framework laid out by Hooper (2006) and define our own PS selection algorithm. The details of our selection algorithm are presented in the next section.

4.4 Maximum Likelihood PS selection

Once all the spatially correlated terms are estimated as described in Equation 3.4, we are left with only the noise term, ϕ_n, representing the combined phase contribution from the scatterers in the resolution cell. We compare the observed phases with the theoretical phase distributions (Equations 3.10 and 3.12) to obtain the maximum likelihood estimate of SCR (γ).

From Equation 3.10 and Equation 3.12, we have a forward model for the distribution of interferometric phase as a function of γ, $P(\phi_n|\gamma)$. Using Bayesian concepts, we estimate the value of γ maximizing the $P(\gamma|\phi_{n_1}, \cdots, \phi_{n_N})$, where $\phi_{n_1}, \cdots, \phi_{n_N}$ are the residual noise phase terms at a pixel in N interferograms, γ is the SCR of the brightest scatterer in the resolution element, and $P(A|B)$ is the probability of event A given event B. In other words, we determine the most likely γ that produced the observed distribution of residual noise phase terms. Using Bayes' rule we rewrite the probability function as follows:

$$P(\gamma|\phi_{n_1}, \cdots, \phi_{n_N}) = \frac{P(\phi_{n_1}, \cdots, \phi_{n_N}|\gamma) \cdot P(\gamma)}{P(\phi_{n_1}, \cdots, \phi_{n_N})} \tag{4.6}$$

The term in the denominator of the right hand side of Equation 4.6 is independent of γ, thus we need only to maximize the numerator over all values of γ. As we have no prior knowledge of γ, we assume that all values are equally likely, that is, $P(\gamma)$ is constant for all values of γ. We also assume that the observed interferometric phase values are independent and identically distributed.

Under these conditions it suffices to maximize the product $P(\phi_{n_1}) \cdots P(\phi_{n_N})$ over all possible values of γ. In other words, we can restate Equation 4.6 as maximizing the product

$$\begin{aligned} \gamma_{ML} &= \arg\max_{\gamma} \left[P(\phi_{n_1}) \cdots P(\phi_{n_N})\right], \qquad \forall\gamma \\ &= \arg\max_{\gamma} \left[\sum_{k=1}^{N} \log\left[P(\phi_{n_k})\right]\right], \qquad \forall\gamma \end{aligned} \tag{4.7}$$

This estimator reduces to evaluation of the sum of probability terms that can be precomputed for different values of γ and ϕ using the expressions given in Equation 3.10 or Equation 3.12. We do not see a significant difference in the results obtained using the two different signal models described in Chapter 3 and hence, assume the Gaussian signal model (Section 3.3.2) in all further discussions due to its closed form PDF expression (Equation 3.12).

We compare the maximum likelihood estimate γ_{ML} from Equation 4.7 for each of the candidate pixels against a pre-determined threshold value (γ_{thr}) - those that exceed the threshold form the set of candidate PS pixels. The successful implementation of our PS selection algorithm depends on the properties of our estimator (Equation 4.7) and the choice of the threshold (γ_{thr}). We elaborate on each of these aspects in the next few subsections.

4.4.1 Estimator properties

In this section, we describe some of the salient features of the MLPS estimator (Equation 4.7) and show that it outperforms the conventional temporal coherence estimator described in Equation 4.3. Replacing the temporal coherence estimator with the MLPS estimator in the StaMPS framework leads to a significantly larger number of PS pixels being correctly identified.

1. **Random phase sequences**

   Figure 4.3 compares the ability of the temporal coherence estimator (Equation 3.15) and the MLPS estimator (Equation 4.7) to identify pixels with random interferometric phase observations. The MLPS estimator has a lower bias compared to the conventional coherence estimator. The estimates were computed for a million randomly simulated phase sequences of length 40. The tail of the histogram corresponding to the MLPS results (dotted lines) also drops to zero faster than the conventional coherence results (solid line). Consequently, the MLPS estimator identifies a larger percentage of random pixels as non-PS pixels than the temporal coherence estimator.

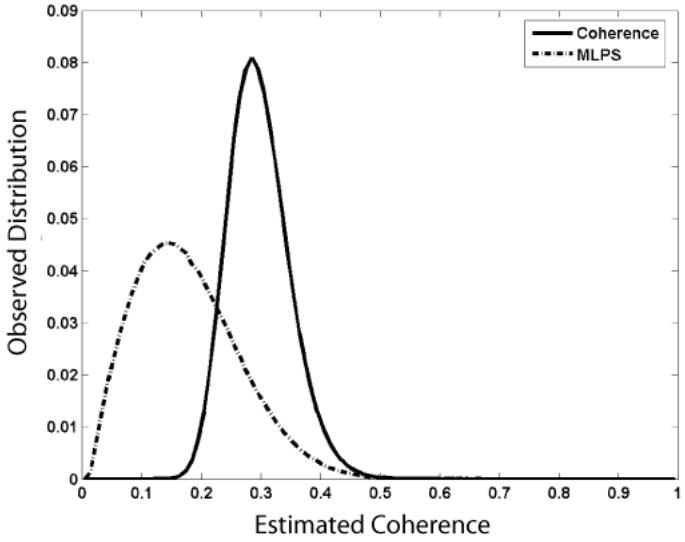

Figure 4.3: Comparison of the ability of the conventional coherence estimator and the MLPS estimator to identify pixels with random interferometric phase. The MLPS estimator has a lower bias and drops to zero faster than the temporal coherence estimator. The MLPS estimator successfully identifies a larger percentage of random phased pixels as non-PS pixels than the temporal coherence estimator.

2. **Effect of sample size**

   The MLPS estimator exhibits expected behavior when the number of input samples for the estimator are changed (Figure 4.4). The bias in the estimates increases as the number of available phase observations decreases. The variance in the estimates also increases for fewer number of observations. From Figure 4.4, it is clear that the MLPS estimator outperforms the conventional coherence estimator even for smaller sample sizes.

3. **Accuracy of the estimator**

   We define the accuracy of the MLPS estimator as it's ability to identify the true SCR used to simulate a sequence of phase observation according to the gaussian signal model. Figure 4.5 shows the estimated SCR (γ_{ML}) as a function of true SCR. We simulated 100000 InSAR time-series corresponding to 25 interferograms for each SCR value (spacing of 0.05) for the Gaussian signal

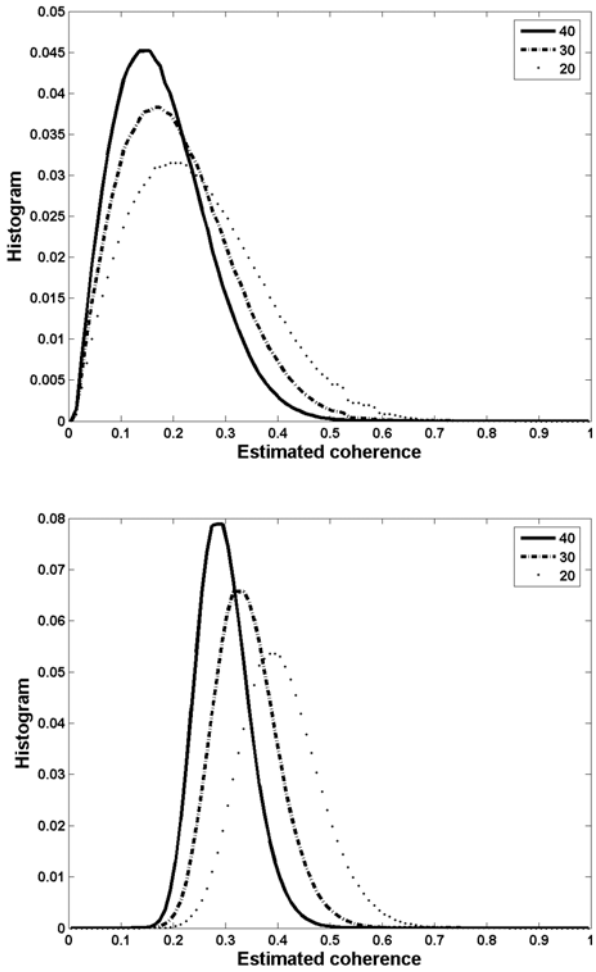

Figure 4.4: The effect of sample size on the ability of the MLPS estimator to identify random noisy pixels. The histograms of estimated correlations for simulated random phase sequences of various lengths - (Top) MLPS estimator and (Bottom) Conventional coherence estimator. The experiment used to compute Figure 4.4 was repreated for 20 (dots), 30 (dots and dashes) and 40 (solid lines) interferograms. The bias in estimated coherence decreases with increased sample size for both the estimators.

model and used the estimator given in Equation 4.7 to generate the image. The MLPS estimator (Equation 4.7) slightly underestimates the true SCR value but the slope of the line is very close to one to ignore this disparity. We notice that the estimated SCR never reaches zero due to the bias from the finite sample size.

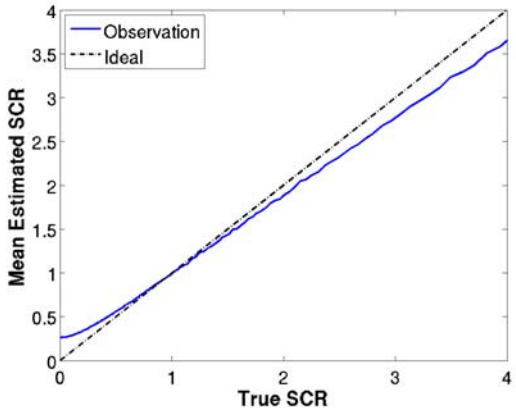

Figure 4.5: Estimates Most Likely SCR (γ_{ML}) using Equation 4.7 as a function of true SCR value for 100000 simulate pixels, assuming a time-series consisting of 25 interferograms and the Gaussian signal model. The theoretical unitary slope line corresponding to an ideal estimator is also shown.

4.4.2 Threshold Selection

The set of candidate PS pixels depends on our selection of the proper γ_{thr}. If the threshold is too high, many potential PS pixels are not included and the resulting PS network is sparse. If the threshold is set too low, too many non-PS pixels are included and the network contains many points that are not truly persistent. Our threshold selection is currently rather arbitrary, because we cannot easily calculate the scattering statistics for persistent pixels amid all possible background terrains. If we could set a limit on the natural variation in the phase of each pixel, we could readily select the threshold parameter γ_{thr} from the dependence of phase standard deviation on γ (Figure 4.6). If we believe, for example, that we should see a natural variation of a fifth of a cycle across all interferograms, then the threshold value is about 2.

Alternatively, we could use one of the common radar detection criteria like constant error rate (e.g. see Skolnik (2001)) to set our threshold. The error rate

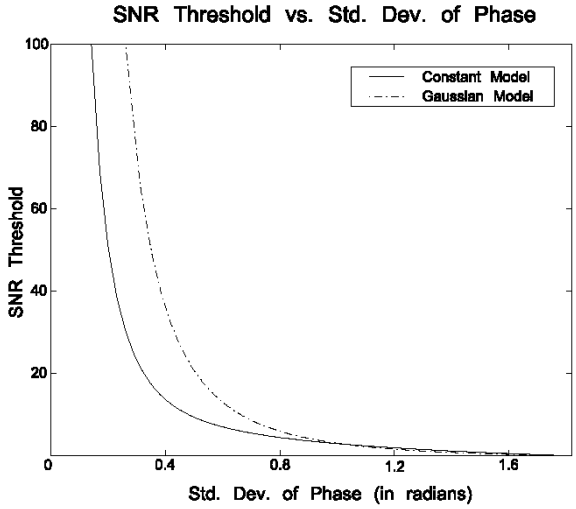

Figure 4.6: Standard deviation of interferometric phase for the constant signal model and the gaussian signal model. We can estimate the threshold (γ_{thr}) by setting a limit on the natural phase variation.

(ER) for a given threshold (γ_0) can be numerically estimated using the equation

$$\begin{aligned} \mathrm{ER}\left(\gamma_0\right) &= \int_0^{\gamma_0} f\left(\beta\right) \cdot P\left(\gamma_{est} > \gamma_0 | \gamma = \beta\right) \cdot d\beta + \\ & \int_{\gamma_0}^{\inf} f\left(\beta\right) \cdot P\left(\gamma_{est} < \gamma_0 | \gamma = \beta\right) \cdot d\beta \end{aligned} \tag{4.8}$$

The first term in both the integrals ($f\left(\beta\right)$) is the PDF of the SCR of the scatterers in the scene that can be estimated from the data itself using the Equation 4.7. We estimate the second term in both the integrals in the right hand side of Equation 4.8 by simulating sequences of interferometric phase residuals from the theoretical PDFs (Equation 3.10 or Equation 3.12) using the MLPS estimator in Equation 4.7. For an error rate of 5%, we can then estimate our threshold using

$$\gamma_{thr} = \arg\min_{\gamma} \mathrm{ER}\left(\gamma\right), \qquad \forall\, \gamma \quad \text{s.t. } \mathrm{ER}\left(\gamma\right) < 0.05 \tag{4.9}$$

ER is often a misleading metric in practical applications, because the penalty of non-selection of true PS pixels is less compared to the penalty of selection of non-PS pixels. More importantly, selecing fewer non-PS pixels with random phase characteristics

significantly improves our ability to reliably unwrap the phase data and decrease noise in our deformation estimates. Hence, a more appropriate metric would be the random pixel acceptance rate (RPAR) defined by the rate of acceptance of pixels with truly random or uniform phase distribution. Figure 4.7 shows the estimated RPAR for both the signal models as a function of the SCR threshold (γ_{thr}) obtained by simulating 100,000 sequences of random phase values in the interval $[-\pi, \pi)$ and estimating the corresponding γ_{ML} using Equation 4.7. For a RPAR of 1%, we could estimate the SCR threshold using the following equations.

$$\text{RPAR}(\gamma_0) = P(\gamma_{est} > \gamma_0 | \gamma = 0) \tag{4.10}$$

$$\gamma_{thr} = \arg\min_{\gamma} [\text{RPAR}(\gamma)] \qquad \forall \gamma \; s.t \, \text{RPAR}(\gamma) < 0.01 \tag{4.11}$$

From Figure 4.7, we observe that for a SCR threshold of 1.8, the RPAR for both the

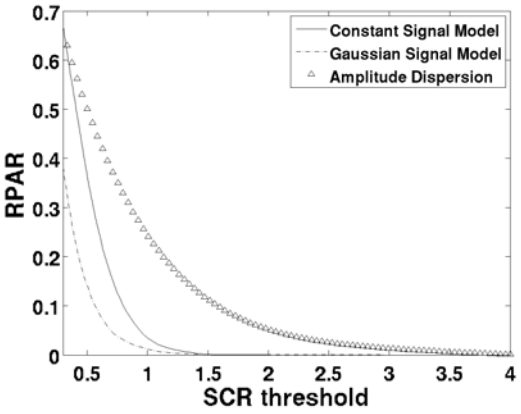

Figure 4.7: RPAR values for various SCR thresholds(γ_{thr}) for the constant and gaussian signal models, and amplitude dispersion method. At SCR value of 2, the random pixel selection rate is less than 1% for the constant and gaussian signal models. RPAR for the amplitude dispersion method does not reduce to 1% till an SCR threshold of about 3.2.

signal models is less than 1%.

An SCR threshold value of 2 fulfilled all the three PS selection criterion described in this section, for the data sets that we examined. Similar threshold values for SCR

have been used in other PS algorithms as well (Adam *et al.*, 2003; Kampes and Adam, 2005).

4.5 An example application

We applied our PS pixel selection method to ERS data acquired over the San Francisco bay area in two different regions: along the San Andreas fault near the SFO airport region and along the Hayward fault near the Oakland-Alameda area. These areas consist of a combination of urban and natural terrain clearly traversed by active faults. Conventional InSAR studies combined with GPS observations (Bürgmann *et al.*, 2000) measure the fault creep deformation signal well in the urban regions along the Hayward Fault, with inconclusive measurements along the San Andreas fault. Previous PS studies (Bürgmann *et al.*, 2006) conducted in this area also pick out coherent scatterers in the urban areas well, but fail in identifying a reliable network of scatterers in the natural terrain on the more rural sides of the faults.

We processed 19 descending scenes acquired by ERS-1 and ERS-2 between 1992 and 2000. We selected a scene from September 1995 as a master scene, based on minimization of the perpendicular baseline and the temporal baseline, and generated 18 interferograms. The maximum perpendicular baseline was 260 m. Using the maximum likelihood selection method, we can identify coherent pixels on the non-urbanized sides of each fault, including where the Ferretti and StaMPS methods fail to locate any PS pixels (See Figure 4.8). Figure 4.9 shows the observed average deformation rates in mm per year and the locations of PS pixels for the San Andreas Fault and Hayward Fault region. Creep of 3 mm/yr (LOS) shows clearly along the Hayward fault, but no evidence of creep greater than possibly 1-2 mm/yr appears along this segment of the San Andreas fault. Notably, in both these regions our methods identified PS in regions where other methods have failed to identify any coherent scatterers. Once we identify the proper set of PS pixels, we obtain a deformation time-series by unwrapping the measured phases in three dimensions, two

spatial dimensions and one in time. We used the step wise-3D unwrapping method described by Hooper and Zebker (2007).

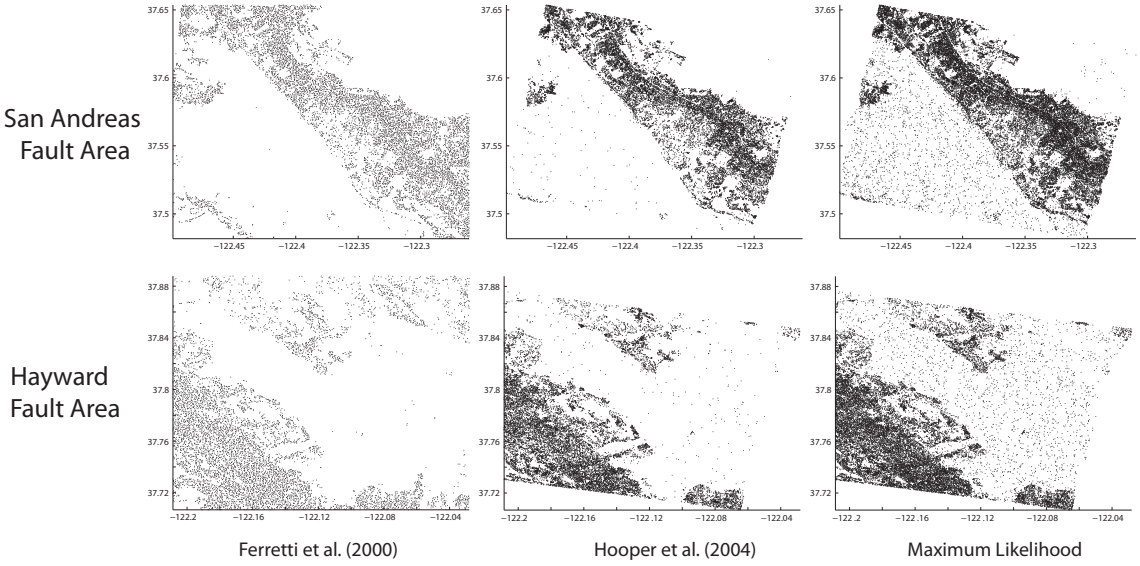

Figure 4.8: Binary mask of the identified PS for the SFO airport region (top) and Oakland-Alameda region (bottom). Results from (left) Ferretti, (middle) Hooper and (right) maximum likelihood methods. The MLPS approach identifies a denser PS network in natural terrain than either of the published methods.

Examination of the PS pixels outside of the urban areas in both regions of study shows that there are areas with spatially correlated phases distinct from the average background velocities. While these could be areas of coherent motion such as landslides, subsidence, or other localized movement, they can just as easily be the product of phase unwrapping errors. At present we are unable to validate the absolute accuracy of the phase unwrapping and this appears to be the limiting problem in the application of PS methods to natural terrains. In Chapter 7, we provide a detailed analysis of the time-series of many of the features observed in Figure 4.9.

4.6 Conclusions

The new maximum likelihood methods for the identification of candidate PS pixels finds many more PS points than published algorithms. When applied to ERS-1

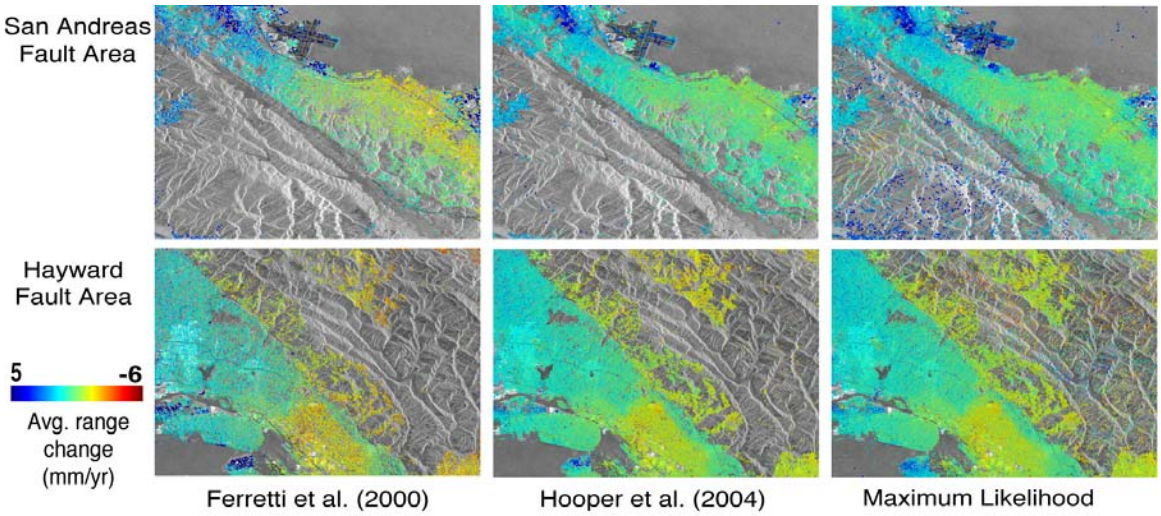

Figure 4.9: Comparison of PS identification algorithms for the SFO airport region (top) and Oakland-Alameda region (bottom). Results from (left) Ferretti, (middle) Hooper and (right) maximum likelihood methods. The MLPS approach identifies a denser PS network in natural terrain than either of the published methods.

Table 4.1: Comparison between different PS selection methods for two test regions in the San Francisco Bay Area

	SFO airport region		Oakland-Alameda region	
	Permanent Scatterers ® (6800)		Permanent Scatterers ® (13237)	
	StaMPS	MLPS	StaMPS	MLPS
PS Candidates	325554	325554	485983	485983
Pre-weeding	31395	50883 (62%)[a]	80469	108939 (35%)[a]
Selected PS	20012	32683 (63%)[a]	46181	62733 (35%)[a]
Common with StaMPS	All	19568 (98%)	All	45034 (98%)

[a] indicates an increase.

and ERS-2 data acquired over the San Francisco bay area, our PS selection method identified 62% (San Andreas Fault region) and 35% (Hayward Fault region) more persistent pixels than Hooper's (2004) algorithm, which in turn finds more PS pixels than Ferretti's original (2001) method. We find 97% of the pixels identified by Hooper plus many more, notably in the vegetated areas in which both previous methods fail to find sufficient persistent scatterers to form a usable network to infer deformation.

Thus the major advantage of the new method is that it allows us to find persistent scattering pixels in vegetated and non-urban terrain, as shown here in the hills west of the San Andreas fault near the SFO airport and the hills to the east of Hayward fault. Very few coherent scatterers are identified here using the methods of Ferretti *et al.* (2001) and Hooper *et al.* (2004), greatly limiting our ability to measure deformation accurately. The PS pixels identified by the maximum likelihood method are mostly a superset of those identified by published methods. Significant work remains in the development of useful 3-dimensional phase unwrapping algorithms. Phase unwrapping error is still the major source of uncertainty for PS-InSAR in vegetated areas. The increased density of PS points provided by the maximum likelihood selection method promises to make the unwrapping problem more tractable. We have addressed the phase unwrapping problem in Chapter 5 with the development of two new unwrapping algorithms suitable for PS-InSAR applications.

Chapter 5

Phase Unwrapping

In chapter 4, we described a new technique for identifying a dense network of persistently scattering pixels. The key processing step in extracting the surface deformation is the estimation of the unwrapped phase for this network of PS pixels. In this chapter, we discuss the spatially sparse data problem, the three dimensional phase unwrapping problem, and a new integer programming formulation for phase unwrapping of multi-dimensional data.

Phase unwrapping is a key problem in many coherent imaging systems, including time series synthetic aperture radar interferometry, which has two spatial and one temporal data dimensions. The problem poses a harder challenge when the data is spatially sparse, due to the availabilty of few reliable PS pixels over the area of interest. We first present a simple method to reduce sparse data sets to equivalent regularly sampled data sets for two-dimensional data. We then describe the edgelist phase unwrapping algorithm which builds on the concepts of the minimum cost flow (MCF) formulation of Costantini (1998). The MCF phase unwrapping algorithm describes a global cost minimization problem involving flow between phase residues computed over closed loops. In our approach, we replace closed loops by reliable edges as the basic construct, thus leading to the name "edgelist". Our algorithm has several advantages over current methods:

- It simplifies the representation of multi-dimensional phase unwrapping.

- It can incorporate data from external sources, like GPS, where available to better constrain the unwrapped solution.
- It treats regularly sampled or sparsely sampled data alike.

It is thus particularly applicable to time series InSAR where data are often irregularly spaced in time, and individual interferograms are corrupted with large decorrelated regions. We show that, similar to the MCF network problem, our formulation also exhibits total unimodularity (TUM) which enables us to solve the integer program using efficient linear programming tools. We then apply our method to a PS-InSAR dataset from the creeping section of the Central San Andreas Fault.

5.1 Introduction

Phase unwrapping as used in InSAR geodesy is the reconstruction of absolute phase from measured phase known only modulo 2π on a finite grid of points. Many methods have been developed for unwrapping SAR interferograms (Hunt, 1979; Goldstein *et al.*, 1988; Ching *et al.*, 1992; Ghiglia and Romero, 1996; Pritt, 1996; Flynn, 1997; Zebker and Lu, 1998; Costantini, 1998; Chen and Zebker, 2000), however phase unwrapping is a key step in many other coherent imaging techniques as well. Most of these methods primarily focus on regularly sampled two dimensional data sets. Interferograms, especially in time series analysis, are often irregularly sampled in both space and time, so that existing algorithms do not always properly unwrap the data. In this chapter, we develop a method to address the most general form of the phase unwrapping problem - unwrapping sparsely distributed, multi-dimensional wrapped phase data. Since we focus on applying our new technique to InSAR phase data, we restrict our discussion to conventional two dimensional (single interferogram) InSAR data and multi-temporal InSAR (Persistent Scatterer and Short Baseline methods) three dimensional data sets.

The performance of any phase unwrapping algorithm depends on our ability to estimate the phase gradient between two adjacent samples in our data set. The

basic assumption in all phase unwrapping problems is that the underlying continuous unwrapped phase function is well sampled in every dimension to enable us to reconstruct it from wrapped phase measurements except at a finite, relatively small, number of discontinuities.

The existence of discontinuities in a data set produces path dependent inconsistencies or residues (Goldstein *et al.*, 1988). The branch cut algorithm (Goldstein *et al.*, 1988) and its derivatives are very popular approaches to phase unwrapping, due to their ease of implementation. Hooper and Zebker (2007) successfully extended the idea of the shortest branch cut to the 3D phase unwrapping problem. Least squares (Hunt, 1979) and FFT-based (Ghiglia and Romero, 1994) phase unwrapping algorithms are computationally efficient but tend to distribute unwrapping errors globally instead of restricting errors to a small set of points. Ghiglia and Romero (1996) suggested a general L_p norm objective function for phase unwrapping problems and argued that L_0 and L_1 norm solutions would produce fewer errors than the traditional least squares solution.

Costantini (1998) developed the first network programming formulation to solve the regularly sampled two dimensional (2D) phase unwrapping problem using an L_1 norm minimum cost flow (MCF) approach. Costantini and Rosen (1999) adapted the algorithm to solve the irregularly sampled 2D phase unwrapping problems using Delaunay triangulation (Barber and Huhdanpaa, 2009). The performance of the network-programming-based unwrapping algorithms for 2D data sets was further improved by the development of an iterative L_0 norm approximation algorithm (Chen and Zebker, 2000) and its application in combination with statistical cost functions (Chen and Zebker, 2001).

We propose a new minimum L_1 norm formulation that is more flexible than the original MCF formulation, allowing us to impose additional constraints on the unwrapped solutions based on available a priori information. It also can be easily extended to analyze multi-dimensional data sets. Here, we briefly review conventional residue-based phase unwrapping algorithms (Section 5.2). We then describe our

new algorithm in Section 5.5. In Section 5.6, we discuss the ability to incorporate additional geodetic observations as constraints in our new algorithm. We apply the method to a time series of data acquired over the creeping section of the San Andreas Fault in Section 5.7. Finally, we discuss implementation and suggest possible improvements.

5.2 Residue-based unwrapping techniques

The primary force motivating the development of residue-based phase unwrapping algorithms is the notion that all the phase discontinuities in a two-dimensional data set are due to linear discontinuities. Goldstein *et al.* (1988) observed that the endpoints of these linear discontinuities can be identified using a discretized curl measure, also known as a residue, as the total phase gradient around the end points does not add up to zero. Example of such closed loops with zero, $+1$ and -1 are shown in Figure 5.1. The residues are assumed to be located at the centroids of the corresponding loops.

In the original residue-cut algorithm (Goldstein *et al.*, 1988), a non-zero residue is located and connected to the nearest non-zero residue, irrespective of the sign. The process of locating and adding non-zero residues to this tree continues until the tree is neutralized. Once neutralized the whole process is repeated again starting from another non-zero residue. When all the residues have been neutralized, the wrapped phase is integrated along any path like a one-dimensional problem (flood-fill algorithm) without integrating over the branch cuts or linear discontinuities. The main aim of the algorithm was to reduce the total length of linear discontinuities imposed to unwrap the data set.

Chen and Zebker (2000) showed that the shortest branch-cut problem reduces to the minimum Steiner tree problem and is *NP*-hard. They observed that the minimum spanning tree (MST), which is the shortest path connecting all the residues, is a good approximation of the minimum steiner tree and overcomes the problem of disconnected regions produced by the original branch-cut algorithm. These

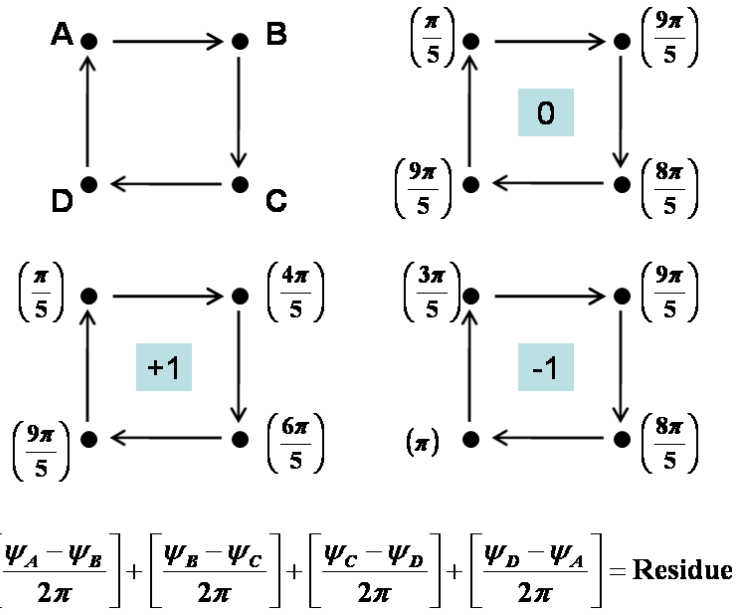

Figure 5.1: Determination of phase residues in a regularly sampled two-dimensional interferogram. $[\cdot]$ represents the nearest integer function. Loops with non-zero residues represent the end-points of linear discontinuities marking phase cycle jumps.

branch-cut algorithms perform well in regions of high coherence, but fail to perform satisfactorily in noisy decorrelated sections of inteferograms (Chen and Zebker, 2000). These algorithms inherently cannot accomodate quality measures and external information in placing these branch cuts to produce more reliable solutions.

5.2.1 Network programming approach

Costantini (1998) exploited the equivalence between the constrained minimum spanning tree problem and the minimum cost flow (MCF) problem to reformulate the problem as a network programming problem. The MCF formulation allows for quality measures in form of cost functions to automatically direct the placement of branch cuts.

The MCF formulation explicitly allows us to solve for the integer phase cycles (K_{ij}) that need to be added to the each edge (i, j) of the unwrapping grid to produce a consistently unwrapped solution. If we introduce non-zero cost functions (C_{ij})

associated with adding a unit phase cycle over each edge (i, j), the two-dimensional phase unwrapping problem can be formulated as a minimum cost flow problem as follows (Costantini, 1998):

$$\begin{aligned}
&\text{Minimize} && \sum_{\forall (i,j) \in E} C_{ij} \cdot ||K_{ij}|| \\
&\text{Subject to} && \\
K_{AB} + K_{BC} + K_{CD} + K_{DA} &= && \left[\frac{\psi_A - \psi_B}{2\pi}\right] + \left[\frac{\psi_B - \psi_C}{2\pi}\right] + \\
& && \left[\frac{\psi_C - \psi_D}{2\pi}\right] + \left[\frac{\psi_D - \psi_A}{2\pi}\right] \\
& && \forall \text{ simple closed rectangles } (A, B, C, D) \\
K_{ij} \text{ is an integer} & && \forall (i, j) \in E
\end{aligned} \tag{5.1}$$

where the right hand side of the constraint equation corresponds to the residue enclosed by each loop (Figure 5.1), $|| \cdot ||$ refers to the L_1 norm and E represents the set of all edges belonging to a simple rectangular grid. The additional integer cycles K_{ij} that need to be added is also referred to as the integer flow on the edge (i, j). The cost functions C_{ij} are used to direct the placement of phase cycle jumps using quality measures derived from the data itself.

5.3 Reduction of sparse data on a regular grid

New multiple pass InSAR techniques often produce a sparse set of points that represent the only reliable measurements of line of sight (LOS) displacement (Chapter 4). PS points are often widely spaced and irregularly sample the deformation pattern. Many current phase unwrapping methods such as SNAPHU (Chen and Zebker, 2001) are not designed to use arbitrarily spaced data, and thus their major benefits of constraining possible and optimal solutions cannot be realized. In this section, we describe a resampling method that enables us to use popular and freely available regular grid 2D phase unwrapping software to unwrap sparse data sets

effectively. Numerous approaches to phase unwrapping on a regular grid have been suggested in the recent past. These unwrapping approaches rely on the concept of residues (Goldstein *et al.*, 1988) about closed loops, using estimates of integrated phase gradients to identify areas of inconsistency. Network programming approaches (Chen and Zebker, 2000; Costantini, 1998; Chen and Zebker, 2001) have so far proven to be the most effective of these. These methods have also been extended to unwrap sparse 2D data sets (Costantini and Rosen, 1999).

For reducing the sparse data to a regular grid, we adopt the concept of residues defined by closed loops of triangles from a non-overlapping triangulation of the given set of sparse data points. The data are then resampled to a regular Cartesian grid and unwrapped with existing solvers. All the results shown here were produced using the Statistical-cost Network flow Algorithm for Phase Unwrapping (SNAPHU) software (Chen and Zebker, 2001). However, any unwrapping algorithm may be used once the sparse 2D unwrapping problem is transformed to a regularly-spaced grid unwrapping problem with our method. This approach for reducing sparse unwrapping problem to a regular grid unwrapping problem was also developed independently by Hooper (Hooper, 2009), who implemented it in the StaMPS software package for PS processing.

5.3.1 Definitions

Let S represent a set of distinct points on a 2D plane where the wrapped phase values are known. Often, these are a subset of points on a regular rectangular 2D grid as represented in Figure 5.2 by distinct symbols enclosed in circles. We now define two real functions $\psi(s)$ and $\phi(s)$ for each point , such that

$$\psi\left(s\right) = \phi\left(s\right) + 2\pi n\left(s\right) \tag{5.2}$$

where $n(s)$ is an integer such that $\psi(s) \in [-\pi, \pi)$. The functions $\psi(s)$ and $\phi(s)$ are the wrapped and unwrapped phase functions respectively. Any useful unwrapping

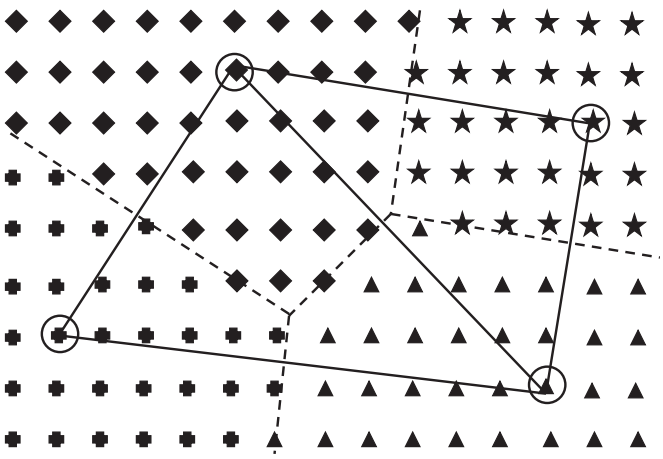

Figure 5.2: Reduction of a sample sparse data set to a regular 2D grid. Symbols enclosed in circles represent the original sparse data points. Solid lines and dashed lines represent the corresponding Delaunay triangulation and Voronoi diagram respectively. Other data points in the regular grid have been filled in with symbols using the nearest neighbor interpolation. Note that the Voronoi diagram corresponds to the boundaries of the interpolated regions.

approach estimates $n(s)$ from a given $\psi(s)$ such that the resultant unwrapped phase function $\phi(s)$ is irrotational, i.e curl of $\phi(s)$ reduces to zero. We also use two geometrical concepts called the Voronoi diagram and the Delaunay triangulation of the set of points S (Barber and Huhdanpaa, 2009). The Voronoi diagram $\left(\hat{S}\right)$ and the Delaunay triangulation $\left(\tilde{S}\right)$ are represented respectively by dashed and solid lines in Figure 5.2. The Voronoi diagram $\left(\hat{S}\right)$ is a continuous version of the regularly interpolated the grid. The Voronoi diagram and the Delaunay triangulation are closely related and it can be shown that in graph theory terminology, $\left(\tilde{S}\right)$ is the dual graph of $\left(\hat{S}\right)$ (Barber and Huhdanpaa, 2009). This property will be used below to relate the regular grid of nearest neighbor interpolated data to the Delaunay triangulation of the sparse data points.

The residues computed on $\tilde{S}$ of the set of vertices S are analogous to residues computed on a regular grid, in this case each triangle represents a non-overlapping closed loop. In existing sparse 2D unwrapping approaches (Costantini and Rosen, 1999; Hooper and Zebker, 2007), residues are computed on each of the triangles and

assumed to be located at the centroid (point of intersection of perpendicular bisectors of the edges) of triangles. In these methods, a branch cut algorithm or a maximum flow approach is then used to neutralize the residues, and the phases are derived from a filling algorithm that grows the phase field while avoiding inconsistent paths (see Goldstein *et al.* (1988) for a discussion).

5.3.2 Geometrical reduction to regular problem

We now show that we can reduce the sparse unwrapping problem to a regular 2D unwrapping problem using a nearest neighbor algorithm. We first interpolate the sparse phase data onto a regular grid using the smallest Euclidean distance nearest neighbor rule as described below. Co-circular vertices, or points that lie on the same circle, amongst the sparse data points can produce a non-unique Delaunay triangulation. We overcome this problem by perturbing or joggling the inputs S, by addition of small random numbers (Barber and Huhdanpaa, 2009). This ensures a unique triangulation $\left(\tilde{S}\right)$ and a convex Voronoi diagram $\left(\hat{S}\right)$. Efficient search algorithms (Mount and Arya, 2010) are then used to determine the nearest neighbor to a given arbitrary point from among a set of measured data points. An example is shown in Figure 5.2. We refer to all interpolated data points that were not part of the original sparse data set as replicas. These are represented by the symbols that are not enclosed in circles in Figure 5.2. Close inspection makes it clear that the boundaries of the nearest neighbor interpolated data approximates the Voronoi diagram, which is also shown by dotted lines.

Next, we show that the phase residues are conserved in the nearest neighbor interpolated regular 2D image. Figure 5.3 illustrates all the possible types of loops that we encounter in the interpolated regular grid. For simplicity, we only show the region within one of the Delaunay triangles and use distinct symbols to represent the three vertices of the triangle. From Figure 5.3, the following can be inferred:

1. Loops formed in regions consisting of the same phase values (Figure 5.3a) do not produce any residues.

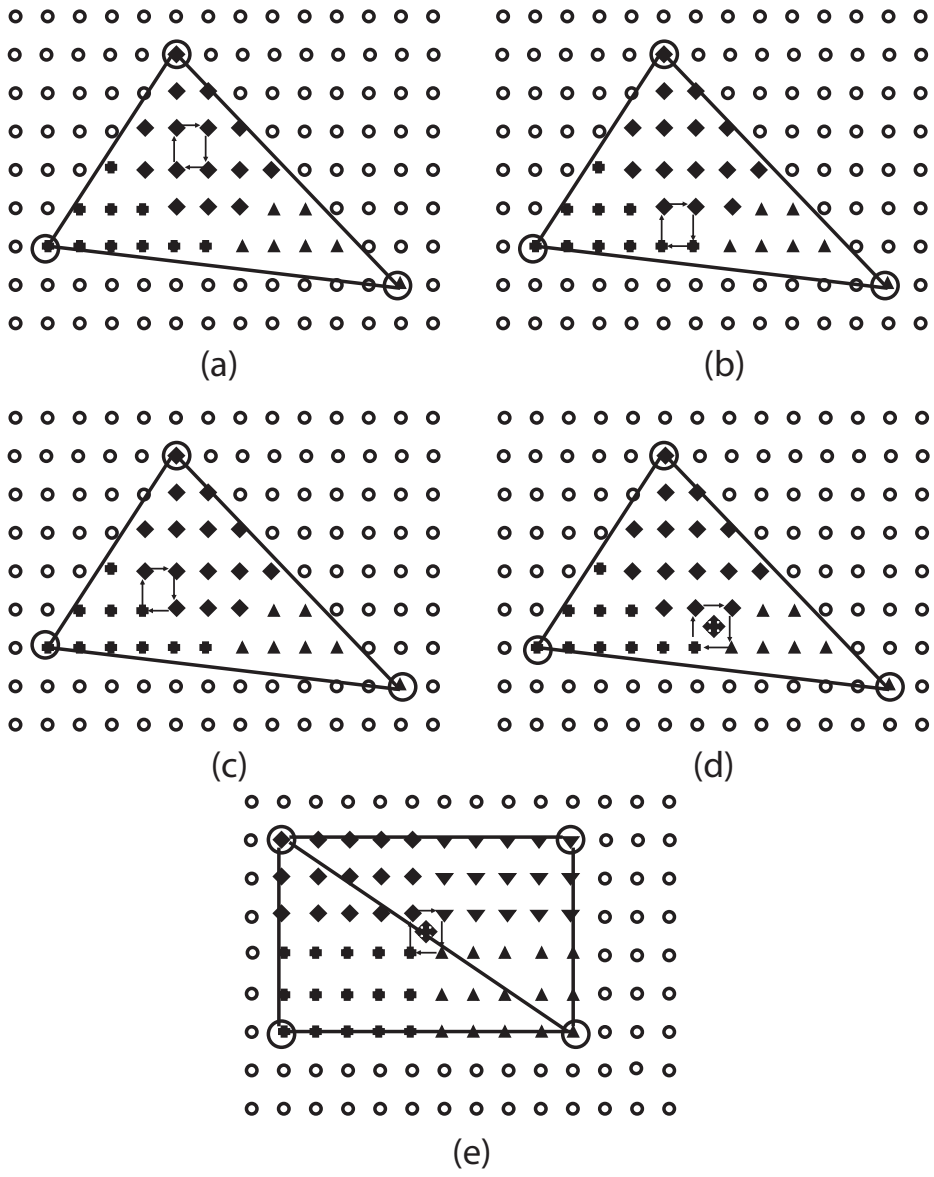

Figure 5.3: This figure shows all possible types of loops that can be observed in a regular 2D image obtained by nearest neighbor interpolation. Distinct symbols are used to identify replicas of different sparse data points. Only the loops in (d) and (e) can produce a non-zero residue.

2. Loops formed on the boundaries with two points of each kind (Figure 5.3b) do not produce residues, as we traverse the boundary twice but in opposite directions when going around the loop. The residue equation in Figure 5.1 evaluates to zero.

3. Loops formed on the boundaries with 3 points of one kind and one of another (Figure 5.3c) do not produce any residues. Again, we traverse the boundary in opposite directions and residue equation in Figure 5.1 evaluates to zero.

4. The loop containing the circumcenter, where at least one value corresponding to each vertex of the Delaunay triangle is present (Figure 5.3d) can produce a residue. The value of this residue is same as that of the original Delaunay triangle. Also, there can exist only one such loop within the triangular region as the circumcenter of each triangle is a unique point.

5. The residues of both the Delaunay triangles (Figure 5.3e) are co-located at the center of the square and the sum of the residues is same as that of the original square. Loops of this kind prevent an exact reduction of this sparse unwrapping problem to a regular unwrapping problem. Details are provided in the next section.

6. Hence, all the residues in the sparse image are conserved and are localized at the circumcenters of the Delaunay triangles.

We have thus shown that we can geometrically reduce the sparse unwrapping problem to a regular 2D problem, and that there is a unique mapping resulting from the nearest neighbor algorithm. Since the data is now defined on a regular grid, we can solve the problem using conventional unwrapping techniques. This is strictly true only if we ignore the cost functions for the edges formed during our original Delaunay triangulation. In the next section, we describe the equivalence of branch cuts in the original and the transformed problems. We also describe the changes required in the cost functions for an almost equivalent reduction of the sparse unwrapping problem to a regular 2D problem.

5.3.3 Branch cuts, flows and cost functions

If replicas of s_1 and s_2 are connected by at least an edge on the interpolated regular grid, they are connected in the Delaunay triangulation $(\tilde{S})$. This is a direct consequence of the duality relationship between $\hat{S}$ and $\tilde{S}$. Since we approximate the Voronoi diagram using a discrete regular grid, the inverse relationship is not true. Figure 5.3e shows an instance where the points on the diagonal (diamond and triangle) of the rectangle are connected in $\tilde{S}$ but not on the regular grid. Almost co-circular points often produce Voronoi boundary line segments that are completely enclosed within a unit square, leading to loss of the edges connecting the diagonals. In terms of geometry, this implies that the regular grid unwrapping problem corresponds directly to the sparse unwrapping problem defined using residues computed over a combination of triangles and quadrilaterals (except the lost edges, similar to merged facets in (Barber and Huhdanpaa, 2009)) rather than the original sparse unwrapping problem defined over $\tilde{S}$.

Also, since we preserve the geometry in terms of location of the residues at the circumcenters of the triangles, the branch cuts occupy the same physical location in the sparse and filled data sets. In other words, if the edge between s_1 and s_2 is marked by a branch cut in $\left(\tilde{S}\right)$, then all the edges between replicas of s_1 and s_2 will also be marked by the branch cut. An example is provided in Figure 5.4. If the edge between a diamond and a triangle (enclosed in circles) is crossed by a branch cut (dashed line) in the original sparse problem, all the edges between the diamonds and triangles are also crossed by the branch cut in the regular problem.

We arrive at the same conclusion using the arc network flow algorithms following similar reasoning. In the previous section, we proved that three of the five different types of loops cannot produce a residue. From property (1) in section 5.3.2, there cannot exist a non-zero flow or a cycle jump on an edge connecting the replicas of the same sparse point as this would imply that replicas of the same points are separated by a nonzero multiple of 2π, thus producing an inconsistency. Hence, any flow is restricted to edges connecting points with distinct phase values. From properties (2)

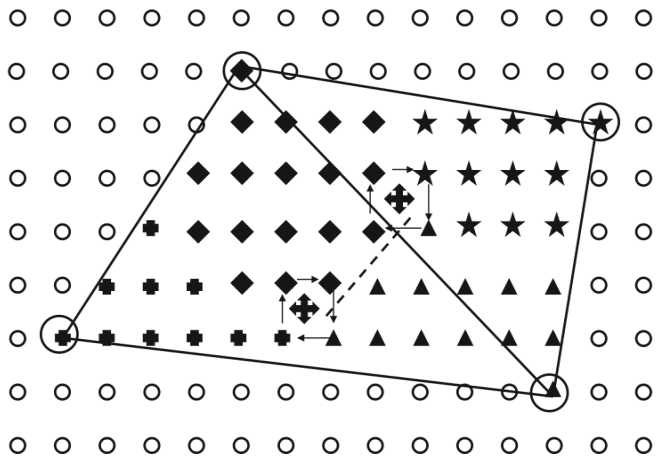

Figure 5.4: This example shows that a branch cut (dashed line) connecting the circumcenters of two adjacent Delaunay triangles intersecting the edges between vertices represented by a diamond and a triangle, also disconnects all edges on the regular grid that connect replicas of the diamond and the triangle.

and (3), we can infer that if there exists a flow on the arc connecting replica points of s_1 and s_2, all arcs connecting the replicas of s_1 to those of s_2 will carry the same flow. Thus, in either unwrapping approach, the cost function needs to account for the number of such edges between replicas of s_1 and s_2. We therefore define the cost functions to be used on the nearest neighbor interpolated data on the regular grid as

$$C_{reg}\left(s_1, s_2\right) = \frac{C_{sparse}\left(s_1, s_2\right)}{n\left(s_1, s_2\right)} \tag{5.3}$$

where $C_{reg}\left(s_1, s_2\right)$ is is the cost function for the edge joining a replica of s_1 and a replica of s_2, $C_{sparse}\left(s_1, s_2\right)$ is the cost function for the edge joining points s_1 and s_2 on the Delaunay triangulation and $n\left(s_1, s_2\right)$ is the number of edges between replicas of s1 and s2 on the regular grid. The edges connecting the replicas of the same sparse data point cannot sustain any flow because of reasons mentioned in section 5.3.2. In our work, the cost function of such edges is set to a large value.

The objective function of the regular unwrapping problem does not contain terms corresponding to the edges lost in the interpolation process. By comparing objective functions, we can again conclude that the regular unwrapping problem is equivalent to

a sparse unwrapping problem defined using residues computed over a combination of triangles and quadrilaterals, as described above. The number of lost edges is directly related to the distribution of points in S and typically constitutes a very small fraction (about one in a thousand) of all the edges in $\tilde{S}$. Often, if the data are well sampled, they do not carry any flow across them and do not contribute to the overall objective function. Hence, the regular unwrapping problem is almost equivalent to the sparse unwrapping problem defined over $\tilde{S}$.

5.3.4 Examples

We applied our method to two data sets, one simulated and one real. We first generated a synthetic interferogram of a vertical right-lateral strike slip fault and descending right-looking geometry over a regular grid using Okada's surface deformation model (Okada, 1985), and then randomly selected 10% of the points from the regular grid to form a sparse data set. Figure 5.5 shows the simulated sparse interferogram, including the fault trace in black and the result of unwrapping using L_1-norm weights in SNAPHU. No additional noise was added to the data and hence we used uniform weights on the original Delaunay triangles for unwrapping. For a test using actual data, we produced a second interferogram from data of the 2003 Bam earthquake in Iran as measured using the SAR instrument on the Envisat satellite (Funning *et al.*, 2005). We randomly selected 10% of the points in this case to simulate a sparse interferogram. Figure 5.6 shows the interferogram and its corresponding unwrapped solution obtained with SNAPHU, in a manner that makes it easy to compare the images directly with Figure 4 (b,d) from Funning *et al.* (2005). The solution of our synthetic data set precisely matches the original data in the simulated interferogram. The sparse-data Bam solution is geophysically plausible but underestimates the total deformation reported by Funning *et al.* (2005). This is a direct consequence of the sparseness of reliable measurements and the resulting loss of residues or cycle jumps in regions of large deformation gradients. The accuracy of our method and the ability to handle varying degrees of data sparseness depends

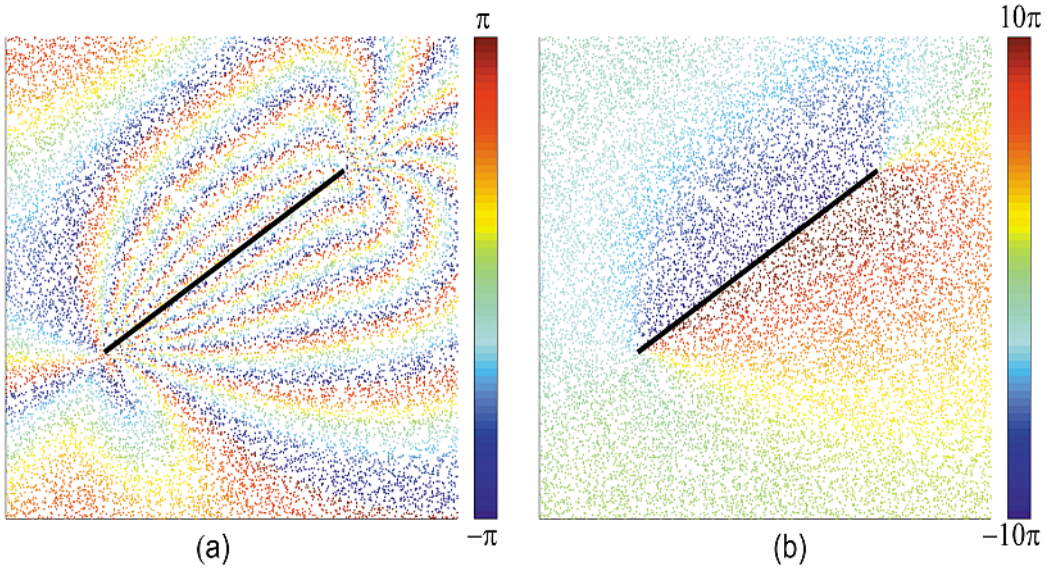

Figure 5.5: (a) Simulated interferogram of a right lateral strike slip fault with 10% of the randomly selected points from the complete interferogram. (b) The unwrapped interferogram using SNAPHU and L_1 norm weights. All the white regions in the image indicate areas where no data is available.

on how the solver retrieves the missing phase cycles using the residues computed on the Delaunay triangulation. Hence if too few data points are available, the solution will be poor. The resampled-data problem can often be solved very quickly because most of the potential residues on the regular grid are likely to be zero due to reasons described in section 5.3.2. We have shown here that the solver in SNAPHU works well for the two cases we have used, but any solver could be combined with a nearest neighbor interpolator to unwrap sparse data.

Our method can also be used with existing regular grid 3D unwrapping software, if available, to unwrap such data sets. In addition, our method does not need expensive commercial solvers or complicated pre-processors and can be easily implemented with existing regular grid solvers. Note that we do not claim that our method necessarily outperforms other unwrapping methods, it simply makes the sparse unwrapping problem feasible using many existing codes. The result of our transformation, applied to sparse data, is almost the same as the solution obtained using residues computed

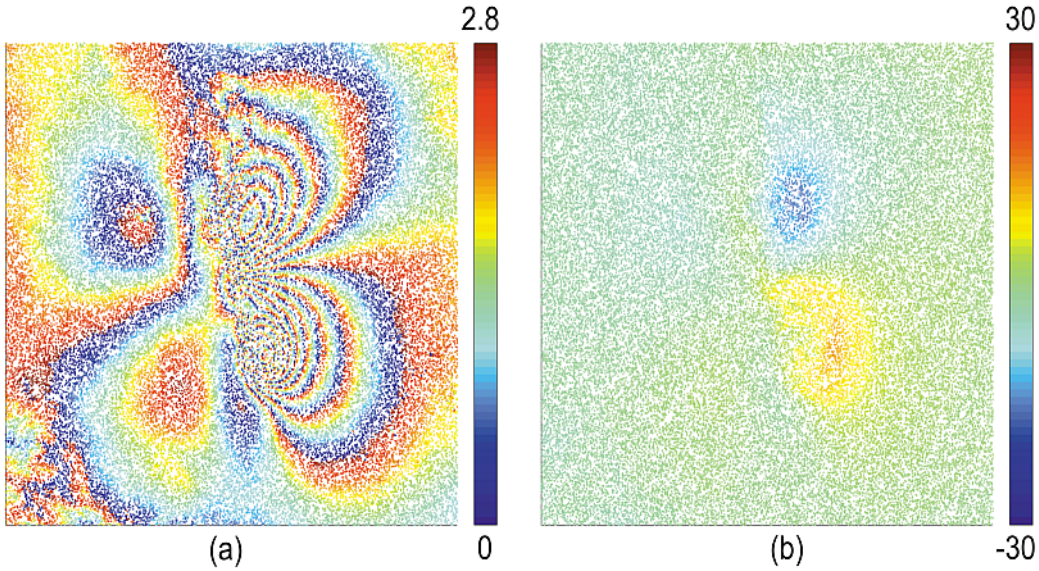

Figure 5.6: (a) Envisat ASAR interferogram of the Bam earthquake. 10% of the points were randomly selected from the complete interferogram. (b) The unwrapped interferogram using SNAPHU and deformation mode cost function. This can be directly compared with Figure 4(b,d) in Funning *et al.* (2005).

on Delaunay triangles and the basic algorithm implemented by the software. The examples shown in this section use only 10% of the interferograms which is almost 10 times as dense as conventional PS networks. However, these interferograms also have significantly larger deformation signatures than in regions that we have applied our PS-InSAR techniques (Chapter 6 and Chapter 7) to. Our unwrapping method works effectively on sparser data sets that are characterized by slower deformation fields.

5.4 Three-dimensional unwrapping

So far, we have discussed the two-dimensional phase unwrapping problem. Time-series InSAR allows us to sample the deformation signal as a function of time, albeit sampled irregularly. Hence, we need a different approach to incorporate this additional information in unwrapping these three-dimensional data sets. Huntley (2001) extended the idea of branch-cuts to three dimensional data sets and postulated that

residues connect to form loops or surface discontinuities in the 3D case. Subsequently, numerous branch-cut algorithms based on this idea have been developed for medical applications (Huntley, 2001; Cusack and Papadakis, 2002). Hooper *et al.* (2007) generalized the framework for time-series InSAR applications and argued that similar to shortest length linear discontinuities in the 2D case, residues are connected by surfaces with the smallest area in the 3D case. The MCF approach also has been extended to three dimensions for application with time-series InSAR techniques (Costantini *et al.*, 2001; Pepe and Lanari, 2006).

However, as we will show later in this chapter, residue-based unwrapping techniques are inflexible and cannot accomodate *a priori* information to constrain the unwrapped solutions. We developed the edgelist phase unwrapping algorithm to address some of the shortcomings of residue-based unwrapping algorithms and to allow us to unwrap spatially-sparse data sets, where the estimates of residues are less reliable due to the greater spatial separation of coherent phase estimates.

5.5 Edgelist phase unwrapping formulation

The edgelist phase unwrapping formulation addresses some of the limitations of the residue-based MCF formulation when handling spatially sparse time-series InSAR dataset. The edgelist formulation is inspired by the dual of the minimum cost flow problem (Ahuja *et al.*, 1999). In this section, we present the mathematical formulation for the edgelist phase unwrapping algorithm.

Let V represent the set of points ($|V| = N$) on which the set of measured wrapped phase values,$\{\psi_i\}$ where $i \in (1, \cdots, N)$, is defined. Let E define the set of edges consituting the unwrapping grid ($|E| = M$) on V such that, for every edge$(i, j) \in E$, $i < j$. Thus $G := (V, E)$ represents a directed graph which will be used to estimate the set of unwrapped phase values, $\{\phi_i\}$ where $i \in (1, \cdots, N)$. For simplicity, we assume that the graph G represents the Delaunay triangulation of the set of points V and

E represents the set of the edges of the triangulation. The wrapped and unwrapped phase values at each point in V are related by

$$\phi_i = \psi_i + 2\pi n_i \quad \text{where } i \in (1, \cdots, N) \tag{5.4}$$

where n_i represent the integer number of cycles that must be added to each point of the wrapped function to obtain the unwrapped function. These variables can be interpreted as node potentials (Ahuja *et al.*, 1999). For every edge (i, j) in E , we define a new variable K_{ij} such that

$$n_j - n_i + K_{ij} = \left[\frac{\psi_i - \psi_j}{2\pi}\right] \tag{5.5}$$

Here $[\cdot]$ represents the nearest integer function and K_{ij} represents the integer flow along the directed edge (i, j) and is equivalent to variables K_1 and K_2 in (Costantini, 1998). As in the original MCF formulation, we associate a non-negative convex cost function $f\left(K_{ij}\right)$ with the integral flow on every edge $(i, j]) \in E$. We can then state our minimum cost flow problem as

$$\text{Minimize} \qquad \sum_{\forall (i,j) \in E} f\left(K_{ij}\right) \tag{5.6}$$

Subject to

$$n_j - n_i + K_{ij} = \left[\frac{\psi_i - \psi_j}{2\pi}\right] \tag{5.7}$$

$$n_i \in \text{Integer} \qquad \forall i \in (1, \cdots, N) \tag{5.8}$$

$$K_{ij} \in \text{Integer} \qquad \forall\, (i, j) \in E \tag{5.9}$$

Our formulation differs from that of Costantini (1998) in that the basic unit in our algorithm is an edge on the unwrapping grid instead of a closed loop, hence the name "edgelist". This formulation also reduces to a variation of the convex cost integer dual network flow problem (Ahuja *et al.*, 1999). Lagrangian relaxation and cost scaling algorithms can be applied to solve the general convex minimum cost flow problem

(Equations 5.6-5.9) (Ahuja *et al.*, 1999). Following Costantini (1998), we restrict our discussion to minimum L_1 norm solutions for ease in implementation using LP solvers.

The salient features of the edgelist formulation include

1. The edgelist formulation reduces to the original MCF formulation if every edge of the Delaunay tessellation is included as a constraint (See Fig 5.7). The constraint of our phase unwrapping formulation when applied to the edges of a loop produces a loop constraint in the original MCF formulation.

2. The edgelist formulation does not distinguish between 2D and 3D data, where the third dimension is generally the time dimension in a series of interferograms. Each phase measurement is treated as a distinct vertex of the graph. Consequently, more variables and constraints are needed to completely define a problem. Table 5.1 provides a comparison of the resources for when each algorithm is applied to a 2D unwrapping problem.

3. The constraint matrix of the edgelist formulation is a total unimodular matrix (TUM, see Section 5.5.1) and the right hand side of the constraints in Equation 5.7 is an array of integers. Similar to the MCF and other TUM integer programming problems, the edgelist formulation can also be exactly solved as a linear program (LP) when the associated objective functions minimize the L_1 norm (Hoffman and Kruskal, 1965).

4. The edgelist formulation can readily incorporate other geodetic measurements such as GPS or leveling data as additional constraints without affecting the TUM property of the constraint matrix. This is discussed in detail in section 3.

We alter the general edgelist formulation (Equations 5.6-5.9) to allow minimum L_1 norm solutions using LP solvers by transforming the L_1 problem into a linear program. Define two new sets of non-negative variables P_{ij} and Q_{ij} , such that

$$K_{ij} = P_{ij} - Q_{ij} \quad \forall\,(i,j) \in E \tag{5.10}$$

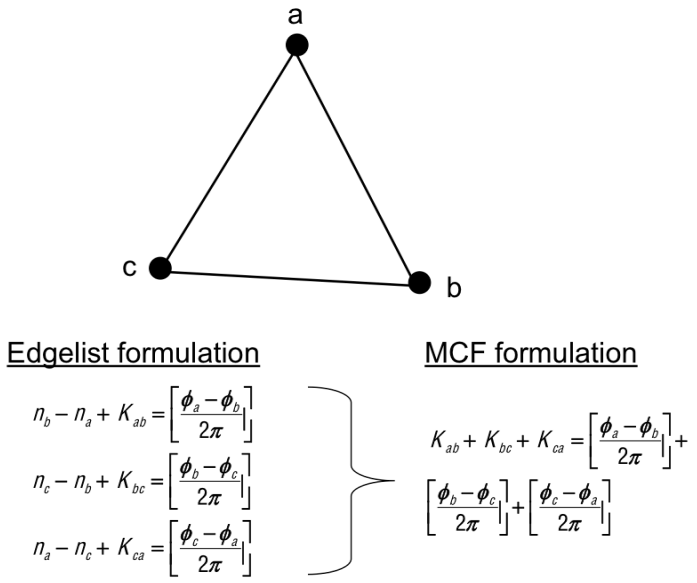

Figure 5.7: Comparison of the new edgelist formulation and the original MCF formulation. We obtain the constraints of the MCF formulation by summing up constraints of the edgelist formulation.

Table 5.1: Parameters needed to represent a regular grid 2D unwrapping problem of size M x N pixels using both the edgelist and MCF formulations.

	Minimum Cost Flow	Edgelist
Dimensions of interferogram	$M \times N$	$M \times N$
Number of variables	$4MN - 2M - 2N$	$5MN - 2M - 2N$
Number of constraints	$MN - M - N + 1$	$2MN - M - N$
Non-zero constraint matrix entries	$8MN - 8M - 8N + 8$	$8MN - 4M - 4N$

The resulting constraint matrix is also TUM (See Section 5.5.1). Hence, the integer program (Equations 5.6-5.9) can be solved exactly using its LP relaxation, where all the variables are allowed to be real valued. The solution to our phase unwrapping problem is thus obtained by solving the linear program

$$\text{Minimize} \qquad \sum_{\forall (i,j) \in E} C_{ij} \cdot (P_{ij} + Q_{ij}) \tag{5.11}$$

$$\text{Subject to}$$

$$n_j - n_i + P_{ij} - Q_{ij} = \left[\frac{\psi_i - \psi_j}{2\pi} \right] \tag{5.12}$$

$$n_i \in \text{Integer} \qquad i \in (1, \cdots, N) \tag{5.13}$$

$$P_{ij}, Q_{ij} \geq 0 \text{ and real} \qquad \forall\, (i,j) \in E \tag{5.14}$$

The node potentials and flows are solved simultaneously. As a result, the final unwrapping step involves simple addition of the node potentials to the wrapped values (Equation 5.4).

5.5.1 Total unimodularity

In this section, we prove the total unimodularity property of the constraint matrix in the edgelist formulation. We use the following properties to prove that the edgelist formulation can be solved using a real valued relaxation (Hoffman and Kruskal, 1965):

1. The incidence matrix (G_n) of a directed graph G is a totally unimodular matrix (TUM).

2. If matrix A is a TUM and I is an identity matrix of appropriate dimensions, then the following matrices are also TUM: $-A$, A^T, $[A, I]$, $[A, -A]$.

3. Let A be a $m \times n$ TUM matrix. Then the following polyhedrons are integral for any vector b of integers:

$$x \in R^n : \; A \cdot x \leq b$$

Revisiting the constraints for the edgelist formuation (Equation 5.7), the corresponding constraint matrix can be written as

$$[G_n \mid I] \cdot \begin{bmatrix} n \\ K \end{bmatrix} = b \tag{5.15}$$

where n represents the node potentials and K represents the flow variables. From properties (1) and (2) above, $A = [G_n \mid I]$ is TUM. Equation 5.15 can be reduced to the form described in property (3) above as

$$\begin{bmatrix} A \\ -A \end{bmatrix} \cdot \begin{bmatrix} n \\ K \end{bmatrix} \leq \begin{bmatrix} b \\ -b \end{bmatrix} \tag{5.16}$$

where all the entries of matrices A, b, n and K are integers.

Using property (3) above, we prove that our integer program (Equations 5.6 - 5.9) can be solved exactly by its real-valued relaxation, as all the corresponding extreme points are integers. A similar argument can be provided to show the LP relaxation (Equations 5.11 - 5.14) also has a totally unimodular constraint matrix and solves the integer problem of interest exactly.

5.5.2 Example

We illustrate the solution to our formulation using a LP solver on the example 3×3 square grid of Figure 5.8. The index of the pixel and the corresponding wrapped phase value are also shown in the format. A typical LP solver starts with a basic feasible solution and minimizes the objective function by altering the solution in the direction of highest negative gradient or the edge of the polytope with highest negative gradient. The linear program edgelist formulation (Equations 5.11 5.14) always has a basic feasible solution corresponding to all $n_i = 0$, $P_{ij} = \left(\left[\frac{\psi_i - \psi_j}{2\pi} \right] > 0 \right)$ and $Q_{ij} = \left(\left[\frac{\psi_i - \psi_j}{2\pi} \right] < 0 \right)$. In case of the example in Figure 5.8 and uniform costs for all edges, the basic feasible initial solution corresponds to all variables set to zero,

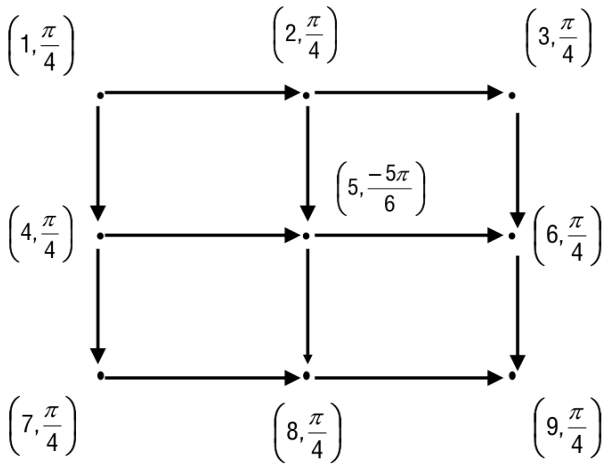

Figure 5.8: An example 3 x 3 grid with pixel index (i) and the corresponding wrapped phase values (ψ_i) shown in (i, ψ_i) format. The optimal solution corresponds to variable n_5 being set to one and all flow variables (K_{ij}s) set to zero.

except P_{25}, P_{45}, P_{56} and P_{58} which equal one. The LP solver alters the solution in the direction of the maximum negative gradient and the final optimal solution corresponds to all variables being set to zero except n_5 which equals one.

It is evident from Equations 5.11-5.14 that the solution is dependent on the unwrapping grid (G) used to define the unwrapping problem. We used Delaunay triangulations to obtain simple non-overlapping surface elements for the reliable points in each interferogram (Costantini and Rosen, 1999). In case of three dimensional PS-InSAR and SBAS data sets, these triangulations are replicated in space for each individual interferogram and form rectangular facets in time, following Hooper and Zebker (2007). The edgelist algorithm allows us to evaluate the unwrapped solution on customized unwrapping grids by defining the set of edges (E) appropriately. The optimal solution of Equations 5.11-5.14 also depends on the values of cost functions (C_{ij}) for the edges. These cost functions allow us to constrain the flow across the edges and is a feature that is common to both the original MCF and the edgelist formulations. For our time-series InSAR applications, we use the wrapped phase data itself to estimate spatial and temporal phase gradients for use in combination with the deformation mode statistical cost functions developed by Chen

and Zebker (2001). In section 5.7 we show an example where these cost functions are modified to include *a priori* information about the area being analyzed.

5.6 Incorporating other geodetic measurements as constraints

Often, complementary geodetic measurements such as GPS networks or leveling surveys are available in addition to frequent SAR acquisitions over regions of interest. This information can be used to direct edges in branch cut based algorithms or adjust cost functions in a network programming method for unwrapping interferometric phase, constraining the result to reflect these additional data. In branch cut algorithms, incorporating such changes involves defining and implementing a multi-criteria or Pareto optimal spanning tree problem (Zhou and Gen, 1997; Knowles and Corne, 2001). In the original MCF formulation, constraints based on additional observations can be defined but at the cost of violating the TUM property of the constraint matrix (Section 5.6.1). Violation of the TUM property renders the problem unsolvable exactly using LP solvers.

In the case of the edgelist formulation, if alternate geodetic measurements are available at points p and q, we introduce a new edge between the points (see Figure 5.9) and a new constraint in the formulation

$$n_p - n_q = \Delta N_{p,q} - \left[\frac{\psi_p - \psi_q}{2\pi}\right] \tag{5.17}$$

where $\Delta N_{p,q}$ is the expected number of unwrapped phase cycles between p and q. The new constraint adds additional entries to the original node but retains the TUM structure (Section 5.5.1). If the points p and q were already connected in the original unwrapping grid (G), the corresponding constraint for the edge in the unconstrained formulation (Equation 5.12) can be replaced by the new equation (Equation 5.17). Independent geodetic estimates of line of sight displacement for L vertices in V

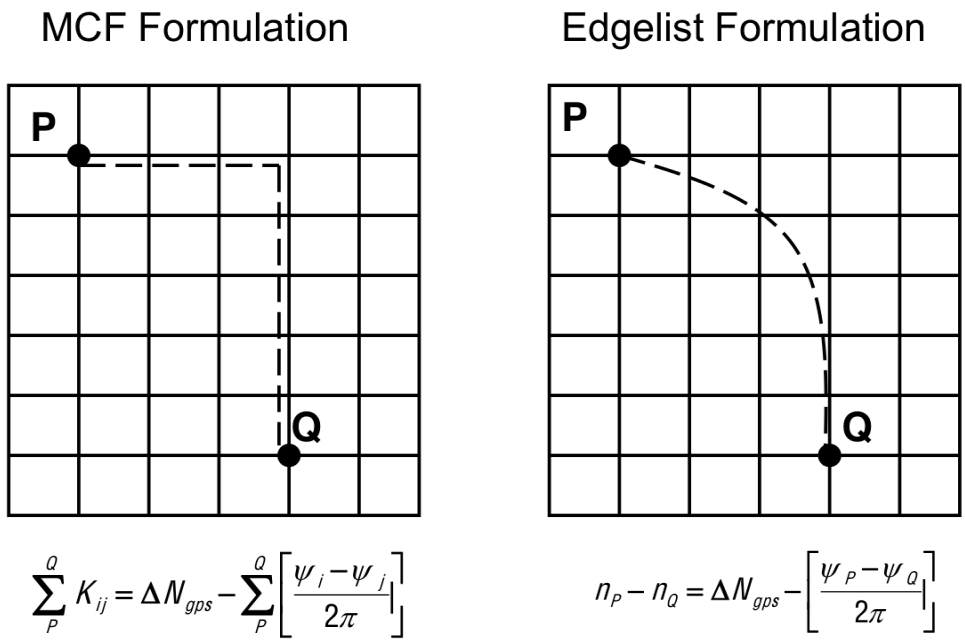

Figure 5.9: An example 3 x 3 grid with pixel index and the corresponding wrapped phase values shown in (i, ψ_i) format. The optimal solution corresponds to variable n_5 being set to one and all flow variables (K_{ij}'s) set to zero.

will allow us to construct $C(L,2) = \frac{L\cdot(L-1)}{2}$ additional equations to constrain our unwrapped solutions.

Simpler constraints of the form

$$0 \leq P_{ij} \leq u \quad \forall (i,j) \in E \tag{5.18}$$

$$0 \leq Q_{ij} \leq u \quad \forall (i,j) \in E \tag{5.19}$$

where u is a positive integer, can be further applied to reduce the solution space. These constraints do not affect the TUM property. The primary advantage of the edgelist formulation is that it provides us with controls over every data point (n_i) and every edge (P_{ij}, Q_{ij}) , as opposed to control over the edges alone in case of the MCF formulation. Both these properties can be suitably exploited to solve challenging unwrapping problems as shown in Section 5.7.

5.6.1 Total unimodularity

In this subsection, we prove that the constraint matrix for the edgelist formulation continues to be TUM after inclusion of external constraints of the form shown in Equation 5.17, whereas the MCF formulation no longer remains TUM on inclusion of external constraints. We use the following property of matrices to prove that the TUM property of our constraint matrix is violated on addition of external constraints for the MCF formulation:

1. A matrix with all elements in $\{0, +1, -1\}$ is TUM if it contains no more than one $+1$ and no more than -1 in each column.

We illustrate its proof using a regularly sampled 2D data set for ease of understanding. In the case of the original MCF formulation (Costantini, 1998), each edge of the unwrapping grid is traversed once in the clockwise and once in the anti-clockwise direction. If we assume a reference direction, the column of the constraint matrix corresponding to the flow variable K_i would have exactly one $+1$ and -1 in the rows corresponding to the loops of which it is a part. The constraint matrix satisfies property (1) shown above and hence is TUM. Suppose there were two GPS measurements at pixels p and q. Then the additional external constraint, corresponding to the MCF formulation, is of the form

$$\sum_{p}^{q} = \Delta N_{p,q} - \sum_{p}^{q} \left[\frac{\psi_i - \psi_j}{2\pi} \right]$$

where (i, j) is an edge along any chosen path from point p and point q and $\Delta N_{p,q}$ is the expected number of cycles in unwrapped phase, as observed by GPS. Adding this constraint violates property (1) above, and the resulting constraint matrix for the MCF formulation is not TUM.

In case of the edgelist formulation, adding external constraints is equivalent to adding additional edges to the unwrapping grid. Following arguments presented in Section 5.5.1, the node incidence matrix for any directed grid is TUM. This implies

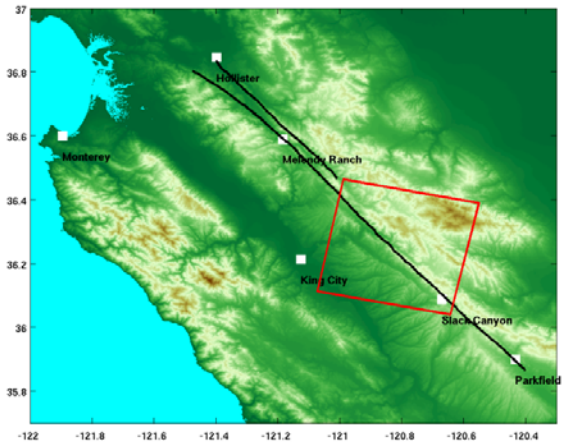

Figure 5.10: Map showing the location of the 40 km x 40 km area (red) being analyzed using PS-InSAR. Fault traces for the Central San Andreas Fault and Calaveras Fault are also shown in black. Locations of the Melendy Ranch and Slack Canyon creepmeters are also shown.

that the linear programming relaxation still produces an exact solution for the edgelist formulation including external constraints.

5.7 Case study: Creeping section of the San Andreas Fault

We applied our edgelist unwrapping algorithm to a persistent scatterer InSAR (PS-InSAR) data set covering an area of 40 km x 40 km around Monarch and Austin peaks (Figure 5.10) in the Central San Andreas Fault region. Conventional InSAR stacking in earlier studies characterized the spatial variation in slip deficit on the Central San Andreas Fault (Ryder and Bürgmann, 2008). However, the presence of large decorrelated areas close to the fault severely compromised the ability to reliably estimate the deformation just north of the fault (see Figure 2 from Ryder and Burgmann (2008)).

We processed 21 SAR scenes (Track 27, Frame 2781) acquired by the ERS-1 and ERS-2 satellites between 1992 and 2004. We selected a scene from March 1997 as

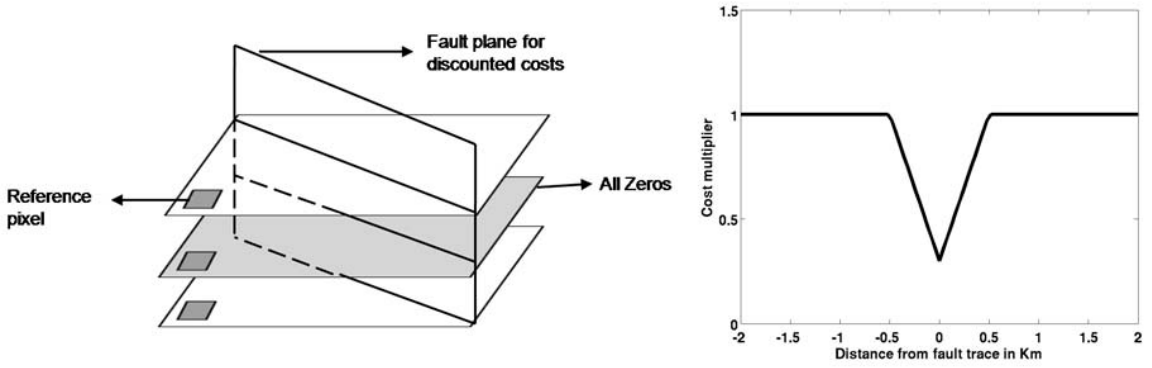

Figure 5.11: (Left) This figure shows the skeletal framework on which the PS-InSAR data set is unwrapped. Each slice represents an interferogram in the PS-InSAR time-series. All the node potentials in areas marked by red are set to zero. The plane of the fault trace is drawn in blue. (Right) The cost of the edges cutting across the fault is subsidized as a distance of center of edge from the fault as shown.

the master scene to minimize the combination of the perpendicular baseline and the temporal baseline in order to optimize the accuracy of the correlated phase estimates in the sparse PS network and generated 20 interferograms. We applied the maximum likelihood persistent scatterer (MLPS) selection algorithm (Shanker and Zebker, 2007) and found a sparse network of 2067 PS points per interferogram. Although the MLPS algorithm identified more PS points than other public domain algorithms, the PS density (1 per sq km) is still very low compared to the suggested threshold of 4 PS / sq km (Colesanti *et al.*, 2003) recommended for conventional PS-InSAR phase unwrapping algorithms.

Figure 5.12(a) shows the average LOS displacement rate in mm/yr and Figure 5.12(b) shows the average profile computed as a function of distance from the fault as computed by our algorithm (Equations 5.11-5.14, 5.18-5.19 above). To form this estimate, we also

1. Neglected elevation variation in the atmospheric phase screen, as the topography does not change by more than a few hundred feet in this area. Thus we compute unwrapped solution on a 3D grid similar to the Quasi-L_∞ norm algorithm of Hooper and Zebker (2007). This is different from the two-step approach of the

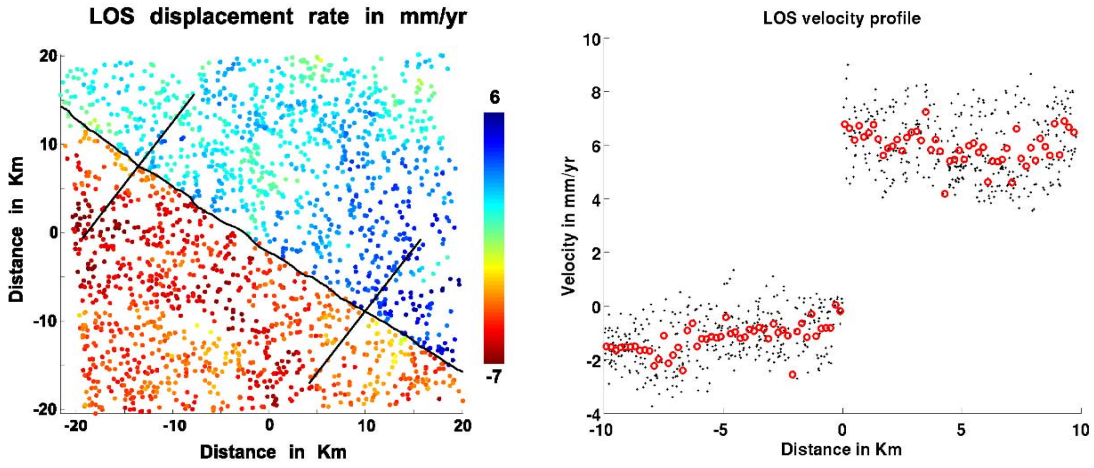

Figure 5.12: (Left) Average LOS displacement rate image estimated using the edgelist phase unwrapping algorithm. The fault trace and the area used for computing the average profile is also indicated. (Right) The average LOS displacement rate (red dots) as a function of distance from the fault is shown. Assuming all the displacement was purely due to strike slip motion across the fault, we estimate a slip rate of 22 mm /yr.

step-wise 3D algorithm (Hooper and Zebker, 2007) and the space-time MCF algorithm (Pepe and Lanari, 2006).

2. Introduced an interferogram consisting purely of zero interferometric phase values to represent the combination of the master scene with itself, into the time-series. All the node potential variables (n_i) for the vertices on the zero interferogram were constrained to be zero (See Figure 5.11a). This establishes a zero-reference frame with no discontinuities across the fault.

3. Chose the PS point with the highest temporal coherence as the master PS point (see Figure 5.11a). The phase of pixels in all the interferograms were referenced to the phase of the master PS point. The node potential for the master PS point is also constrained to be zero in all the interferograms. Thus, all the unwrapped phase values are estimated with reference to the master PS point.

4. Forced the solution to concentrate phase changes in the immediate vicinity of the fault trace, by identifying a region of 1 km width along the active fault

trace in which all cost functions (C_{ij}) associated with edges of the Delaunay triangulation and all time-edges of the points that lie within this zone were decreased. (See Figure 5.11b) This incorporates our knowledge that most of the creep is near the surface and that deformation decreases with distance from the fault. This is a good assumption for this fault but may not pertain to other parts of the world.

One of the main advantages of our method is that we do not require a temporal model for estimating deformation. The approach described above models the points on opposite sides of the fault as connected by loose (subsidized cost) strings, i.e., the unwrapped solution for a pixel depends more on the phase values of pixels on the same side of the fault as itself and less on the phase of pixels on the other side of the fault. Phase cycle jumps are preferentially compensated in the buffer zone. As a consequence, the unwrapped solutions in the buffer zone may not be entirely reliable due to the artificial discounts applied on the cost functions. But as we move away from the buffer zone, the solutions should be more accurate. Figure 5.12 shows the results obtained using our new algorithm.

It is useful to compare our solution to the results obtained by other algorithms. We have already noted the comparison with the Ryder and Burgmann (2008) stack, and see that the current solution produces estimates closer to the fault. We also reduced the data using the step-wise 3D phase unwrapping algorithm (Figure 5.14) (Hooper and Zebker, 2007). In this analysis we clearly see the presence of the fault, but there appears "leakage" of signal across the known fault trace. This likely can be attributed to the inability to accommodate multiple cycle jumps across the fault for the large temporal baseline interferograms in the data set. We overcome this problem by subsidizing the costs for edges cutting across the fault. In this area the fault creeps at roughly 22 mm/yr (approximately 7 mm/yr in the radar line of sight, LOS), so that interferograms with temporal separation of more than 4 years exhibit multiple cycles across the fault. In an L_1 or L_2 norm formulation, multiple cycle jumps are penalized more heavily than single cycle jumps and require careful,

and often impractical, adjustment of the cost functions. Also, the San Andreas Fault fully bisects the image and forms a line discontinuity. In other words, there is no direct connection between the regions on either side of the fault through an area that is not noisy in phase. As the phase unwrapping problem is set up as a minimiazation problem (Equations 5.11-5.14) multiple-cycle jumps across the fault are underestimated. The edges cutting across the fault are incorrectly unwrapped in the temporal unwrapping stage of the step-wise 3D algorithm (Hooper and Zebker, 2007), resulting in both overly smooth solutions and leakage of deformation signal across the fault.

Figure 5.13 shows the cumulative LOS displacements between regions that are located at a distance of 8 km on either side of the fault. For reference, the time-series from the Melendy Ranch and Slack Canyon creepmeters (courtesy USGS) are also included. The creep rates estimated by our method are consistent with the long-term trend of observations from the USGS creepmeters in the area. However, the PS-InSAR time-series exhibits a non-linear trend that needs to be further investigated. This is seen in the Ryder and Burgmann (2008) InSAR stack as well. We note that InSAR is more sensitive to the vertical component of the deformation than the lateral component, due to the steep look angles of the instrument. GPS stations in the area fail to characterize vertical deformation with comparable accuracy and are often not used in modeling any vertical motion associated with creep across the fault. Hence, vertical deformation could be one source of this observed non-linear trend that needs further investigation with additional time-series InSAR studies using data from more coherent high resolution X-band and L-band SAR sensors like TerraSAR-X and ALOS PALSAR.

Most creep studies in the Central San Andreas Fault region use a constant velocity to model the slip rate distribution at depth (Ryder and Bürgmann, 2008; Rolandone *et al.*, 2007). Other studies, such as Nadeau and McEvilly (2004), suggest that the recurrence of repeating microearthquakes affects the slip rate along the fault significantly. Comparing results with Nadeau and McEvilly (2004), we also observe a

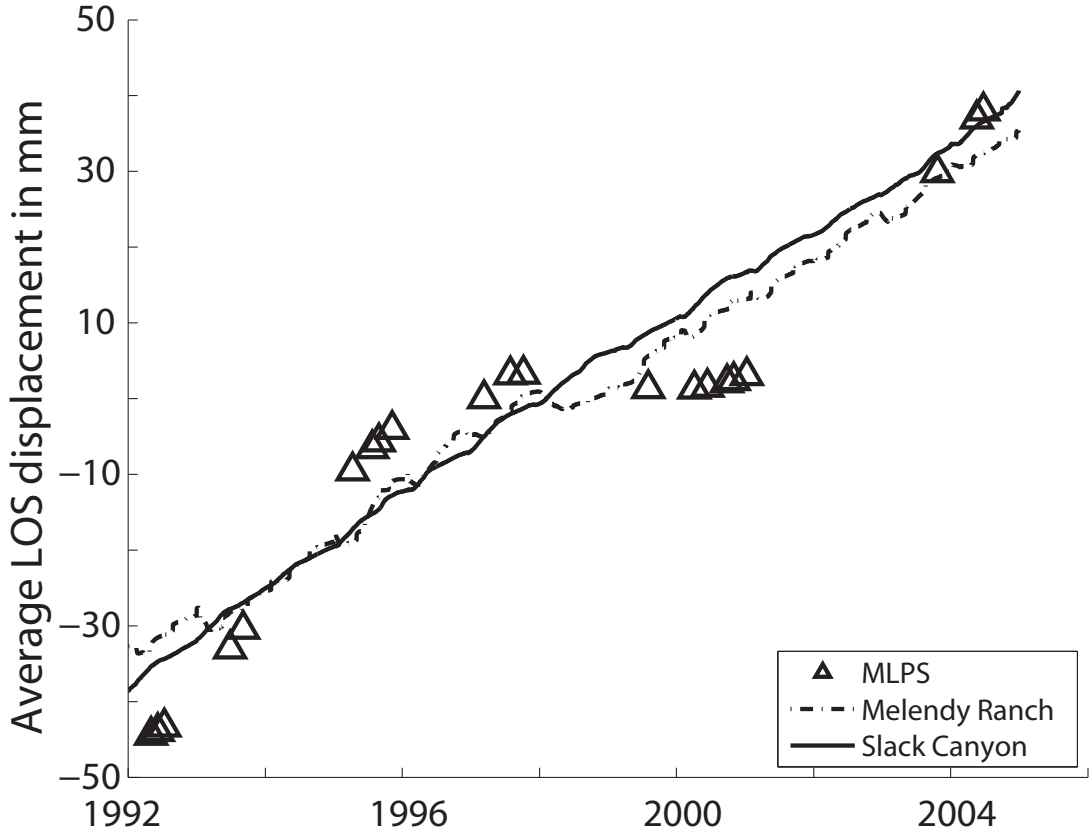

Figure 5.13: The cumulative displacement time-series for the regions marked out in Figure 5.12(a). The time-series from the creep meters at Melendy ranch and Slack canyon are also included for comparison. The creepmeter measurements have been projected on to the radar LOS direction for comparison.

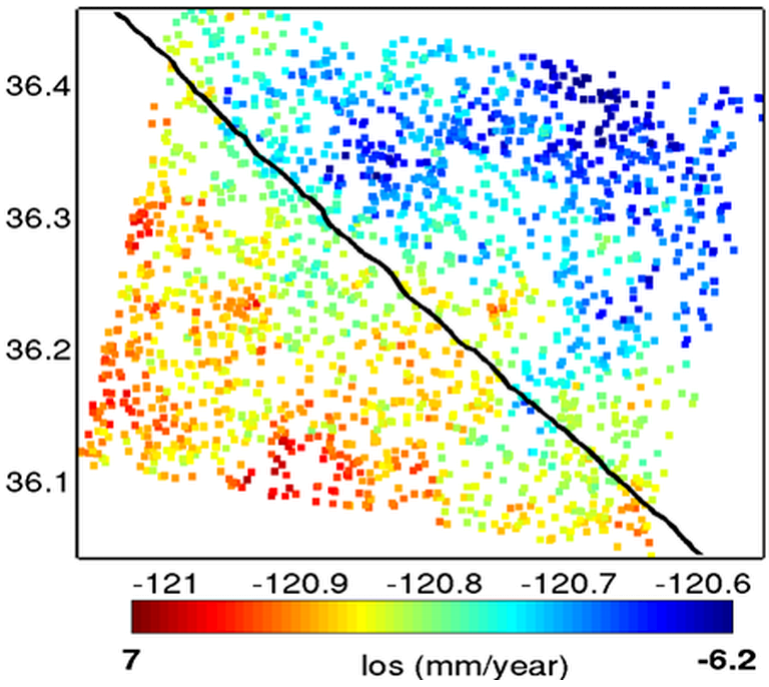

Figure 5.14: The average LOS displacement rate in mm/yr estimated using the stepwise 3D unwrapping algorithm (Hooper and Zebker, 2007).

similar pulse-like variation in slip rate in the time period 1992-1996 in Figure 5.13. If the results from our phase unwrapping method are plausible, the algorithm forms the basis for a new method to monitor the changing strain field over the entire Central San Andreas Fault area – spaceborne PS-InSAR is capable of measuring very small displacements over a large area.

5.8 Discussion and Conclusions

We present a new phase unwrapping algorithm that is as accurate but more flexible than previously known formulations. Our implementation exploits the TUM property that allows us to solve large scale phase unwrapping problems using LP solvers. Tests using simulated and real data sets demonstrate the validity of our new formulation. We implemented the edgelist algorithm using the simplex modules of the CPLEX software (CPLEX, 2006). In the absence of specialized constraints, illustrated in

the case study above, the edgelist formulation is computationally very inefficient compared to the original MCF algorithm and requires more computer resources. The quality of the solution however, matches that of the MCF formulation and permits a simplified representation of multi-dimensional phase unwrapping problem and the incorporation of data from external sources, like GPS, where available to better constrain the unwrapped solution.

The edgelist method provides a way to apply a priori knowledge to improve our ability to unwrap challenging data sets such as our case study above. Moreover, the algorithm is easier to implement at a smaller scale with fewer number of constraints and variables. This makes it an ideal candidate for improving the temporal unwrapping step of the multi-temporal PS-InSAR and SBAS phase unwrapping (Hooper and Zebker, 2007; Pepe and Lanari, 2006).

Chapter 6

Comparison of time-series InSAR methods: Rockslide mapping in Norway

In this chapter, we apply the PS-InSAR methods developed in Chapter 4 and Chapter 5 to study several rockslide sites in Troms County in the far north of Norway. In the process, we also the compare the results from our PS-InSAR technique against those from the Small Baseline Subset (SBAS) algorithm (Berardino *et al.*, 2002). We also take this opportunity to address the difference and similarities between the PS-InSAR and the SBAS multitemporal InSAR methods for displacement studies in rural terrain.

6.1 Introduction

The natural hazard of rockslides has a high socioeconomic and environmental importance in many countries. Norway is particularly susceptible to large rockslides due to its many fjords and steep mountains. One of the most dangerous hazards related with rock slope failures are tsunamis that can lead to large loss of life. It is therefore important to systematically identify potentially unstable rock slopes. Traditional landslide monitoring techniques are expensive and time consuming. Differential satellite interferometric synthetic aperture radar (InSAR) is an invaluable tool for land displacement monitoring, particularly for the slow and very slow

landslides (See Hungr *et al.* (2001) for classification). Improved access to archived satellite data has led to the development of several innovative multitemporal algorithms, including Persistent Scatterer InSAR techniques. We also study the same area with another popular time-series InSAR technique - the small baseline method (SBAS).

Being a mountainous country, Norway is particularly susceptible to large rock avalanches. In the last 100 years, over 170 people have been killed by tsunamis in fjords caused by large rock avalanches. In each case, the rock avalanche was preceded by many years of slow movement, with acceleration prior to slope failure (Eiken, 2008). With several thousand kilometers of inhabited coastline and valleys, it is a challenge to identify the hazards efficiently. Even when we suspect an area to be sliding, it may take several years of measurements to confirm it and extensive ground instrumentation to characterize the type of motion.

The evolution of potential rockslides has often been studied using structural geological methods (Braathen *et al.*, 2004; Chigira, 1992; Agliardi *et al.*, 2001). Recent studies concentrate on documenting rockslide kinematics and identifying geometric configurations particularly susceptible to sliding, e.g., (Braathen *et al.*, 2004; Henderson and Saintot, 2009). Less emphasis has been placed on the direct, empirical relationships between the development of structures, evidence for movement and subsequent effects on the geomorphological architecture (Colesanti and Wasowski, 2006). Reconciliation of field observations and conventional measuring techniques such as Global Navigation Satellite System (GNSS) receivers and Total Station measurements has often proven ambiguous or problematic. Such quantification is a necessary step in hazard and risk assessment (Solheim *et al.*, 2005).

Recently, the potential of a differential synthetic aperture radar approach has been investigated to study landslides by numerous research groups (Berardino *et al.*, 2003; Hilley *et al.*, 2004; Strozzi *et al.*, 2005; Rott and Nagler, 2006; Colesanti and Wasowski, 2006). The interferometric phase measurements, however, are affected by various decorrelation phenomena (Zebker and Villasenor, 1992). The

main limiting factors are atmospheric artifacts that can introduce a bias in the phase measurement (Zebker *et al.*, 1997), and temporal decorrelation that makes InSAR phase measurements unreliable over vegetated regions due to the change in relative position of the scatterers in a resolution element (Zebker and Villasenor, 1992). Another limitation is spatial baseline decorrelation which occurs when the interferometric baseline is not exactly zero. Since the radar receives the coherent sum of all independent scatterers within the resolution cell, these contributions are added slightly differently due to the different geometry. Spatial decorrelation leaves many image pair combinations infeasible in areas with steep terrain (Section 2.4).

Effects of various decorrelation phenomena can be reduced by combining multiple SAR observations using multi-temporal InSAR techniques. Using more than two SAR scenes leads to redundant measurements that can be used in more advanced time series methods. These methods can be broadly classified into Persistent Scatterer (PS-InSAR) and Small BAseline Subset (SBAS) methods. PS-InSAR methods work by identifying image pixels in a stack of interferograms generated with the same master that are coherent over long time intervals (Ferretti *et al.*, 2000; Hooper *et al.*, 2004; Kampes, 2006). On the other hand, SBAS methods use all possible SAR image combinations with a short spatial baseline to reduce the effects of spatial and temporal decorrelation (Berardino *et al.*, 2002; Lanari *et al.*, 2007b).

Each of these methods has its advantages and limitations, and both have proven to be effective in successfully estimating deformation time series in various regions (Lanari *et al.*, 2004a; Hilley *et al.*, 2004; Hooper *et al.*, 2007). In this chapter, we compare the PS-InSAR and SBAS methods as applied to rockslide mapping.

This chapter is organized as follows. In Section 6.2 and Section 6.3 we present the study area as well as the available SAR data. We also briefly discuss the geological setting of our test area, including the relevance of PS-InSAR and SBAS methods for analyzing such terrain. A short review of the SBAS implementation including a discussion of theory, system issues and implementation is provided in Section 6.4. In Section 6.5, we present the results obtained with both the PS-InSAR and SBAS

methods when applied to our test area. In Section 6.6 we discuss the results, and in particular the ability of both the time-series InSAR methods to handle various error sources in interferograms. Finally, Section 6.7 provides our conclusion and outlook on these new developments in InSAR and their impacts on the field of remote sensing of rockslides.

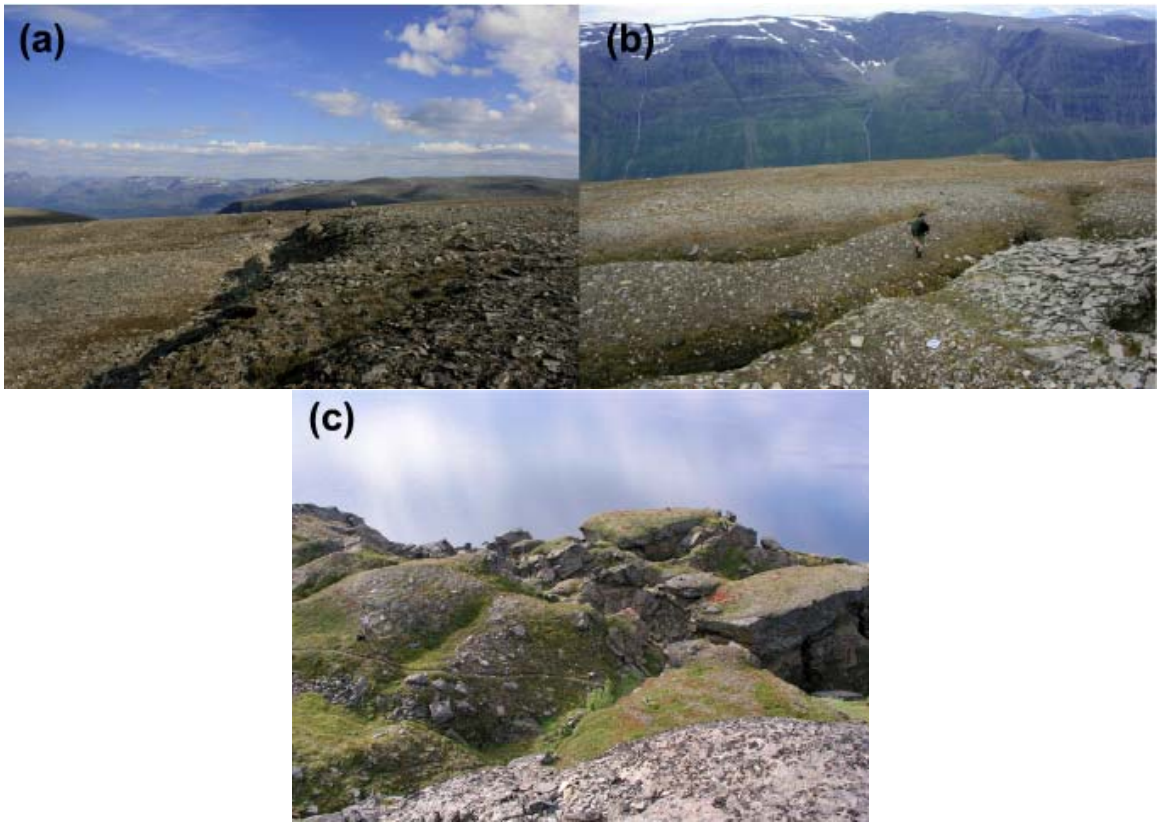

Figure 6.1: Photomontage illustrating typical scattering mechanisms that can be expected from the rockslide sites. (a,b). Gámanjunni. (c) Nordnes.

6.2 Study area

Since 2003, a comprehensive study involving several different institutions and international partners has focused on the investigation and documentation of the possibility for large rockslides in Troms County. Aerial photo analysis, field mapping, InSAR, LIDAR, differential GPS, continuous laser monitoring and 2D resistivity

analysis have been employed to identify potentially unstable rockslopes and further focus on those that are actively moving. A total of 75 sites has been identified (Henderson *et al.*, 2009b) by means of aerial photo analysis, regional satellite InSAR and helicopter reconnaissance, all with volumes ranging from 1 million m^3 to 500 million m^3. Geometric and kinematic models of movement of the different rockslides have both been identified and placed within a regional geometric and tectonic model where active faulting is both observed on the regional InSAR data and invoked as the driving mechanism for the regional distribution of rockslides (Osmundsen *et al.*, 2009). Detailed studies linking geology, geomorphology and the InSAR techniques presented here have been carried out on the scale of individual rockslides (Henderson *et al.*, 2009a). We focus on three rockslides (Gámanjunni, Rismmalčohkka and Nordnes), located in Troms County in the far north of Norway.

The photomontage in Figure 6.1(a–c) illustrates typical terrains in our test area. PS-InSAR methods rely on identification of pixels characterized by a dominant scatterer and operate on interferograms of the highest possible resolution. SBAS methods, on the other hand, are designed to identify pixels characterized by a distributed scattering mechanism and hence, operate on multi-looked interferograms (Section 2.5). In our area of interest, we can expect to observe a mixture of all types. We therefore expect that PS and SBAS methods will be complementary.

6.3 Available SAR data

Our analysis is based on 18 unique European Space Agency (ESA) ERS-1 and ERS-2 SAR data acquired from 1992 through 1999 (descending orbit, track 251, frame 2196), see Table 6.1. We selected only snow-free scenes. The ERS satellites have an operating wavelength of 5.66 cm, and the radar looks to the right (west for descending imaging geometry) with an angle of approximately 23.5° from the vertical. The radar is only sensitive to displacement changes with a component in the radar line-of-sight (LOS) direction.

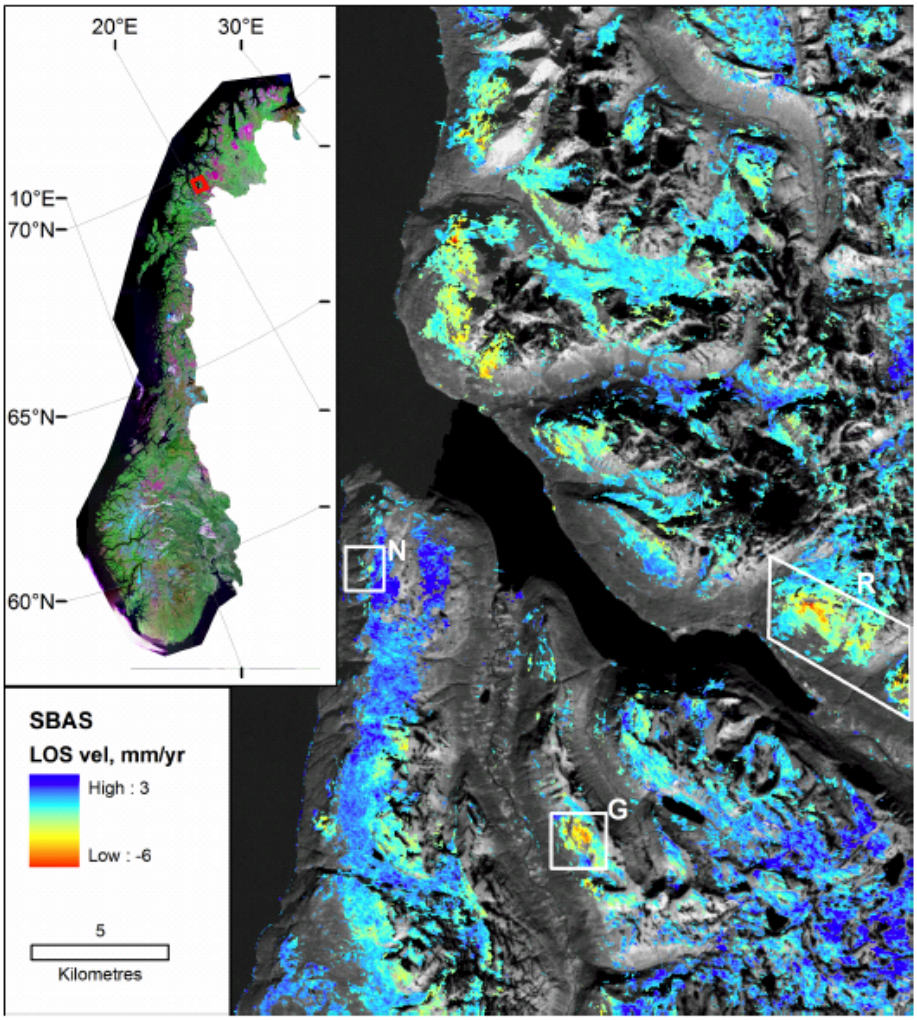

Figure 6.2: Landsat location map of study area in Troms County showing mean LOS velocity for the period of study (SBAS). Most of the identified rockslide sites are clustered around the presently active (Osmundsen *et al.*, 2009) Lyngen Fault Complex. Location of study area in Troms County in Norway shown in inset. The analyzed rockslides are marked with white rectangles.

Figure 6.3a shows the 65 interferograms that were computed using a maximum spatial baseline threshold of 600 m for the spatial baseline and a 5 years for the temporal baseline. Each line corresponds to an interferogram between two acquisition dates. We process the interferograms using the Norut GSAR software (Larsen *et al.*, 2005). We used a digital elevation model from the Norwegian Mapping Authority with a grid size of 25×25 m and a height standard deviation of 5–6 m to remove the topographic phase. A complex multi-look operation taking two looks in range and

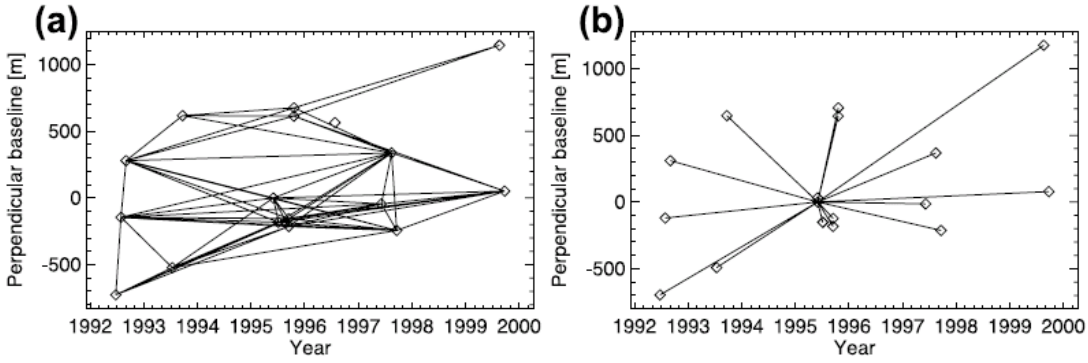

Figure 6.3: Baseline plot. (a) SBAS baselines relative to 1995-06-01. (b) PS baselines relative to 1995-06-02.

eight looks in azimuth, produced pixels with ground range dimensions of about 50 m in range and 50 m in azimuth direction.

Figure 6.3b shows the 15 interferograms computed with respect to the selected master scene (1995-06-02) for PS analysis. All interferograms were computed at full resolution, with pixel dimensions of approximately 20 m in ground range and 4 m in azimuth. The interferograms also span the time period from June 1992 to September 1999. We used the Norut GSAR software (Larsen *et al.*, 2005) for generating all interferograms. The topographic phase component was corrected using the same DEM as the one used for the SBAS analysis. We estimated topography related atmospheric phase screen for each interferogram and compensated before PS-InSAR analysis, as is described below in Section 6.3.1.

6.3.1 Atmospheric phase correlated with topography

The atmospheric phase component correlated with topography is a significant noise source in interferograms, especially in areas with varied topography (Onn and Zebker, 2006). The neutral atmospheric phase screen often is linearly dependent on topography as seen in GPS and InSAR data (Emardson *et al.*, 2003). Onn and Zebker (2006) showed that the topography-correlated neutral atmospheric phase screen can be empirically corrected using the phase information from the

interferograms themselves. Figure 6.4 shows a scatter plot of the interferometric phase for an example interferogram from Southern California against the DEM height (Onn and Zebker, 2006). A fit to these data provides the correction function.

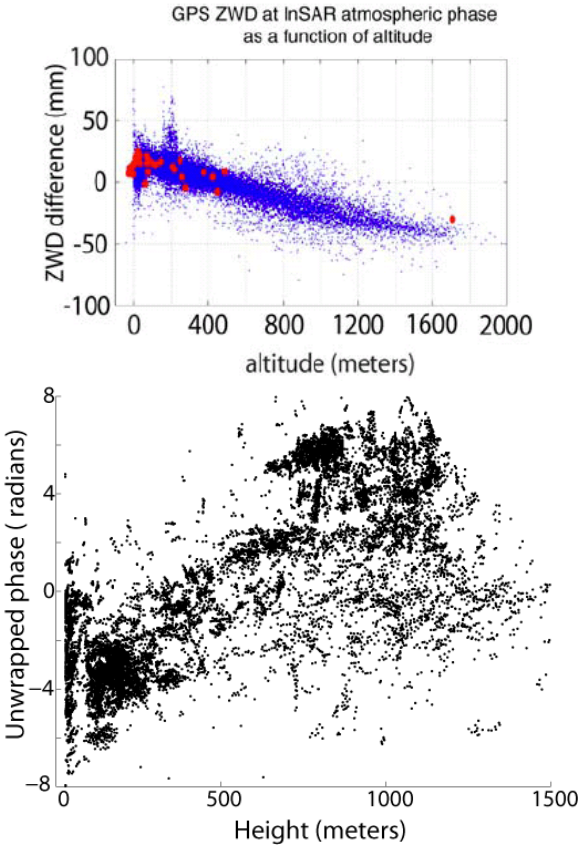

Figure 6.4: (Top) Interferometric phase (blue) and the GPS Zenith Wet Delay (red) plotted as a function of DEM height for an example interferogram in Southern California. For details see Onn and Zebker (2006). (Bottom) Interferometric phase of all pixels with coherence over 0.6 plotted as a function of height for an example interferogram over our test area.

A module to automatically estimate the phase screen as a linear function of the DEM height was incorporated into the GSAR processing chain following Emardson *et al.* (2003). The topography-related atmospheric phase component was compensated in all the interferograms used for producing results in Section 6.5 before the actual time-series processing.

Table 6.1: Used scenes from track 251, frame 2196.

Mission	Date (yyyy-mm-dd)	$B_\perp$ [a] (m)	B_t [a] (days)	Number of SBAS interferograms that scene is part of
ERS-1	1992-06-23[b]	-696	-1074	5
ERS-1	1992-07-28	-120	-1039	10
ERS-1	1992-09-01	310	-1004	10
ERS-1	1993-07-13	-491	-689	7
ERS-1	1993-09-21	647	-619	4
ERS-1	1995-06-01[d]	31	-1	10
ERS-2	1995-06-02[c e]	0	0	0
ERS-1	1995-07-06	-150	34	11
ERS-2	1995-07-07[c]	-154	35	0
ERS-1	1995-09-14	-182	104	11
ERS-2	1995-09-15	-123	105	11
ERS-1	1995-10-19	644	139	6
ERS-2	1995-10-20	706	140	5
ERS-2	1997-06-06	-14	735	8
ERS-2	1997-08-15	368	805	12
ERS-2	1997-09-19	-213	840	10
ERS-2	1999-08-20[b]	1175	1540	2
ERS-2	1999-09-24	78	1575	8

[a] Baseline relative to the scene 1995-06-02.
[b] Only in SBAS.
[c] Only in PS.
[d] SBAS master geometry.
[e] PS master geometry.

6.4 Short description of the SBAS algorithm

In this section, we review the fundamental concepts behind the SBAS multitemporal InSAR algorithm. For further details, we refer the readers to Berardino *et al.* (2002), Casu *et al.* (2006) and Lanari *et al.* (2007b).

Let us start by assuming a set of $N+1$ coregistered single look complex (SLC) SAR images. The first step of the SBAS algorithm is the generation of M multilooked small baseline differential interferograms. By restricting the maximum spatial baseline used, spatial decorrelation is reduced, and the effect of residual phase due to uncompensated topography is mitigated. On the other hand, such a baseline constraint can lead to a separation of the interferograms into several independent subsets in the baseline-time domain. The SBAS algorithm correctly retrieves the phase values as long as the subsets are overlapping in time.

We select a common set of coherent pixels in M interferograms as characterized by a high coherence in a selected fraction of the interferograms.

The SBAS algorithm relies on the availability of unwrapped phase values for all M interferograms (Berardino *et al.*, 2002). Consequently, a phase unwrapping step is needed to retrieve the absolute phase values from the (modulo 2π) wrapped interferometric phase (Goldstein *et al.*, 1988; Ghiglia and Pritt, 1998; Costantini, 1998; Chen and Zebker, 2001). A best fit plane is removed from the unwrapped phase to account for possible precise orbit errors in the unwrapped data.

After phase unwrapping and ramp removal, all pixels are referenced to a selected point, usually characterized by high coherence and *a priori* known deformation temporal model. The differential phase for a generic coherent pixel, in interferogram j, generated by combining SAR acquisitions at times t_B and t_A is (Berardino *et al.*,

2002)

$$\begin{aligned}\delta\phi_j &= \phi(t_B) - \phi(t_A) \\ &\approx \frac{4\pi}{\lambda}[d(t_B) - d(t_A)] + \frac{4\pi}{\lambda}\frac{B_{\perp j}}{r\sin\theta}\Delta z \\ &+ \frac{4\pi}{\lambda}[d_{\mathrm{atm}}(t_B) - d_{\mathrm{atm}}(t_A)] \\ &+ n_j, \qquad \forall j = 1, ..., M,\end{aligned} \tag{6.1}$$

where λ is the transmitted radar wavelength, $\phi(t_B)$ and $\phi(t_A)$ are the phases corresponding with the times t_B and t_A, $d(t_B)$ and $d(t_A)$ are the radar LOS projection of the cumulative deformation referenced to the first scene (i.e. implying $\phi(t_0) = 0$). We also include a phase term that is related to possible errors Δz in the applied digital elevation model (DEM) used for differential interferogram generation. This phase component is proportional to the perpendicular baseline for each interferogram $B_{\perp j}$, range distance r, as well as satellite look angle θ. A possible atmospheric signal (Zebker *et al.*, 1997; Ferretti *et al.*, 2000; Hanssen, 2001) is included in the terms $d_{\mathrm{atm}}(t_B)$ and $d_{\mathrm{atm}}(t_A)$. Decorrelation effects and other noise sources are included in the last term n_j. Note that the following processing steps are carried out on a pixel-by-pixel basis on all selected coherent pixels.

6.4.1 Estimation of DEM error and low pass displacement signal

We first estimate DEM error and displacement model parameters. We use a cubic temporal deformation model

$$\begin{aligned}\phi(t_i) &= \bar{v}\cdot(t_i - t_0) + \frac{1}{2}\bar{a}\cdot(t_i - t_0)^2 + \frac{1}{6}\Delta\bar{a}\cdot(t_i - t_0)^3 \\ &= \frac{4\pi}{\lambda}\cdot d(t_i)\end{aligned} \tag{6.2}$$

and write the unknown parameter vector as

$$\mathbf{x}^T = [\bar{v}, \bar{a}, \Delta\bar{a}, \Delta z], \tag{6.3}$$

where $\bar{v}$ is mean velocity, $\bar{a}$ is mean acceleration, $\Delta\bar{a}$ is mean acceleration variation, and Δz is DEM error.

As in (Berardino *et al.*, 2002), using a cubic model, we form a linear system with M equations (corresponding to the vector of unwrapped phase values $\boldsymbol{\delta\phi}$) and 4 unknowns

$$[\mathbf{AM}, \mathbf{c}]\mathbf{x} = \boldsymbol{\delta\phi}, \tag{6.4}$$

where $\mathbf{M}$ is an $N \times 4$ matrix corresponding to the parameters of the cubic displacement model in Equation 6.2, $\mathbf{c}^T = [(4\pi/\lambda)(B_{\perp 1}/r_1 \sin\theta_1, ..., (4\pi/\lambda)(B_{\perp M}/r_M \sin\theta_M]$ is a factor proportional to the DEM error, and $\mathbf{A}$ is an $M \times N$ difference operator matrix corresponding to the unknown cumulative phase values $\boldsymbol{\phi} = [\phi_1, \phi_2, ..., \phi_N]$ and the M interferograms. For details about $\mathbf{A}$ and $\mathbf{M}$, see (Berardino *et al.*, 2002).

We would like to point out that the cubic displacement model in Equation 6.2 is used only to help the estimation of the DEM error, while the final inversion to compute the displacement time series is independent of such a model, see Equation 6.5.

Since we apply a displacement model, the equation system in Equation 6.4 is generally simplified. For such a smooth temporal model, the product $[\mathbf{AM}, \mathbf{c}]$ is nonsingular. The estimate of $\hat{\mathbf{x}}$ can then be obtained in an optimal least squares (LS) way (Golub and Loan, 1996).

6.4.2 Estimation of cumulative phase

The estimated DEM error is subtracted from the unwrapped phase, forming the following linear system

$$\mathbf{Bv} = \boldsymbol{\delta\phi'}, \tag{6.5}$$

where $\boldsymbol{\delta\phi'} = \boldsymbol{\phi} - \Delta z \cdot \mathbf{c}$ is the redundant set of phase differences with the DEM error contribution subtracted, and the unknown coefficient vector is

$$\mathbf{v}^T = \left[v_1 = \frac{\phi(t_1)}{t_1 - t_0}, ..., v_N = \frac{\phi(t_N) - \phi(t_{N-1})}{t_N - t_{N-1}} \right]. \tag{6.6}$$

As in (Berardino *et al.*, 2002), we replace the unknown cumulative phase values $\boldsymbol{\phi}^T = [\phi_1, \phi_2, ..., \phi_N]$ with the mean phase velocity between time adjacent acquisitions. The design matrix $\mathbf{B}$ is changed accordingly, and now represents the cumulative time between each interferogram pair. Accordingly, a trivial integration step is needed to recover the final solution $\boldsymbol{\phi}$.

6.4.3 Atmospheric filtering and final displacement time series estimation

Atmospheric inhomogeneities can create an artificial atmospheric signal superimposed on each SAR image (Zebker *et al.*, 1997; Hanssen, 1998; Hanssen, 2001).

The atmospheric filtering approach used in the SBAS method is inspired by Ferretti *et al.* (2000) and Ferretti *et al.* (2001). The rationale behind the SBAS algorithm is to separate the different phase contributions (deformation, topographic error, atmospheric signal and decorrelation noise) by inverting a linear system of equations. In the atmospheric filtering step we exploit the spatial and temporal correlations of the atmosphere. The key observation is that the atmospheric phase component is highly correlated in space, but uncorrelated in time (Hanssen, 1998; Hanssen, 2001). The undesired atmospheric signal is estimated as follows:

1. the low pass deformation signal from Equation 6.2 is removed from the estimated deformation time series.

2. Following this, the residual phase signal is detected as the result of first, a temporal high pass filter with respect to the time variable, then a spatial low pass filter on the residuals.

Once the atmospheric signal has been estimated, it is subtracted from the estimated deformation phase signal. To obtain the final displacement estimate, the phase must be multiplied by the factor $\lambda/4\pi$.

6.5 Results

In this section we present the results from using the two multi-temporal InSAR techniques, PS-InSAR and SBAS. We focus on three specific rockslides where displacement has been identified and confirmed by field surveys performed by the Geological Survey of Norway (NGU) (Henderson *et al.*, 2009a; Henderson *et al.*, 2009b).

Common processing for both SBAS and PS-InSAR includes SAR processing and coregistration. We focused all raw SAR scenes into SLC images using the Norut GSAR processor (Larsen *et al.*, 2005). After focusing, we prewhitened and equalized the Fourier spectra of all SLCs, and coregistered the SLC images to a selected master geometry that was chosen to minimize both spatial and temporal baseline dispersion.

6.5.1 PS-InSAR procedure

For each complex interferogram, we first compute an amplitude calibration constant by summing up the absolute values of the area of interest (Lyons and Sandwell, 2003). We select an initial set of PS candidates after normalization of the amplitudes using the calibration values and a low threshold on the amplitude dispersion index (Ferretti *et al.*, 2001). We estimate phase contributions due to DEM errors using the perpendicular baseline estimates for each pixel and then subtract them from the measured interferometric phase values. The spatially correlated phase terms are iteratively determined for each of these PS candidates using the StaMPS software. We then apply the MLPS selection algorithm with a ML correlation threshold of 0.7. The identified PS network is then used to re-estimate all the spatially correlated

phase terms for each PS pixel. No explicit orbital ramp removal is necessary as this slowly varying term also includes the spatially correlated phase term.

We used the stepwise-3D phase unwrapping algorithm (Hooper and Zebker, 2007) to unwrap the sparse phase measurements. No deformation model was applied to aid the unwrapping process. Atmospheric phase screen and orbital phase ramps were estimated using a combination of a low-pass spatial filter and a high-pass temporal filter. A detailed analysis of the estimated deformation time series for three selected rockslides is presented in Section 6.6.

6.5.2 SBAS procedure

For each complex interferogram, we estimated and removed a best fitting linear phase ramp due to imprecise orbit knowledge (Lauknes *et al.*, 2005). After removal of the orbital phase ramp, the differential phase delay due to tropospheric stratification is estimated for each interferogram (Section 6.3.1). The main principle can be outlined as follows. Based on the individual differential phase estimates (two dimensional interferograms), we form a linear system where we invert the phase as a function of height for each SAR scene using a least squares approach. The resulting differential phase contribution due to atmosphere is then removed from each input interferogram.

In order to exclude decorrelated areas from the study, and to make phase unwrapping feasible, we applied a pixel thresholding, selecting only the pixels that exhibit an estimated coherence value larger than 0.25 in at least 30% of the interferograms. The overall phase coherence of the area is relatively high due to the limited vegetation cover above 600–700 m elevation.

Based on the selected pixels we apply a Delaunay triangulation and interpolation on all images (Costantini and Rosen, 1999). Thus, we are able to link spatially separated coherent patches. Following this operation, we unwrapped the interferograms using the SNAPHU software (Chen and Zebker, 2001). It should be noted that our preprocessing steps (orbital error ramp and stratified atmospheric removal) are crucial for a successful spatial unwrapping in this terrain.

After removing orbital trends and topography related atmosphere, as well as replacing the phase of low coherence points with Delaunay triangulated phase, we are left with a spatially correlated atmospheric signal. After the phase unwrapping step, all pixels are referenced to a chosen point on the eastern shore of the Lyngen fjord.

We then applied the SBAS algorithm described in Section 6.4 to the 65 InSAR pairs. For phase retrieval, we applied the new L_1 norm based SBAS phase inversion method presented in (Lauknes *et al.*, 2009).

The spatially correlated atmospheric contributions were estimated and filtered out before estimating a mean displacement velocity. Figure 6.2 shows the mean velocity rate over the analyzed area.

6.5.3 Differences in implementation

We summarize the main differences between the PS-InSAR and SBAS implementations in Table 6.2. Fundamentally, there are three major differences between our PS-InSAR and SBAS implementations:

1. The PS-InSAR method does not require any predetermined displacement model and yet successfully manages to identify the expected trend in LOS displacement. The SBAS method needs a temporal displacement model to separate DEM error from displacement.

2. We used the stepwise-3D algorithm (Hooper and Zebker, 2007) to unwrap the sparse 3D data set in our PS-InSAR implementation, while two dimensional phase unwrapping using the SNAPHU algorithm (Chen and Zebker, 2001) sufficed for our SBAS implementation.

3. Spatial filtering is an essential step in the StaMPS framework for identification of the PS pixels. No spatial filtering is needed in the SBAS inversion. Deformation estimates on a pixel-by-pixel basis results from inverting the unwrapped phase.

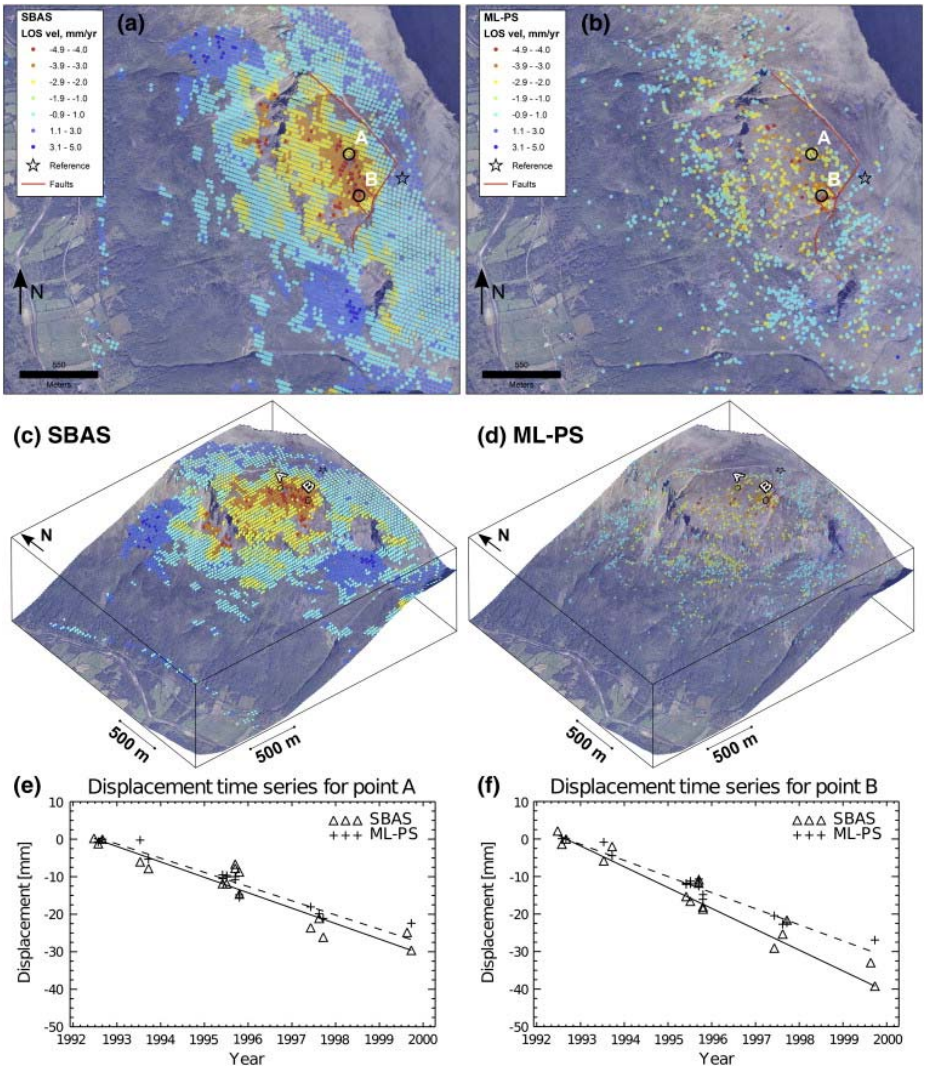

Figure 6.5: Detailed results from the Gámanjunni slide (see area G, Figure 6.2). (a–b) show the estimated mean velocity displacement rate maps overlaid on an aerial photo, while (c–d) show the same results draped on top of an aerial photo, for SBAS (a,c) and MLPS (b,d). (e–f) show the estimated time series for both SBAS and MLPS for points A and B, respectively. The mapped active structures are marked in (a–b).

6.5.4 Final displacement estimates

Figures 6.5–6.7(a–d) show the estimated mean LOS velocity in (mm/year) using both SBAS and MLPS methods. The mean velocity has been draped on top of an aerial photo in (a,b), and a DEM has been used to produce the three dimensional perspective view in (c,d).

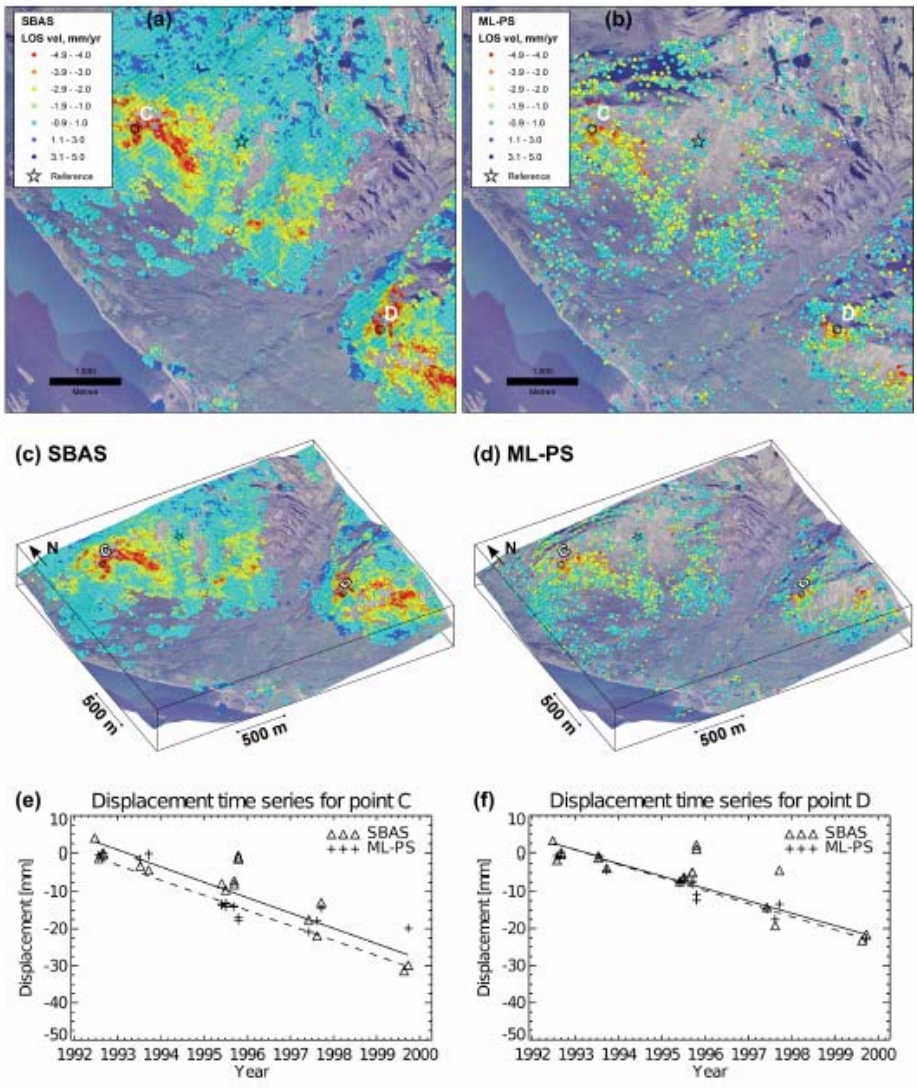

Figure 6.6: Detailed results from the Rismmalčohkka slide (see area R, Figure 6.2). (a–b) show the estimated mean velocity displacement rate maps overlaid on an aerial photo, while (c–d) show the same results draped on top of an areal photo, for SBAS (a,c) and MLPS (b,d). (e–f) show the estimated time series for both SBAS and MLPS for points C and D, respectively.

It should be remarked that, in order to ease comparison with the PS results, we have chosen to geocode each pixel from the SBAS results as an individual point. Consequently, when plotting the points, it appears that the data are rather sparse. Often, in reality, we do have complete spatial coverage.

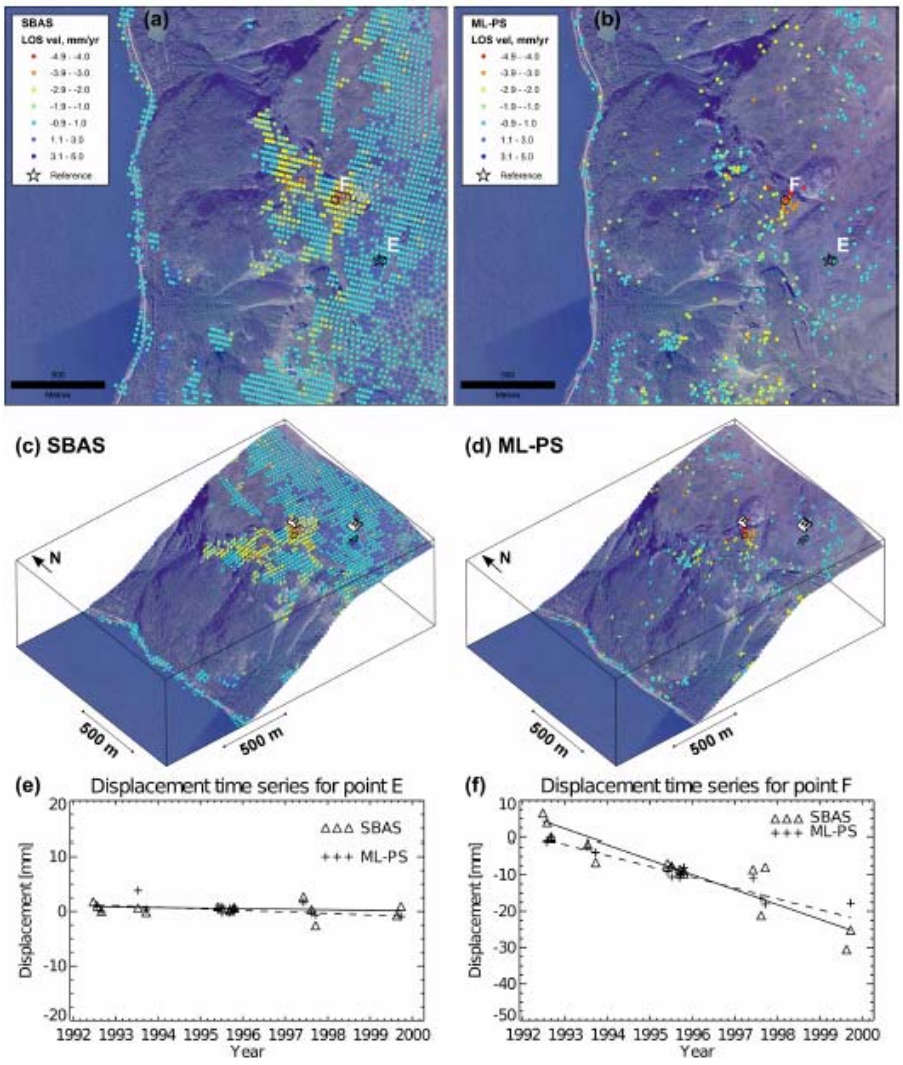

Figure 6.7: Detailed results from the Nordnes slide (see area N, Figure 6.2). (a–b) show the estimated mean velocity displacement rate maps overlaid on an aerial photo, while (c–d) show the same results draped on top of an areal photo, for SBAS (a,c) and MLPS (b,d). (e–f) show the estimated time series for both SBAS and MLPS for points E and F, respectively.

Figures 6.5–6.7(e,f) show the estimated LOS displacement time series for two selected points using both SBAS and MLPS methods. The positions of the two selected point areas are indicated in the mean velocity maps in Figures 6.5–6.7(a–d). The SBAS estimates have a pixel dimension of about 30×40 m, and the MLPS estimates retrieved at full resolution have a pixel dimension of 4×20 m, in the azimuth and range directions, respectively. In order to compare time series, we selected an area

of 3×3 pixels from the SBAS (corresponding to about 90×120 m on the ground), and used all PS pixels within this area. All points within the selected area were averaged as to produce a better estimate. In order to produce the time series, we referenced all points to a chosen reference area, marked with a star in the corresponding mean velocity plots from Figures. 6.5–6.7(a–d).

The triangles in the time series (Figs. 6.5–6.7(e,f)) correspond to the SBAS estimates, and the crosses correspond to the MLPS estimates. The lines correspond to fitting a linear model fit to the SBAS (solid line) and MLPS (dashed line) points using a least absolute deviation (L_1) method.

In Table 6.3 we summarize the estimated mean velocities for the time series plotted in Figures 6.5–6.7(e,f). In Table 6.3 we also show the computed root mean squared error (RMSE) between the linear model and the data, for both SBAS and MLPS.

6.6 Discussion

For all three areas, the SBAS results have greater spatial coverage compared to PS-InSAR. The absence of vegetation above 600–700 m altitude could explain this. Perhaps in these areas, distributed scattering mechanism dominates over the point target scattering mechanism. PS pixels possibly correspond to areas having large boulders located inside the resolution cell. We expect that more PS points are detected in areas where the scattering is of a "complex character", i.e. an area with mixed point scatterers and distributed scatterers, while the SBAS is better suited for areas where the scattering mechanism is distributed (see Figure 6.1 for scattering mechanisms). Our results show that the SBAS has greater coverage in all areas. This is in agreement with the photos in Figure 6.1(a–b), where a dominating distributed scattering is likely.

A look at the time series in Figures 6.5–6.7(e,f) shows that displacement estimates corresponding to certain acquisitions tend to be noisier than the others. In SBAS, these can probably be attributed to the number of interferogram combinations each

SAR scene contributes to, see Figures 6.3a and Table 6.1. If few interferograms are computed with respect to a scene, we expect that the inversion will be less robust for this point, and the noise level will be higher. In PS-InSAR, the noise on the temporal time series can be attributed to the baseline of the corresponding interferogram. In the StaMPS framework, spatially correlated terms are estimated by filtering each interferogram. In the case of interferograms with large baselines and sparse PS networks, these filtering estimates tend to be noisier.

It should be noted that PS-InSAR methods estimate the LOS velocity of the dominant scatterer in a resolution element, whereas the SBAS method estimates the average motion of all scatterers within a resolution cell. Therefore, slight variations between the velocities might occur.

For our study area, which is snow covered during large parts of the year, we can only use the summer and autumn scenes for analysis. Consequently, ascertaining seasonal variation in the rockslide displacement rates is difficult.

Another effect of using only data from the summer-autumn period is that the data points are clustered along the time dimension with a nearly periodic time spacing of one year. This makes the temporal atmospheric filtering challenging since we need to use long filter lengths. Furthermore, the irregularity of the temporal sampling can lead to filter end effects.

The difference in the PS and SBAS spatial pixel density for an area also affects our estimates of the two dimensional atmospheric signal, and hence the estimated deformation series.

In this work, we compare our time series results at the site level. The SBAS dataset has a better spatial coverage than the PS-InSAR dataset in this case. From the time series in Figures 6.5–6.7(e,f) we can see that the two methods follow each other quite well for all points selected. In general, the SBAS time series exhibit a larger spread around the fitted linear curve than the MLPS points. On average, the estimated root mean squared error (RMSE) between the linear fit and the data points

is 1.6 mm higher for SBAS than for MLPS, and the average mean velocity rates are within 0.5 mm/year of each other (Table 6.3).

6.6.1 Gámanjunni

The Gámanjunni rockslide (Figure 6.5) is located on a west-facing mountain at 1200 metres elevation and is bounded by two back-scarps (Henderson *et al.*, 2009a). The block volume is approximately 17 million m^3, and it is therefore among the biggest potential rockslides in Norway.

On the outcrop scale, the InSAR results are in close agreement with field observations. The spatial extent of the InSAR movement area matches extremely well with the area delimited by the active structures (See Figure 6.5. The block is subsiding at a rate up to 5 mm/year relative to the surrounding mountainside. Field evidence suggests that some fault segments have been active at different times and that previously active fault segments, which are now extinct, have been superseded by younger, more active faults, which are accommodating movement at present.

The NNW-SSE trending internal structures in the failing block are reflected in a NNW-SSE trending pattern in the InSAR data. This is seen in both the SBAS and PS data. Henderson *et al.* (2009a) demonstrated an apparent upward movement in the front of the block that is related to the failure mechanism, which is also faithfully recorded in both data sets, although it is more apparent in the SBAS data.

As indicated by Henderson *et al.* (2009a), we clearly observe that we are able to see differential movement patterns within the rockslide that can be directly correlated to the displacement profile of the individual faults and to the variable surface expression of the different faults. Based on the InSAR results, GPS monuments have been established. The monuments are measured once a year, and the preliminary differential GPS results are in broad agreement with the InSAR data (Eiken, 2008).

6.6.2 Rismmalčohkka

The Rismmalčohkka rockslide (Figure 6.6) is located on a south-west facing mountain between 600–1000 m elevation. The block volume is approximately 100 million m^3.

This rockslide geometry and architecture is fundamentally different from the sites of Nordnes and Gámanjunni, which form a more blocky, contiguous rock mass. The Rismmalčohkka slide covers a large area, but represents a rather "thin-skinned" rockslide where the total depth to the sole thrust is no more than 50–80 metres. The surface morphology consists of an extremely attenuated, rubbleized, moving mass. Hence, it is plausible that a distributed scattering model of the SBAS technique is better suited for InSAR analysis in this area compared to the dominant scatterer model of PS-InSAR.

6.6.3 Nordnes

Nordnes rockslide (Figure 6.7) shows the biggest difference between the two multi-temporal techniques among the areas analyzed. Both methods successfully identify the large deformation signal on the higher part of the rockslide. The spatial coverage of the PS-InSAR on the lower section is significantly lower than that of the SBAS technique, possibly indicating the nature of the scattering mechanism.

It can also be noted that in the Nordnes site, the SBAS method is able to resolve the faster moving, and more chaotically moving frontal part of the slide much better than the PS-InSAR method. This is probably related to the fact that the failure mechanism is much more chaotic in the most frontal part of the rockslide, with blocks tumbling in different directions.

6.7 Conclusions

SBAS techniques have a great advantage in that they can easily recover regional scale deformation, while PS techniques can be used for detailed and complimentary studies. Furthermore, the convergence between structural and InSAR descriptions of

the active rockslides is remarkable. Ground observations of fault geometry, evolution and developing footwall profile are precisely reflected in the SBAS and PS InSAR results. InSAR data have contributed to the detailed interpretation of the failure mechanism of several rockslides.

On the regional scale, large areas can be determined to be stable, thereby allowing rather expensive field activities to be focused on areas where movement has been detected. Our extensive experience in the ground-truthing of the InSAR method demonstrates a remarkable correlation between subsidence detected from the InSAR and mappable, unstable slopes in the terrain.

The millimetric precision of velocity determination, combined with the relatively high spatial resolution, allows detailed site characterization of many large rockslides. In addition to determining if a block is moving, we can discern subtleties such as differential velocities along an actively developing fault scarp. Although InSAR cannot be considered a replacement for ground based monitoring of active rockslides, it provides an important complementary dataset.

InSAR provides a new technique to determine potential rockslide movement and therefore provides a direct link between quantitative ground movement data and the structures, kinematics and changes of slope. Integrated studies using geological, geomorphological and newly developed remote sensing techniques are relatively few, e.g., (Jaboyedoff *et al.*, 2004). The direct linkage of InSAR data to structural geology and sliding processes is a new and novel niche in rockslide research and will prove to be a critical tool in future rockslide mitigation. Time-series InSAR techniques provide a detailed velocity maps of large areas covering entire landslides as opposed to sparse points on in case of GPS networks. This important characteristic of time-series InSAR will see it play a more important role in flow modeling of landslides in the future.

Table 6.2: Main differences between SBAS and PS.

	SBAS	PS
Main algorithms	(Berardino *et al.*, 2002; Casu *et al.*, 2006; Lanari *et al.*, 2007b).	(Ferretti *et al.*, 2000; Ferretti *et al.*, 2001; Werner *et al.*, 2003; Hooper *et al.*, 2004; Kampes, 2006; Shanker and Zebker, 2007).
Interferogram generation	Multilooked interferograms using the baseline thresholds as discussed in Section 6.4.	Full resolution interferograms with respect to the chosen geometry master image.
Pixel selection	Based on estimated coherence.	Based on estimated ML correlation.
Target scattering mechanism	Distributed scatterer pixel.	Pixel with dominant scatterer.
Resolution	Multi-looked (30×40 m).	Single look (4×20 m).
Phase unwrapping	Delaunay triangulation and SNAPHU (Costantini, 1998).	Stepwise-3D (Hooper and Zebker, 2007).
Low pass filter	Gaussian with dimension 1500 m.	Butterworth filter with cutoff of 800 m.
Temporal filter	Triangular (Bartlett) 400 days.	1 year Gaussian filter.

Table 6.3: Time series results from the three areas.

Area	SBAS mean (mm/year)	PS mean (mm/year)	SBAS RMSE (mm)	PS RMSE (mm)
Gámanjunni				
point A	-3.80	-4.12	3.17	2.00
point B	-5.57	-4.30	3.27	1.54
Rismmalčohkka				
point C	-4.16	-4.08	4.43	3.92
point D	-3.34	-3.52	4.92	1.80
Nordnes				
point E	-0.10	-0.28	1.06	0.98
point F	-4.08	-2.97	3.92	1.80

Chapter 7

Noise characteristics of PS-InSAR time-series: A case study of the San Francisco Bay Area

In this chapter, we describe the observed noise characteristics of deformation time-series estimated using the MLPS algorithm (Shanker and Zebker, 2007) in the StaMPS framework (Hooper, 2006). We use a dataset of 43 SAR scenes covering the San Francisco Bay Area for our analysis. In particular, we focus on the (1) Hayward Fault in the Oakland-Alameda region, (2) peninsula segment of the San Andreas Fault near the San Francisco airport (SFO) and (3) South Bay region, all of them imaged by ERS sensors during 1995-2000. First, we quantify the ability of the StaMPS framework to correct temporally uncorrelated phase error terms by analyzing the estimated deformation between ERS tandem scenes (separation of one day). We then quantitatively compare and cross-validate our time-series PS-InSAR results againt the results from the Small Baseline Subset (SBAS) InSAR time-series algorithm (Berardino *et al.*, 2002). We also compare our results against creep measurements from alignment arrays along the Hayward Fault (McFarland *et al.*, 2009).

We present in detail the estimated line of sight (LOS) velocities and deformation time-series for selected stations using both the time-series techniques, and successfully identify the salient deformation features in all three test regions. We show that the

root-mean squared difference in estimate line of sight (LOS) deformation between tandem pairs is about 4 mm. We also show that the root mean squared differences of the estimated mean velocities and deformation between the PS and SBAS time-series InSAR techniques are about 1 mm/yr and 5 mm, respectively. We also compare our deformation estimates against those from the creep meters of the San Francisco State University (SFSU) Fault Creep Monitoring Project. The observed discrepancies are within expected noise levels and design parameters of the time-series InSAR techniques.

7.1 Data

In this study, we compare deformation time-series processed over three sub-areas in the San Francisco Bay Area (Figure 7.1) using two different multi-temporal algorithms: Stanford University's MLPS algorithm in the StaMPS framework (PS) and IREA-CNR's SBAS technique relevant to the SBAS family of algorithms. We analyzed a total of 43 SAR acquisitions acquired during descending passes of ERS-1 and ERS-2 satellites (Track 70, Frame 2853) between May 1995 and December 2000. All the time-series InSAR products were produced using a common geometry corresponding to an acquisition from December 1997. 42 common-master interferograms were used for the PS analysis, and 124 multi-looked interferograms (20 azimuth looks and 4 range looks), corresponding to the network shown in Figure 7.2, were used in the SBAS analysis. There are no significant time gaps in the data set. Note that this area has been previously analyzed independently using these two techniques (Shanker and Zebker, 2007; Lanari *et al.*, 2007a; Lanari *et al.*, 2007b) but with different sets of SAR acquisitions. The SAR images were processed from Level-0 data at both Stanford and IREA-CNR, and the results were produced in radar coordinates for ease in direct pixel-to-pixel comparisons. The integer pixel offsets were then computed using the master SAR scenes and the results were aligned at the pixel level. The results from PS analysis were averaged over a window of 20 azimuth and 4

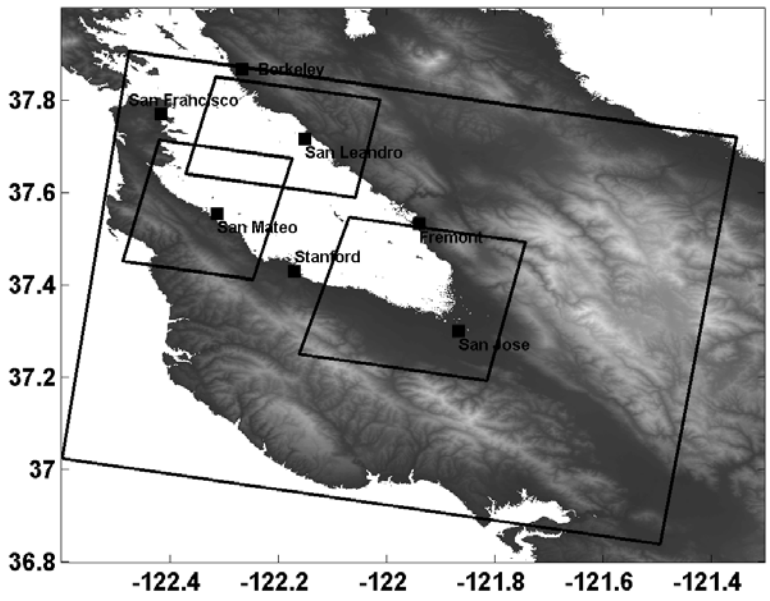

Figure 7.1: The locations of three sub-areas that were used in the time-series comparison, shown overlaid on the SRTM DEM of the region. The largest square represents the total area covered by the frame that was analyzed using the SBAS method.

range pixels to match the resolution of the SBAS analysis results. The PS results were processed as three different areal subsets due to the large data volume. The SBAS results were processed for the complete frame see Figure 7.1. The PS data set was unwrapped using the stepwise-3D phase unwrapping algorithm (Hooper and Zebker, 2007), while the SBAS time-series was estimated using the interferogram network shown in Figure 7.2 and the extended MCF phase unwrapping algorithm (Pepe and Lanari, 2006). The comparison of the results requires a common reference point. In our case, we choose the common reference pixel as the one with the maximum average temporal coherence (see Hooper (2006) and Pepe & Lanari (2006) for definition) as estimated using the PS and SBAS techniques. We also use a temporal filter of 400 days length to mitigate the effects of the seasonal variation of the ground water levels. These effects are significant in areas close to the bay (Lanari *et al.*, 2007b).

Unfortunately, there were no continuous GPS stations operating in these areas prior to 1999, and there were only two GPS stations with any overlap with our

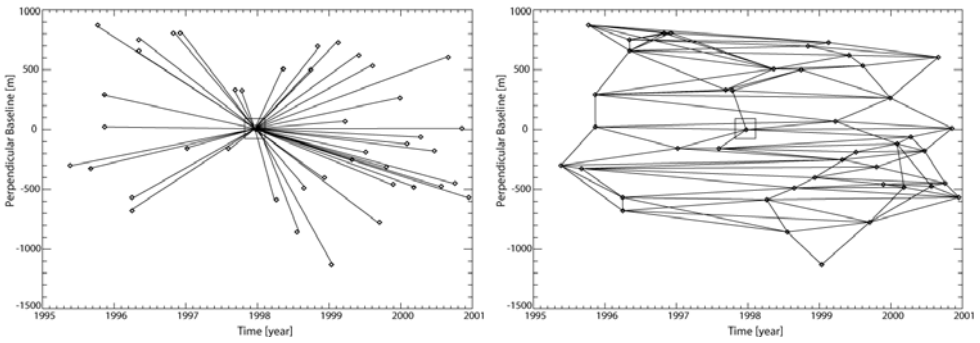

Figure 7.2: (Left) Time-baseline plot of the 43 ERS scenes (vertices) used for the PS-InSAR analysis. SAR scene from Dec 1997(square) was used for the master geometry. (Right) Edges between vertices represent the 124 interferograms used in the SBAS analysis. Again, the SAR scene from Dec 1997 (square) was used for the master geometry.

estimated time-series. Hence, we could not compare our deformation estimates against those from continuous GPS stations from networks that have since been added in the San Francisco Bay Area. San Francisco State University (SFSU) and the United States Geological Survey (USGS) maintain a network of alignment arrays across the active sections of the Hayward Fault (McFarland *et al.*, 2009). Eight stations between Kilometers 23 and 46 are covered by one the sub-areas that we analyzed and were used for direct comparison with our estimated deformation estimates. The data is freely available for download at `http://pubs.usgs.gov/of/2009/1119/`.

7.2 Methodology

We use three different methods to analyze our estimated deformation time-series. In the first technique (Section 7.2.1), we focus on tandem pairs in the time-series. No external geodetic observations are used to quantify noise levels in this case. In the second technique, we compare our results against those obtained from another indepedent time-series technique belonging to the SBAS family of algorithms in Section 7.2.2. This comparison yields a measure of degree of consistency in the estimated deformation signal by the two time-series InSAR techniques. Finally, we

compare our results against ground truth in the form of creep measurements from the SFSU-USGS alignment array.

7.2.1 Tandem SAR scenes

Let $P(x,t)$ represent the estimated PS-InSAR deformation time-series with spatial index "x" at time "t". We identified three pairs of ERS tandem scenes (Duchossois *et al.*, 1996) in our set of 43 SAR scenes - $10-11$ Nov 1995, $29-30$ Mar 1996 and $03-04$ May 1996 and analyzed the difference in estimated time-series on a pixel-by-pixel basis. The deformation phase term ($\phi_{defo,x,t}$ in Equation 3.14) does not change significantly over 24 hours. Hence, the estimated difference is a quantitative measure of our ability to correct for other temporally uncorrelated noise sources such as orbit error and atmospheric propagation delay. In the case of our PS-InSAR implementation, it is a measure of the ability of the StaMPS framework (Hooper, 2006) to distinguish the deformation signal from noise. We use the the standard deviation of the difference in deformation estimates ($\sigma(P(x,t+1)-P(x,t))$) to quantify the noise levels.

7.2.2 Inter-comparison with SBAS

Let $V_D(x)$ represent the difference in mean line-of-sight (LOS) velocities as estimated by PS and SBAS techniques at point with spatial coordinates "x". We analyze the average difference, $E(V_D(x))$, and the standard deviation, $\sigma(V_D(x))$, of the difference in the estimated velocities over all commonly identified coherent pixels. We calculate similar statistics for the estimated LOS time-series by assuming that $D(x,t)$ represents the difference in the estiamted PS and SBAS LOS deformation time-series at point with spatial coordinates "x" at time instant "t". In particular, we estimate the average difference, $E(D(x,t))$, and the standard deviation of the difference, $\sigma(D(x,t))$, by assuming that the difference of estimates at every time-instance is independent. We also report the mean standard deviation $E(\sigma_x(D(x,t)))$, where σ_x represents the standard deviation for a fixed spatial index, between the

time-series of commonly selected coherent pixels. Similar statistics have been used in previous work, including the PSIC4 study (Raucoules *et al.*, 2009), to validate the estimated time-series against continuous GPS and/or leveling measurements (Casu *et al.*, 2006; Crosetto *et al.*, 2008; Ferretti *et al.*, 2009; Adam *et al.*, 2009).

7.2.3 Comparison with alignment arrays

We compare the estimated creep across the Hayward Fault from PS-InSAR at 8 different stations with observations from the SFSU-USGS alignment array (McFarland *et al.*, 2009). For estimating creep across the fault from the PS results, we average the deformation estimates over an area of 500 m $\times$ 500 m on either side of the fault adjacent to the station of interest and analyze the time-series of the difference. We project the cumulative displacement observations of the creep meters to radar LOS, assuming no verical deformation, for direct comparison with estimated deformation time-series. We interpolate the creep meter observations using cubic splines to create a time-series that corresponds to the SAR image acquisitions. We represent the difference between the estimated PS time-series and the interpolated creep meter measurements at a station x, as $\Delta(x,t)$ respectively. Like in Section 7.2.2, we report the mean bias ($E\left(\Delta\left(x,t\right)\right)$) and the standard deviation ($\sigma\left(\Delta\left(x,t\right)\right)$) for the 8 alignment array stations. We also report the difference in estimated average velocity ($\Delta_v\left(x\right)$) between the PS-InSAR results and the alignment array creep measurements. The SBAS results used in this work were previously compared against the alignment array measurement and reported in Lanari *et al.* (2007a).

7.3 Results

Table 7.1 shows the statistics of the number of coherent pixels identified by the two time-series InSAR techniques. We used a phase noise threshold of 5 mm in the MLPS algorithm (Shanker and Zebker, 2007) for identifying the PS and a temporal coherence threshold of 0.7 (see Pepe and Lanari (2006)) for identifying the SBAS

pixels. The SBAS technique identified a slightly larger number of coherent pixels, which is consistent with observations over other regions (Lauknes *et al.*, 2010). Both the techniques identified a similar network of coherent pixels (85 percent in common), mostly in the urban areas. The MLPS algorithm performs slightly better in the non-urbanized zones.

Table 7.1: The statistics of the number of coherent pixels identified by each time-series InSAR technique. The PS results were generated at single-look interferogram scale and the results were multi-looked to match the resolution of the SBAS results.

Property	SFO Airport	San Leandro	South Bay
Size of the area in pixels (Azimuth × Range)	375 × 300	300 × 375	412 × 375
Pixels with PS estimates	13448	26956	55279
Pixels with SBAS estimates	15653	29160	61510
Number of common pixels	11222	23281	49134

Figure 7.3 shows the histogram of the difference in deformation estimates for one of the tandem pairs ($P(x,t+1) - P(x,t)$) for the SFO airport region. It is evident that the difference is normally distributed with almost zero mean. The non-zero bias can be attributed to noise in the selected reference pixel. Table 7.2 tabulates the tandem data noise levels for all the three tandem pairs and the sub-regions of the San Francisco Bay Area and indicates that an average of $3-4$ mm of noise is observed between tandem pairs. Assuming that noise from both the scenes contribute equally (factor of $1/\sqrt{2}$) to this estimate, we estimate a noise level of $2-3$ mm for every SAR scene.

Table 7.2: Standard deviation of the difference $[\sigma(P(x,t+1) - P(x,t))]$ in estimated PS-InSAR time-series for the three tandem pairs of data in our series of 43 SAR scenes.

Dates	SFO Airport	San Leandro	South Bay
$10-11$ Nov 1995	2.79 mm	2.94 mm	2.85 mm
$29-30$ Mar 1996	3.76 mm	3.72 mm	3.67 mm
$03-04$ May 1996	3.88 mm	3.82 mm	3.81 mm

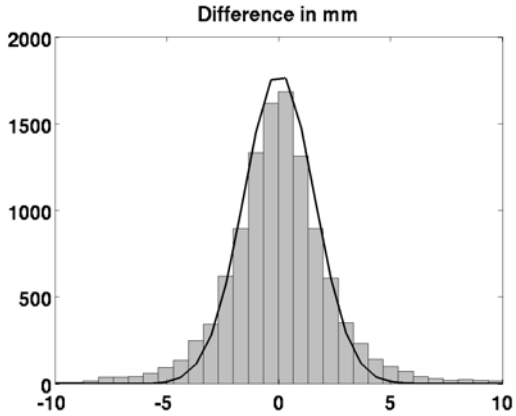

Figure 7.3: Histogram of the LOS time-series differences between the $10-11$ Nov 1995 tandem pair for all the PS pixels over the SFO airport region. Note that the histogram has a Gaussian structure. The best fit Gaussian distribution is also shown.

In Figure 7.4 we present the mean deformation velocity maps computed using the two techniques. It is clear that both the PS and the SBAS approaches identify the major deformation features in the San Francisco Bay Area. These include the subsidence of the SFO airport runway (SFO airport sub-area, Figure 7.4 (a)), the uplift due to the San Leandro synform (Marlow *et al.*, 1999; Schmidt *et al.*, 2005), rapid subsidence of many areas near the coast like the Bay Farm Island (San Leandro sub-area, Figure 7.4 (b)), the differential uplift across the Silver creek Fault in San Jose (South Bay sub-area, Figure 7.4 (c)), and the creep across the Hayward Fault near Oakland and Fremont (Figure 7.4 (b,c)). In addition to comparing mean deformation velocities, we also directly compared the estimated time-series for select stations shown in Figure 7.4 (a3,b3,c3). The individual time-series for creep across the Hayward Fault (Figure 7.5 (b5)) and differential subsidence across the Silver Creek Fault (Figure 7.5 (c5)), were produced by averaging rectangular regions on either side of their fault and computing their difference. Subsidence of regions along the San Francisco Bay like Candle Stick Point (Figure 7.5 (a1)), Bay Farm Island (Figure 7.5 (b1)), Alameda Ferry (Figure 7.5 (b2)) and Shoreline Park (Figure 7.5 (c1)) are also given. Few systematic differences between the results from the two techniques are observed, as expected. From the difference between the estimated velocities

(Figure 7.4), we note that the MLPS technique underestimates the subsidence, by more than 2 mm/yr, of rapidly subsiding reclaimed areas located near the Bay, such as the runway of the SFO airport (Figure 7.5 (a3)), the edge of Bay Farm Island (Figure 7.5 (b1)) and the shoreline park (Figure 7.5 (c1)). This could be a consequence of the spatial filtering effects of the StaMPS framework (Hooper, 2006). In the StaMPS framework, deformation is estimated from the unwrapped data using a combination of a spatial low pass filter and a temporal low pass filter. If the dimensions of the filter are large, some of the localized subsidence features are smoothed out. This filtering however, does not affect our estimates of fault creep as the physical dimensions of these features are significantly larger than those of the applied filters. We also observe some boundary effects in the processing. The three PS data sets were processed independently to reduce the workflow data volumes while the whole frame was processed as a single data set for the SBAS analysis before subsets were created for comparison. As a result, the PS pixels near the subset boundaries are insufficiently constrained in the phase unwrapping step compared to the SBAS data set. Hence, the differences between the velocity estimates near the edges are more than 1 mm/yr higher than over other parts of the image. Moreover, note that the time-series estimated using the PS and SBAS techniques physically represent the motion of the dominant scatterer in the resolution element and the average motion of the scatterers in the resolution element respectively. These values could be physically different. Different phase unwrapping algorithms (Hooper and Zebker, 2007; Pepe and Lanari, 2006) could be another source of difference between the two results. Table 7.3 shows the statistics related to the difference in deformation estimates from the two time-series InSAR techniques. From Figure 7.6, it is clear that the error statistics are normally distributed and can hence, be characterized by their mean and standard deviation. As described in Section 7.2.2, we also report the mean pixel-by-pixel standard deviation as this statistic has been widely used in other studies for quantifying estimation errors and differences. In summary, by taking into account

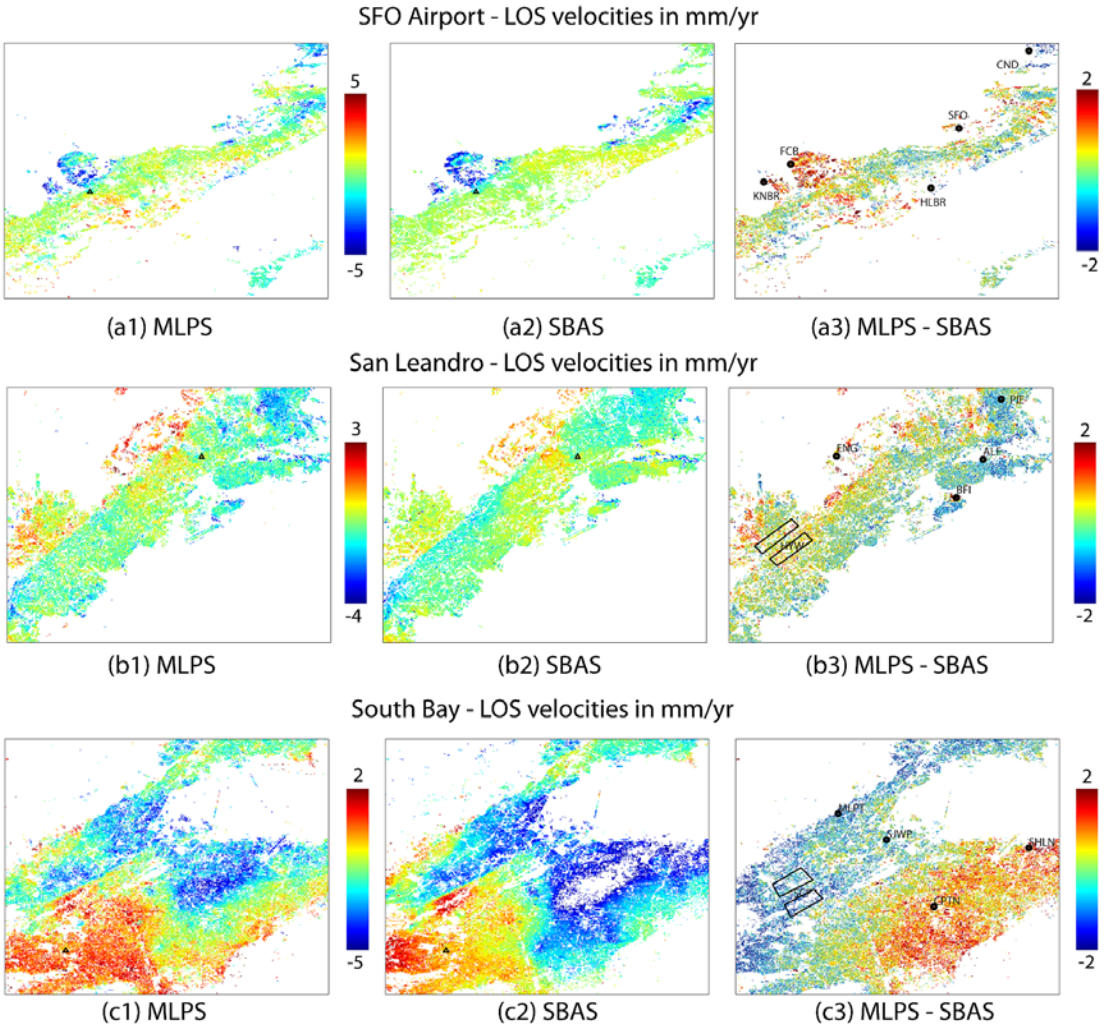

Figure 7.4: LOS velocity in the three different regions of the San Francisco Bay Area as estimated using the MLPS method (Left) and the SBAS method (Middle). The common reference point is indicated by a black triangle in each of the images. (Right) The differences between the velocity estimates are also shown. The stations for which individual time-series are shown in Figure 7.5 are marked by circles. The areas across the fault used to compute the creep across the Hayward Fault (b3) and the differential subsidence across the Silver Creek Fault (c3) are also shown.

for Table 7.3 values, we can assume that the average difference in estimated LOS velocities is in the order of 1 mm/yr and the estimated LOS time-series is 5 mm.

Figure 7.7 shows the estimated creep using PS-InSAR and the observed creep from the SFSU-USGS alignment array. Stations H39A (Figure 7.7(c)) and HENC (figure 7.7(e)) show the most discrepancy between creep meter observations and

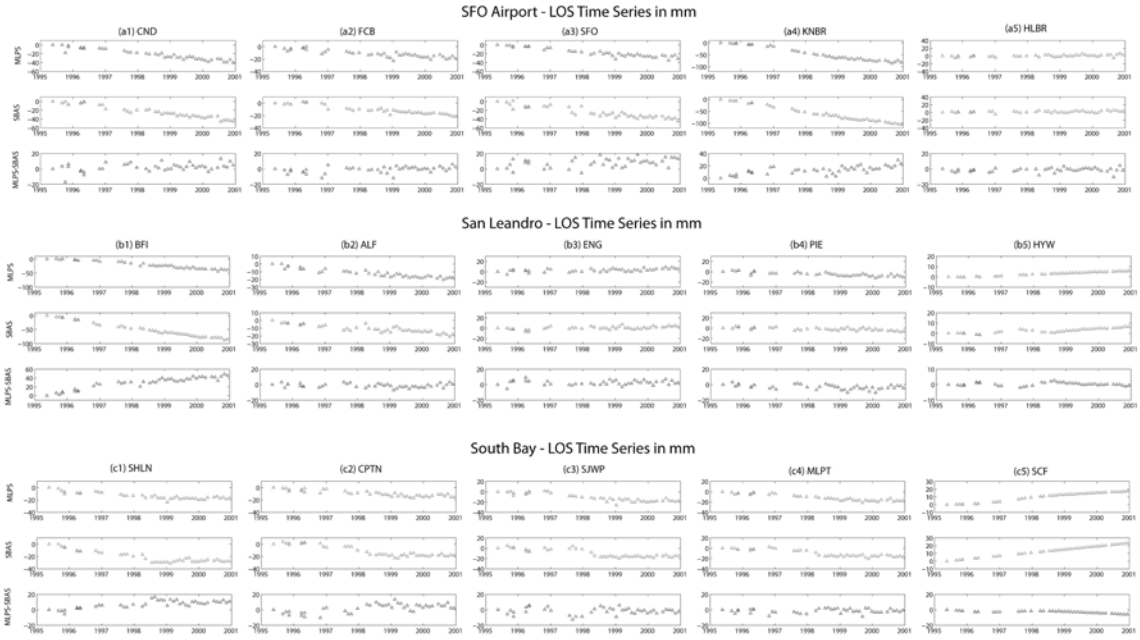

Figure 7.5: Estimated LOS time-series for three different stations for each of the three different regions in the San Francisco Bay Area using the MLPS method and the SBAS method. The difference between the deformation estimates for each of the stations is also shown. b5 and c5 represents the average difference across the Hayward and Silver Creek Faults, respectively, computed in the areas highlighted in Figure 7.4(b3) and Figure 7.4(c3).

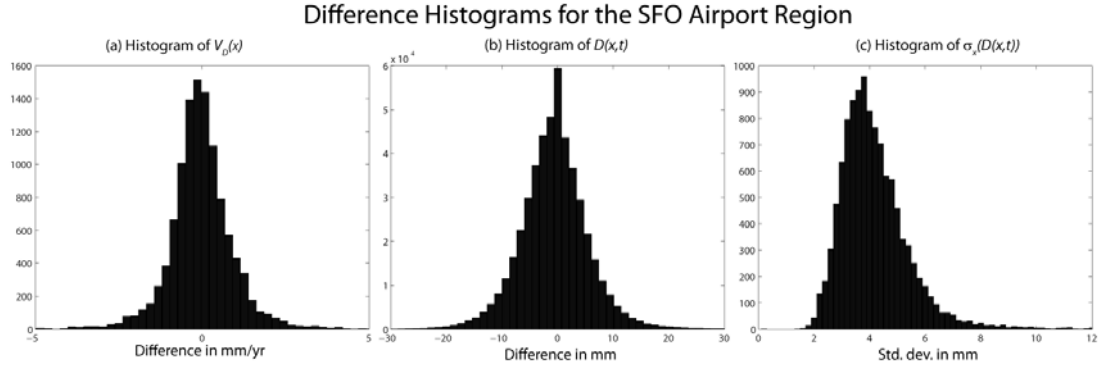

Figure 7.6: (a) Histogram of velocity differences for the SFO airport region. (b) Histogram of the LOS time-series differences for the SFO airport region. (c) Histogram of the pixel-by-pixel std. dev of LOS time-series for the SFO airport region. Note that the first two histograms have a Gaussian structure and the last one, a Rayleigh distribution structure.

Table 7.3: The statistics of the differences between LOS velocities and time-series as estimated using the MLPS and the SBAS techniques for the three sub-regions in the San Francsico Bay Area.

Difference statistic	Formula	SFO Airport	San Leandro	South Bay
Mean bias in velocity difference (mm/yr)	$E\left(V_D\left(x\right)\right)$	0.17	-0.04	-0.23
Std. dev. of velocity difference (mm/yr)	$\sigma\left(V_D\left(x\right)\right)$	1.18	0.76	0.95
Mean bias in time-series difference (mm)	$E\left(D\left(x,t\right)\right)$	-0.50	1.44	-1.06
Std. dev. of time-series difference (mm)	$\sigma\left(D\left(x,t\right)\right)$	6.56	5.39	6.84
Mean of pixel-by-pixel std. dev.	$E\left(\sigma_x\left(D\left(x,t\right)\right)\right)$	4.33	3.61	4.72

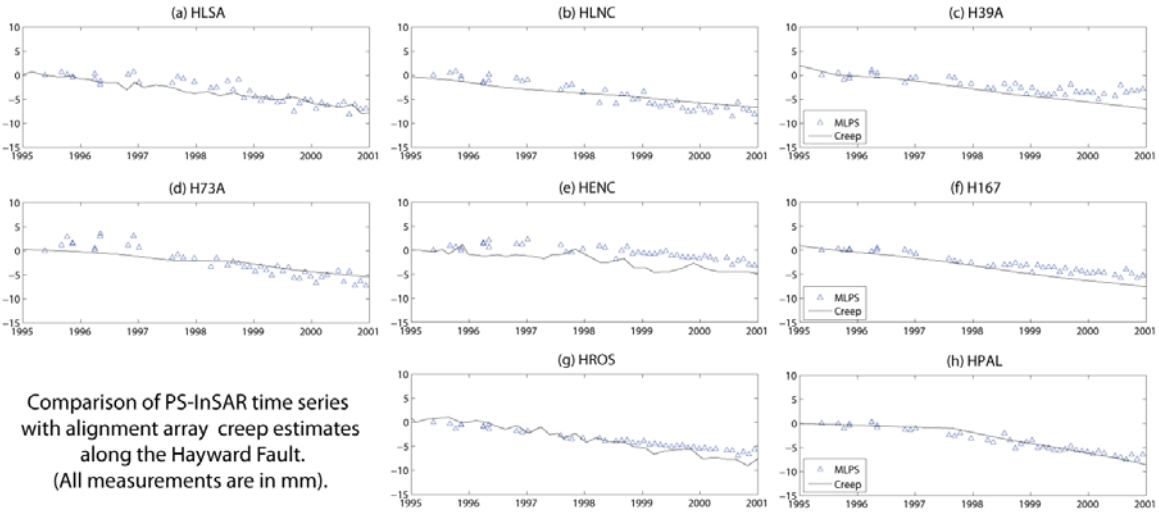

Figure 7.7: PS-InSAR time-series and SFSU-USGS alignment array creep estimates for 8 selected stations along the Hayward Fault.

estimated time-series. PS-InSAR results clearly identify the change in creep rate for station HPAL (Figure 7.7(h)) in mid-1997. Creep meters are insensitive to local vertical deformation where as InSAR is most sensible to vertical deformation by a factor of up to 3. Any local vertical deformation can significantly affect our PS-InSAR

deformation estimates. Table 7.4 shows the difference statistics between the PS-InSAR deformation estimates and the interpolated alignment array measurements for 8 stations along the Hayward Fault. From Table 7.4, we conclude that the discrepancy between the estimated creep from the PS-InSAR time-series and alignment array measurements is 1.5 mm in LOS displacement and 0.5 mm/yr in LOS velocity. These value are similar to those reported by Lanari *et al.* (2007a).

Table 7.4: Mean and standard deviation of the difference between estimated PS-InSAR deformation time-series and observed creep time-series from the SFSU-USGS alignment array for 8 stations.

Station	Mean Bias	Std. dev	Velocity difference
	$E(\Delta(x,t))$	$\sigma(\Delta(x,t))$	$\lvert\Delta_v(x)\rvert$
HLSA	0.53 mm	1.27 mm	0.20 mm/yr
HLNC	-0.07 mm	1.29 mm	0.55 mm/yr
H39A	1.36 mm	1.21 mm	0.54 mm/yr
H73A	0.27 mm	1.60 mm	0.68 mm/yr
HENC	1.78 mm	1.31 mm	0.28 mm/yr
H167	1.25 mm	0.75 mm	0.34 mm/yr
HROS	0.52 mm	1.18 mm	0.63 mm/yr
HPAL	0.08 mm	0.79 mm	0.22 mm/yr

7.4 Conclusions

In this chapter, we have analyzed the noise characteristics of our PS-InSAR technique by focusing on difference between tandem SAR pairs. We have also compared the accuracy of the Stanford University's MLPS selection algorithm in the StaMPS framework against that of the IREA-CNR's SBAS technique, which was one of the original participants of the PSIC-4 study. As major result, we notice that both the PS and SBAS techniques identify the salient deformation features in the Bay Area, with a similar coverage. In addition, the final values obtained for the average difference in estimated LOS velocity and time-series are consistent with those estimated by the ESA PSIC-4 study (Raucoules *et al.*, 2009), for their mining test site in Gardanne,

France and by independent studies (Casu *et al.*, 2006; Lanari *et al.*, 2007a). We also compared our PS-InSAR estimates with observed creep measurements from the SFSU-USGS alignment array and found that our estimates were accurate within 1.5 mm LOS displacement and 0.5 mm/yr LOS velocity, similar to the values reported by Lanari *et al.* (2007a) for SBAS estimates.

Future comparative time-series InSAR studies should also include detailed comparisons of recently developed algorithms, that estimates deformation at the highest possible resolution from short baseline interferograms (Hooper, 2008; Lanari *et al.*, 2004b). Similar comparative studies are needed for data acquired using X-band and L-band sensors to better understand the effects of wavelength, resolution and orbit repeat periods on the ability of time-series InSAR algorithms to study various geophysical phenomena. The ESA supersite initiative will enable us to conduct more inter-comparative studies and validate them against other geodetic measurements and in the process, will enable us better understand the limitations of these time-series techniques.

Chapter 8

Summary

Applicability of conventional interferometric synthetic aperture radar (InSAR) for crustal deformation studies is limited by the fact that almost any interferogram includes large areas where the signals decorrelate and no reliable measurement is possible. Persistent scatterer (PS) InSAR overcomes the decorrelation problem by identifying resolution elements whose echo is dominated by a single scatterer in a series of interferograms. Combining information from multiple interferograms also mitigates the effect of atmospheric distortions in the deformation estimates. Existing PS methods have been very successful in analysis of urban areas, where man-made structures act like strong corner-reflectors. However, man-made structures are absent from most of the Earth's surface. The Stanford method for persistent scatterers (StaMPS) was the first technique designed to extend the applicability of PS-InSAR to natural terrain.

This dissertation has three major aspects to it - i) improving PS selection in natural terrain, ii) developing new phase unwrapping algorithms suitable for multi-dimensional time-series InSAR datasets and iii) describing the noise characteristics of the deformation estimated using PS-InSAR. In Chapter 4 we introduce an information theoretic approach to PS selection that identifies a denser PS network in natural terrain than other published algorithms.

In Chapter 5 we address the phase unwrapping problem and presents two new unwrapping algorithms designed for time-series InSAR applications. The second of

these techniques, the "edgelist" algorithm, relies on a new robust phase unwrapping formulation that is more flexible than the conventional network programming formulations and can incorporate additional geodetic observations as constraints.

In Chapters 6 and 7, we apply our PS-InSAR technique to study rockslides in Lyngen region of Norway and crustal deformation in the San Francisco Bay Area respectively. We also characterize the noise levels in our deformation estimates by comparing our estimates against independent SBAS estimates from research groups in Europe. We observe that our deformation estimates are within 1 mm/yr LOS velocity and 5 mm absolute LOS displacement of the SBAS results. When compared against creep measurements from alignment arrays along the Hayward fault our PS-InSAR time-series matched ground reality to within 1.5 mm LOS displacement and 0.5 mm/yr LOS displacement respectively.

8.1 Future Work and Improvements

PS selection in this work use statistics derived from assumed signal models for the scattering behavior of PS pixels. However, very little work has been done to observe and verify the actual scattering characteristics of PS pixels. Understanding the effect of wavelength, pixel resolution and frequency of SAR acquisitions will help us understand the scattering properties of PS pixels better and will provide insight into the actual scattering mechanisms at work. Such information will be crucial for designing PS selection techniques that will perform better in non-urban terrain. Understanding of these aspects of PS-InSAR is also crucial for design and development of future SAR sensors.

Extracting deformation signatures from the idenfied PS network using phase unwrapping algorithms remains one of the harder aspects of time-series InSAR processing. We have developed the "edgelist" algorithm during the course of this dissertation but all aspects of this formulation have not yet been completely explored. In particular,

1. Fast implementation of this algorithm for large scale time-series InSAR problems with efficient customized linear solvers is yet to be explored.

2. The possibility of using softer inequality constraints as opposed to hard equality constraints using additional geodetic data is yet to be explored.

3. Adjustment of cost functions using *a priori* information regarding the area of study needs to be formalized. We demonstrated in Chapter 5, that adjustment of cost functions is an important issue that needs to be addressed for correctly unwrapping time-series InSAR data across the San Andreas Fault.

Over the last few years, time-series InSAR has taken over from conventional InSAR as the default technique for crustal deformation studies. With the launch of several SAR missions like TerraSAR-X, ALOS PALSAR, COSMO-SkyMed etc, SAR data is being acquired more frequently and in larger volumes than ever before. For maximum utilization of this data resource, automation of time-series InSAR techniques is the need of the hour.

8.2 Conclusions

We have demonstrated the applicability of PS-InSAR techniques in natural terrain in Chapters 4, 5, 6 and 7. We have demonstrated the use of our maximum likelihood PS selection technique and the edgelist unwrapping technique to study time-dependent creep across the Central San Andreas in Chapter 5. We also demonstrate the use of PS-InSAR techniques for studying rockslide activity in Norway in Chapter 6. We have compared our deformation estimates against the SBAS results from research groups in Europe in Chapters 6 and 7, and conclude that our results agree to within 1 mm/yr LOS velocity and 5 mm absolute LOS displacement. Our deformation estimates matched to within 1.5 mm LOS displacment and 0.5 mm/yr LOS velocity when compared against creep measurements from alignment arrays along the Hayward Fault.

References

Abramowitz, M., and Stegun, I. A. 1972. *Handbook of Mathematical Functions with Formulas, Graphs and Mathematical Tables*. Second edn. 180 Varick Street, New York, NY 10014: Dover Publications, Inc.

Adam, N., Kampes, B., Eineder, M., Worawattanamateekul, J., and Kircher, M. 2003. The development of a scientific permanent scatterer system. *In: ISPRS workshop*. Inst. for Photogramm. and Geoinf., Hannover, Germany.

Adam, N., Parizzi, A., Eineder, M., and Crosetto, M. 2009. Practical persistent scatterer processing validation in the course of the Terrafirma project. *Journal of Applied Geophysics*, **69**, 59–65.

Agliardi, F., Crosta, G., and Zanchi, A. 2001. Structural constraints on deep-seated slope deformation kinematics. *Engineering Geology*, **59**, 83–102.

Ahuja, R. K., Hochbaum, D. S., and Orlin, J. B. 1999. *Solving the convex cost integer dual network flow problem*. Integer programming and combinatorial optimization, vol. 1610. Springer Berlin / Heidelberg. Pages 31–44.

Amelung, F., Galloway, D. L., Bell, J. W., Zebker, H. A., and Laczniak, R. J. 1999. Sensing the ups and downs of Las Vegas: InSAR reveals structural control of land subsidence and aquifer system deformation. *Geology*, **27**(6), 483–486.

Amelung, F., Jónsson, S., Zebker, H., and Segall, P. 2000. Widespread uplift and trapdoor faulting on Galapagos volcanoes observed with radar interferometry. *Nature*, **407**(6807), 993–996.

Bamler, R., and Just, D. 1993 (August). Phase statistics and decorrelation in SAR interferograms. *Pages 980–984 of: Proceedings of Geoscience and Remote Sensing Symposium, IGARSS' 93*, vol. 3.

Barber, C., and Huhdanpaa, H. 2009. *QHull*. Retrieved September 01, 2009, from `http://www.qhull.org`.

Berardino, P., Fornaro, G., Lanari, R., and Sansosti, E. 2002. A new algorithm for surface deformation monitoring based on small baseline differential SAR interferograms. *IEEE Trans. on Geosci. Remote Sensing*, **40**(11), 2375–2383.

Berardino, P., Costantini, M., Franceschetti, G., Iodice, A., Pietranera, L., and Rizzo, V. 2003. Use of differential SAR interferometry in monitoring and modelling large slope instability at Maratea (Basilicata, Italy). *Engineering Geology*, **68**, 31–51.

Braathen, A., Blikra, L. H., Berg, S. S., and Karlsen, F. 2004. Rock-slope failures of Norway; type, geometry, deformation mechanisms and stability. *Norwegian Journal of Geology*, **84**, 67–88.

Bürgmann, R., Schmidt, D., Nadaeu, R. M., d'Alessio, M., Fielding, E., Manaker, D., McEvilly, T. V., and Murray, M. H. 2000. Earthquake potential along the northern hayward fault, California. *Science*, **289**(5482), 1178–1182.

Bürgmann, R., Hilley, G., Ferretti, A., and Novali, F. 2006. Resolving vertical tectonics in the San Francisco Bay Area using permanent scatterer InSAR and GPS analysis. *Geology*, **34**(3), 221–224.

Casu, F., Manzo, M., and Lanari, R. 2006. A quantitative assessment of the SBAS algorithm performance for surface deformation retrieval from DInSAR data. *Remote Sens. Environment*, **102**, 195–210.

Chen, C. W., and Zebker, H. A. 2000. Network approaches to two-dimensional phase unwrapping: intractability and two new algorithms. *J. Opt. Soc. Am. A*, **17**(3), 401–414.

Chen, C. W., and Zebker, H. A. 2001. Two-dimensional phase unwrapping with use of statistical models for cost functions in nonlinear optimization. *J. Opt. Soc. Am. A*, **18**(2), 338–351.

Chigira, M. 1992. Long term gravitational deformation of rocks by mass rock creep. *Engineering Geology*, **32**, 157–184.

Ching, N. H., Rosenfeld, D., and Braun, M. 1992. Two-dimensional phase unwrapping using a minimum spanning tree algorithm. *IEEE Trans. Image Proc.*, **1**(3), 355–365.

Colesanti, C., and Wasowski, J. 2006. Investigating landslides with space-borne Synthetic Aperture Radar (SAR) interferometry. *Engineering Geology*, **88**, 173–199.

Colesanti, C., Ferretti, A., Novali, F., Prati, C., and Rocca, F. 2003. SAR monitoring of progressive and seasonal ground deformation using the permanent scatterers technique. *IEEE Trans. on Geosci. Remote Sensing*, **41**(7), 1685–1701.

Costantini, M. 1998. A novel phase unwrapping method based on network programming. *IEEE Trans. on Geosci. Remote Sensing*, **36**(3), 813–821.

Costantini, M., and Rosen, P. A. 1999 (February). A generalized phase unwrapping approach for sparse data. *Pages 267–269 of: Proc. of IEEE Geosci. and Remote Sens. Symposium, IGARSS '99*. IEEE.

Costantini, M., Malvarosa, F., Minati, F., Pietranera, L., Giammarioli, V., and Jahjah, M. 2001 (JULY). A space-time analysis technique for monitoring terrain displacements from SAR differential interferometric measurements. *Pages 2634–2636 of: Proc. IEEE Geosci. and Remote Sens. Symposium, IGARSS '01*, vol. 6. IEEE.

CPLEX. 2006. *Using the CPLEX Callable Library - Version 10.0*. Release by CPLEX optimization Inc., Incline Village, NV.

Crosetto, M., Arnaud, J., Duro, J., Biescas, E., and Agudo, M. 2003. Deformation monitoring using remotely sensed radar interferometric data. *In: Proceedings of* 11^{th} *FIG symposium on deformation measurements, Santorini 03*.

Crosetto, M., Bremmer, C., Hanssen, R., Capes, R., and Marsh, S. 2008. Ground motion monitoring using SAR interferometry: Quality assessment. *European Geologist*, 12–15.

Cumming, I., and Wong, F. 2005. *Digital processing of SAR data*. 685 Canton Street, Norwood, MA 02062: Artech House, Inc.

Cusack, R., and Papadakis, N. 2002. New robust 3D phase unwrapping algorithm: Application to magnetic field mapping and undistorting echo-planar images. *NeuroImage*, **16**, 754–764.

D'aria, D., Ferretti, A., Giudci, D., Guarnieri, A. M., Rizzoli, P., and Rocca, F. 2009. *Method for radiometric calibration of SAR sensors*. PATENT. Application Number: EP2065731, Filing Number:EP20080170042.

Duchossois, G., Kohlhammer, G., and Martin, P. 1996. Completion of the ERS tandem mission. *Earth Observation Quarterly*, **52**, 1–2.

Eiken, T. 2008. *Rapport om Deformasjonsmålingar i Troms 2003–2008*. Tech. rept. University of Oslo. (in Norwegian).

Emardson, T. R., Simons, M., and Webb, F. H. 2003. Neutral atmospheric delay in interferometric synthetic aperture radar applications: Statistical description and mitigation. *J. Geophys. Res.*, **15**(B5), 2231.

Farr, T. G., Rosen, P. A., Caro, E., Crippen, R., Duren, R., Hensley, S., Kobrick, M., Paller, M., Rodriguez, E., Roth, L., Seal, D., Shaffer, S., Shimada, J., Umland, J., Werner, M., Oskin, M., Burbank, D., and Alsdorf, D. 2007. The Shuttle Radar Topography Mission. *Rev. Geophys.*, **45**(RG2004).

Ferretti, A., Prati, C., and Rocca, F. 2000. Nonlinear subsidence rate estimation using permanent scatterers in differential SAR interferometry. *IEEE Trans. on Geosci. Remote Sensing*, **38**(5), 2202–2212.

Ferretti, A., Prati, C., and Rocca, F. 2001. Permanent scatterers in SAR interferometry. *IEEE Trans. on Geosci. Remote Sensing*, **39**(1), 8–20.

Ferretti, A., Savio, G., Barzaghi, R., Musazzi, S., Novali, F., Prati, C., and Rocca, F. 2009. Submillimeter accuracy of InSAR time series: Experimental validation. *IEEE Trans. on Geosci. Remote Sensing*, **45**(5), 1142–1153.

Flynn, T. J. 1997. Two-dimensional phase unwrapping with minimum weighted discontinuity. *J. Opt. Soc. Am. A*, **14**(10), 2692–2701.

Freeman, A. 1992. SAR calibration: an overview. *IEEE Trans. on Geosci. Remote Sensing*, **30**(6), 1107–1121.

Fu, L. L., and Holt, B. 1982. *Seasat view oceans and sea ice with synthetic aperture radar*. Tech. rept. Jet Propulsion Lab.

Funning, G., Parsons, B., Wright, T. J., Jackson, J. A., and Fielding, E. J. 2005. Displacements and source parameters of the 2003 Bam (Iran) earthquake from Envisat advanced synthetic aperture radar imagery. *J. Geophys. Res.*, **110**(B09406).

Gabriel, A. K., Goldstein, R. M., and Zebker, H. A. 1989. Mapping small elevation changes over large areas: Differential radar interferometry. *J. Geophys. Res.*, **94**(B7), 9183–9191.

Ghiglia, D. C., and Pritt, M. D. 1998. *Two-dimensional Phase Unwrapping: Theory, Algorithms, and Software*. New York: Wiley.

Ghiglia, D. C., and Romero, L. A. 1994. Robust two-dimensional weighted and unweighted phase unwrapping that uses fast transforms and iterative methods. *J. Opt. Soc. Am. A*, **11**, 107–117.

Ghiglia, D. C., and Romero, L. A. 1996. Minimum L^p-norm two-dimensional phase unwrapping. *J. Opt. Soc. Am. A*, **13**, 1999–2013.

Goldstein, R. M. 1995. Atmospheric limitations to repeat-track radar interferometry. *Geophys. Res. Lett.*, **22**(18), 2517–2520.

Goldstein, R. M., Zebker, H. A., and Werner, C. L. 1988. Satellite radar interferometry: Two-dimensional phase unwrapping. *Radio Sci.*, **23**, 713–720.

Golub, G. H., and Loan, C. F. Van. 1996. *Matrix Computations*. Third edn. Baltimore: Johns Hopkins University Press.

Hanssen, R. 1998. *Atmospheric Heterogeneties in ERS Tandem SAR Interferometry*. Delft University Press, Delft, The Netherlands.

Hanssen, R. F. 2001. *Radar Interferometry: Data Interpretation and Error Analysis*. First edn. Springer.

Henderson, I. H., Lauknes, T. R., Osmundsen, P. T., Dehls, J., Larsen, Y., and Redfield, T. 2009a. The dynamics of active landslide development and evolution: a combined structural geology, geomorphology and InSAR approach. *Slope Tectonics*. , Geological Society (London) Special Publication (In press).

Henderson, I. H. C., and Saintot, A. 2009. Regional spatial variations in rockslide distribution from structural geology ranking: an example from Storfjorden, western Norway. *Slope Tectonics*. , Geological Society (London) Special Publication (In press).

Henderson, I. H. C., Osmundsen, P. T., and Redfield, T. F. 2009b. *ROS Fjellskred i Troms: Status og planer*. Report 2009.023. Geological Survey of Norway. (in Norwegian).

Hilley, G. E., Bürgmann, R., Ferretti, A., Novali, F., and Rocca, F. 2004. Dynamics of slow moving landslides from permanent scatterer analysis. *Science*, **304**(5679), 1952–1955.

Hoffman, A. J., and Kruskal, J. B. 1965. *Integral boundary points of convex polyhedral*. Linear inequalities and related systems. Princeton University Press, NJ. Pages 223–246.

Hooper, A. 2006 (May). *Persistent scatterer radar interferometry for crustal deformation studies and modeling of volcanic deformation*. Ph.D. thesis, Stanford University.

Hooper, A. 2008. A multi-temporal InSAR method incorporating both persistent scatterer and small baseline approaches. *Geophys. Res. Lett.*, **35**, L16302.

Hooper, A. 2009. *StaMPS*. Retrieved September 01, 2009, from `http://enterprise.lr.tudelft.nl/~ahooper/stamps/`.

Hooper, A., and Zebker, H. 2007. Phase unwrapping three dimensions, with applications to InSAR time series. *J. Opt. Soc. Am. A*, **24**(9), 2737–2747.

Hooper, A., Zebker, H., Segall, P., and Kampes, B. 2004. A new method for measuring deformation on volcanoes and other natural terrains using InSAR persistent scatterers. *Geophys. Res. Lett.*, **31**, L23611.

Hooper, A., Segall, P., and Zebker, H. 2007. Persistent scatterer interferometric synthetic aperture radar for crustal deformation analysis, with application to Volcn Alcedo, Galpagos. *J. Geophys. Res.*, **112**, B07407.

Hungr, O., Evans, S. G., Bovis, M. J., , and Hutchinson, J. N. 2001. A review of the classification of landslides of the flow type. *Environmental and Engineering Geoscience*, **7**(3), 221–228.

Hunt, B. R. 1979. Matrix formulation of the reconstruction of phase values from phase differences. *J. Opt. Soc. Am. A*, **69**(3), 393–399.

Huntley, J. M. 2001. Three-dimensional noise-immune phase unwrapping algorithm. *Applied Optics*, **40**(23), 3901–3908.

Jaboyedoff, M., Ornstein, P., and Rouiller, J. D. 2004. Design of a geodetic database and associated tools for monitoring rock-slope movements: the example of the top of Randa rockfall scar. *Natural Hazards and Earth System Sciences*, **4**, 187–196.

Jacobs, A., Sandwell, D., Fialko, Y., and Sichiox, L. 2002. The 1999 (M_w 7.1) hector mine, california, earthquake: near-field postseismic deformation from ERS interferometry. *Bull. Seism. Soc. Am.*, **92**(4), 1433–1442.

Just, D., and Bamler, R. 1994. Phase statistics of interferograms with applications to synthetic-aperture radar. *Appl. Opt.*, **33**(20), 4361–4368.

Kampes, B. M. 2006. *Radar Interferometry: Persistent Scatterer Technique*. First edn. P. O. Box 17, 3300 AA, Dordrecht, The Netherlands: Springer.

Kampes, B. M., and Adam, N. 2005 (November). STUN algorithm for persistent scatterer interferometry. *In: FRINGE 2005 Workshop*. European Space Agency.

Ketelaar, V. B. H. 2009. *Satellite radar interferometry: Subsidence monitoring techniques*. First edn. P. O. Box 17, 3300 AA, Dordrecht, The Netherlands: Springer.

Knowles, J. D., and Corne, D. W. 2001. A comparison of encodings and algorithms for multiobjective minimum spanning tree problems. *Pages 544–551 of: Proc. of 2001 Conference on Evolutionary Computation, CEC 01*, vol. 1. IEEE.

Kohlhase, A. O., Feigl, K. L., and Massonnet, D. 2003. Applying differential InSAR to orbital dynamics: a new approach for estimating ERS trajectories. *Journal of Geodesy*, **77**(9).

Lanari, R., Zeni, G., Manuta, M., Guarino, S., Berardino, P., and Sansosti, E. 2004a. An integrated SAR/GIS approach for investigating urban deformation phenomena: a case study of the city of Napoli, Italy. *International Journal of Remote Sensing*, **25**(14), 2855–2867.

Lanari, R., Mora, O., Manunta, M., Mallorqui, J. J., Berardino, P., and Sansosti, E. 2004b. A small-baseline approach for investigating deformations on full-resolution differential SAR interferograms. *grs*, **42**(7), 1377–1386.

Lanari, R., Casu, F., Manzo, M., and Lundgren, P. 2007a. Application of SBAS-DInSAR technique to fault creep: A case study of the Hayward Fault, California. *Remote Sensing of Environment*, **109**(1), 20–28.

Lanari, R., Casu, F., Manzo, M., Zeni, G., Berardino, P., Manunta, M., and Pepe, A. 2007b. An overview of Small Baseline Subset Algorithm: A DInSAR technique for surface deformation analysis. *Pure and Applied Physics*, **164**(4), 637–661.

Larsen, Y., Engen, G., Lauknes, T. R., Malnes, E., and Høgda, K. A. 2005. A generic differential interferometric SAR processing system, with applications to land subsidence and snow-water equivalent retrieval. *In: Proc. Fringe 2005 Workshop, ESA ESRIN, Frascati, Rome, November 28–December 2 (ESA SP-610).*

Lauknes, T. R., Dehls, J., Larsen, Y., Høgda, K. A., and Weydahl, D. J. 2005. A comparison of SBAS and PS ERS InSAR for subsidence monitoring in Oslo, Norway. *In: Proc. Fringe 2005 Workshop, ESA ESRIN, Frascati, Rome, November 28–December 2.*

Lauknes, T. R., Zebker, H., and Larsen, Y. 2009. InSAR Deformation Time Series Using an L_1-norm Small-Baseline Approach. *IEEE Trans. on Geosci. Remote Sensing.* , submitted for publication.

Lauknes, T. R., Shanker, A. P., Dehls, J. F., Zebker, H. A., Henderson, I. H. C., and Larsen, Y. 2010. Detailed landslide mapping in northern Norway with small-baseline and persistent scatterer interferometric SAR time series methods. *Remote Sensing of Environment.*

Lee, J. S., Hoppel, K. W., Mango, S. A., and Miller, A. R. 1994. Intensity and Phase statistics of Multilook Polarimetric and Interferometric SAR Imagery. *IEEE Trans. on Geosci. Remote Sensing*, **32**(5), 1017–1028.

Lyons, S., and Sandwell, D. 2003. Fault creep along the southern San Andreas from interferometric synthetic aperture radar, permanent scatterers, and stacking. *J. Geophys. Res.*, **108**(B1), 2047.

Marlow, M. S., Jachens, R. C., Hart, P. E., Carlson, P. R., Anima, R. J., and Childs, J. R. 1999. Development of the San Leandro synform and neotectonics of the San Francisco Bay block, California. *Marine and Petroleum Geology*, **16**(5), 431–442.

Massonnet, D., Rossi, M., Carmona, C., Adragna, F., Peltzer, G., Feigl, K., and Rabaute, T. 1993. The displacement field of the Landers earthquake mapped by radar interferometry. *Nature*, **364**, 138–142.

McFarland, F. S., Lienkaemper, J. J., and Caskey, S. J. 2009. *Data from theodolite measurements of creep rates on San Francisco Bay Region faults, California, 1979-2009.* U.S. Geological Survey Open- File Report 2009-1119. U.S Geological Survey. Available at `http://pubs.usgs.gov/of/2009/1119/`.

Mount, D. M., and Arya, S. 2010. *ANN: A Library for Approximate Nearest Neighbor Searching.* Version 1.1.2 Released on Jan 27, 2010 from `http://www.cs.umd.edu/~mount/ANN/`.

Nadeau, R. M., and McEvilly, T. V. 2004. Periodic pulsing of characteristic micro earthquakes on San Andreas Fault. *Science*, **303**(5655), 220–222.

Nutricato, R., Bovenga, F., and Refice, A. 2002 (June). Optimum interpolation and resampling for PSC identification. *Pages 3626–3628 of: Proceedings of Geoscience and Remote Sensing Symposium, IGARSS '02*, vol. 6.

Okada, Y. 1985. Surface deformation due to shear and tensile faults in a half space. *Bull. Seism. Soc. Am.*, **75**(4), 1135–1154.

Onn, F., and Zebker, H. A. 2006. Correction for interferometric synthetic aperture radar atmospheric phase artifacts using time series of zenith wet delay observations from a gps network. *J. Geophys. Res.*, **111**(B09102).

Osmundsen, P. T., Henderson, I., Lauknes, T. R., Larsen, Y., Redfield, T. F., and Dehls, J. 2009. Active normal fault control on landscape and rock-slope failure in northern Norway. *Geology*, **37**(2), 135–138.

Papoulis, A. 1991. *Probability, Random Variables and Stochastic Processes*. 3rd edn. 1221 Avenue of the Americas, New York, NY 10020: McGraw-Hill.

Pepe, A., and Lanari, R. 2006. On the extension of minimum cost flow algorithm for phase unwrapping of multitemporal differential SAR interferograms. *IEEE Trans. on Geosci. Remote Sensing*, **44**(9), 2374–2383.

Pollitz, F. F., Wicks, C., and Thatcher, W. 2001. Mantle flow beneath a continental strike-slip fault: postseismic deformation after the 1999 hector mine earthquake. *Science*, **293**(5536), 1814–1818.

Pritchard, M. E., and Simons, M. 2002. A satellite geodetic survey of large scale deformation of volcanic centers in the central andes. *Nature*, **418**(6894), 167–171.

Pritt, M. D. 1996. Phase unwrapping by means of multigrid techniques for interferometric SAR. *IEEE Trans. on Geosci. Remote Sensing*, **34**(3), 728–738.

Raucoules, D., Bourgine, B., deMichele, M., Cozannet, G. Le, Bremmer, C., Veldkamp, J. G., Tragheim, D., Bateson, L., Crosetto, M., Agudo, M., and Engdahl, M. 2009. Validation and intercomparison of Persistent Scatterers Interferometry: PSIC4 project results. *Journal of Applied Geophysics*, **68**(3), 335–347.

Rolandone, F., Bürgmann, R., Agnew, D. C., Johnson, I. A., Templeton, D. C., d'Alessio, M. A., Titus, S. J., DeMets, C., and Tikoff, B. 2007. Aseismic slip and fault-normal strain along the creeping segment of the San Andreas fault. *Geophys. Res. Lett.*, **35**(L14305).

Rosen, P. A., Hensley, S., Joughin, I. R., Li, F. K., Madsen, S. N., Rodriguez, E., and Goldstein, R. M. 2000. Synthetic aperture radar interferometry. *Proc. IEEE*, **88**(3), 333–382.

Rott, H., and Nagler, T. 2006. The contribution of radar interferometry to the assessment of landslide hazards. *Advances in Space Research*, **37**, 710–719.

Ryder, I., and Bürgmann, R. 2008. Spatial variations in slip deficit on the central San Andreas fault from InSAR. *Geophysical Journal Intl.*, **175**(3), 837–852.

Sandwell, D. T., and Price, E. J. 1998. Phase gradient approach to stacking interferograms. *J. Geophys. Res.*, **103**(B12), 30183–30204.

Sansosti, E., Berardino, P., Manunta, M., Serafino, F., and Fornaro, G. 2006. Geometrical SAR image registration. *IEEE Trans. on Geosci. Remote Sensing*, **44**(10), 2861–2870.

Saribandi, K. 1992. Derivation of phase statistics from Mueller matrix. *Radio Sci.*, **27**(5), 553–560.

Scharroo, R., and Visser, P. 1998. Precise orbit determination and gravity field improvement for the ERS satellites. *J. Geophys. Res.*, **103**(B4), 8113–8127.

Schmidt, D. A., R.Bürgmann, Nadeau, R. M., and d'Alessio, M. 2005. Distribution of aseismic slip rate on the Hayward fault inferred from seismic and geodetic data. *J. Geophys. Res.*, **110**(B08406).

Shanker, A. P., and Zebker, H. 2007. Persistent scatterer selection using maximum likelihood estimation. *Geophys. Res. Lett.*, **34**, L22301.

Shanker, A. P., and Zebker, H. 2010. Edgelist phase unwrapping algorithm for time-series InSAR. *J. Opt. Soc. Am. A*, **37**(4).

Shanker, A. P., and Zebker, H. A. 2008. Sparse two-dimensional phase unwrapping using regular grid methods. *IEEE Geosci.Remote Sensing Lett.*, **6**(2), 327–331.

Simons, M., Fialko, Y., and Rivera, L. 2002. Coseismic deformation from the 1999 msubw 7.1 hector mine, california, earthquake as inferred from insar and gps observations. *Bull. Seism. Soc. Am.*, **92**(4), 1390–1402.

Skolnik, M. L. 2001. *Introduction to RADAR systems*. 3 edn. 1221 Avenue of the Americas, New York, NY 10020: Tata McGraw-Hill.

Solheim, A., Bhasin, R., DeBlasio, F. V., Blikra, L. H., Boyle, S., Braathen, A., Dehls, J., Elverhøy, A., Etzelmüller, B., Glimsdal, S., Harbitz, C. B., Heyerdal, H., Høydal, Ø. A., Iwe, H., Karlsrud, K., Lacasse, S., Lecomte, I., Lindholm, C., Longva, O., Løvholt, F., Nadim, F., Nordal, S., Romstad, B., Rød, J. K., and Strout, J. M. 2005. International Centre for Geohazards (ICG): Assessment, prevention and mitigation of geohazards. *Norwegian Journal of Geology*, **85**, 45–62.

Soumekh, M. 1999. *Synthetic Aperture Radar Signal Processing*. First edn. New York: John Wiley & Sons, Inc.

Strozzi, T., Farina, P., Corsini, A., Ambrosi, C., Thüring, M., Zilger, J., Wiesmann, A., Wegmüller, U., and Werner, C. 2005. Survey and monitoring of landslide displacements by means of L-band satellite SAR interferometry. *Landslides*, **2**(3), 193–201.

Touzi, R., Lopes, A., Bruniquel, J., and Vachon, P. W. 1990. Coherence estimation for SAR imagery. *IEEE Trans. on Geosci. Remote Sensing*, **28**(1), 88–97.

Ulander, L. M. H. 1991. Accuracy of using point targets for SAR calibration. *IEEE Trans. on Aero. and Elec. Sys.*, **27**(1), 139–148.

Werner, C., Wegmuller, U., Strozzi, T., and Wiesmann, A. 2003 (July). Interferometric point target analysis for deformation mapping. *Pages 4362–4364 of: Proceedings of Geoscience and Remote Sensing Symposium, IGARSS '03*, vol. 7.

Zebker, H. A., and Goldstein, R. M. 1986. Topographic mapping from interferometric synthetic aperture radar observations. *J. Geophys. Res.*, **91**(B5), 4993–5000.

Zebker, H. A., and Lu, Y. 1998. Phase unwrapping algorithms for radar interferometry: residue-cut, least squares and synthesis algorithms. *J. Opt. Soc. Am. A*, **15**(3), 586–598.

Zebker, H. A., and Villasenor, J. 1992. Decorrelation in interferometric radar echoes. *IEEE Trans. on Geosci. Remote Sensing*, **30**(5), 950–959.

Zebker, H. A., Rosen, P. A., Goldstein, R. M., Gabriel, A., and Werner, C. 1994. On the derivation of coseismic displacement field using differential radar interferometry : The Landers earthquake. *J. Geophys. Res.*, **99**, 19618–19634.

Zebker, H. A., Rosen, P. A., and Hensley, S. 1997. Atmospheric artifacts in interferometric synthetic aperture radar surface deformation and topographic maps. *J. Geophys. Res.*, **102**, 7547–7563.

Zhou, G., and Gen, M. 1997. Genetic programming approach on multi-criteria minimum spanning tree problem. *European Journal of Operations Research*, **114**(1), 141–152.